Homogenisation of Slender Periodic Composite Structures

Julián Dizy Suárez

Imperial College London
Department of Aeronautics

This thesis is submitted for the degree of Doctor of Philosophy and the Diploma of Imperial College London.

October 2013

Declaration

I hereby declare that this thesis, and the research to which it refers, are the product of my own work, and has not been submitted for any other reward. Ideas and quotations from the work of other people, published or otherwise, are fully acknowledged. The copyright of this thesis rests with the author and is made available under a Creative Commons Attribution Non-Commercial No Derivatives license. Researchers are free to copy, distribute or transmit the thesis on the condition that they attribute it, that they do not use it for commercial purposes and that they do not alter, transform or build upon it. For any reuse or redistribution, researchers must make clear to others the license terms of this work.

Julián Dizy Suárez

Strength does not come from winning. Your struggles develop your strengths. When you go through hardships and decide not to surrender, that is strength.

A. Schwarzenegger

To my parents

Acknowledgments

I would like to express my deepest gratitude to my exceptionally knowledgeable, patient and inspirational academic supervisors: Dr. Rafael Palacios and Dr. Silvestre Pinho. Muchas gracias y muito obrigado to both for your advice and guidance throughout the project.

I am very grateful to Dr. Henrik Hesse and Mr. Robert Simpson for developing *SHARP.beams*, the geometrically nonlinear beam solver which I have used in this work to couple my homogenisation tool with. I would also like to thank Dr. Nelson Vieira De Carvalho (currently at NASA Langley) and Dr. Matthew Laffan for their involvement and participation. Furthermore, my gratitude goes to all the members of the Composites and Aeroelastics groups for their encouragement and interesting discussions.

Financial support for part of my graduate and post-graduate studies came from the Spanish *Fundación para el desarrollo de la formación en las zonas mineras del carbón* and it is gratefully acknowledged. Travel grants from the Royal Aeronautical Society, Imperial College Trust and Old Centralians' Trust are also greatly appreciated.

Finally, I would like to thank my parents Julián and Josefina, my brother Eduardo and my grandparents for their support. Also, thank you Mira and Leonardo for humouring me and making the British winter (or summer) bearable throughout the duration of this work.

Abstract

The increasing efficiency and performance requirements on current aircraft requires the use of novel configurations and analysis methodologies which capture their behaviour both accurately and efficiently. In spite of the great improvements in computational power, simulating the full 3D structure is too costly and unviable for conceptual design stages. Hence, reduced order models that accurately describe the behaviour of these engineering structures are demanded. This work focuses on those that have a dominant dimension and, because the characteristic length of the sought response so allows it, can be assimilated into a 1-D beam model. A homogenisation technique is introduced to obtain the full 6×6, i.e. including transverse shear effects, equivalent 1-D stiffness properties of complex slender composite structures. The classical 4×4 stiffness matrix is obtained for periodic structures, that is, without the usual assumption of constant cross sections. The problem is posed on a unit cell with periodic boundary conditions such that the small-scale strain state averages to the large-scale one and the deformation energy is conserved between scales. The method is devised such that its implementation can be carried out using a standard finite-element package whose advantages can be exploited. This technique is readily applicable to engineering models. It provides a new level of modelling flexibility by employing tie constraints between different parts so that parametric analyses or optimisation can be performed without re-meshing. The proposed methodology allows local stress recovery and local (periodic) buckling strength predictions; nonlinear effects such as skin wrinkling can therefore be propagated to the large scale. Numerical examples are used to obtain the homogenised properties for several isotropic and composite beams, with and without transverse reinforcements, taper or thickness variation, and for both linear and geometrically-nonlinear deformations. The periodicity in the local post-buckling response disappears in the presence of localisation in the solution and this is also illustrated by a numerical example. Finally, the code originated from this work, SHARP.cells, is coupled with a nonlinear beam solver.

Contents

List of Figures

List of Tables

Nomenclature

The main symbols used in this dissertation are listed below:

Symbols

AR	aspect ratio
a	body-fixed frame of reference
B	deformed (material) frame of reference of each cross section
b	unit cell depth, m
C^{Ba}	coordinate transformation matrix, from a to B
$\mathcal{C}_{ijkl}$	material elasticity tensor
D	full vector of degrees of freedom
E	Young's modulus
$e_{\alpha\beta}$	Levi-Civita permutation symbol
F	nodal external forces
$\mathbb{F}$	cross-sectional internal forces
G	shear modulus
H	cross-sectional angular momenta
h	transverse dimension of the beam
$\mathbb{I}$	identity matrix
J_{ij}	cross-sectional moment of inertia
$\mathcal{K}$	global stiffness matrix
K_B	local curvature
L	length of the beam (or total length of all beams)
$\mathcal{M}$	global mass matrix
M	cross-sectional mass matrix or nodal external moments
$\mathbb{M}$	cross-sectional internalm moments
m	mass per unit length
N	matrix of shape functions
N_e	number of nodes
n	unit vector
P	cross-sectional translational momenta
Q	generalised forces
R	full vector of forces
S	cross-sectional stiffness matrix
s	semi-width

Symbols (contd.)

$\mathcal{T}$	kinetic energy
T	tangential rotation operator
t	physical time or thickness
$\mathcal{U}$	internal (strain) energy
u_i	large scale (beam) displacements
V_b	local translational velocity
v_a	rigid-body translational velocity
v_i	small scale (unit cell) displacements
$\vec{v}$	inertial translational velocity of the body-fixed frame, a
$\mathcal{W}$	virtual work
w_i	warping field
x_i	small scale (unit cell) coordinates
x_{cg}	location of the centre of gravity
y	large scale (beam) reference coordinate

Greek

β	variable containing nodal displacements and velocities
γ_i	beam strains
Δ	increment
η	variable containing nodal displacements and rotations
ϵ	vector of beam strains
ε_{ij}	small scale strain tensor
ζ	orientation of the A-frame
η	nodal displacements and rotations
θ_i	local beam rotations
κ_i	beam curvatures
ν	Poisson's ratio
ρ	density
σ_{ij}	small scale stress tensor
ξ	in-plane coordinates
ϕ	single rotation about a unit vector
$\delta\Phi$	local virtual rotations
Ψ	Cartesian rotation vector
Ω	unit cell volume
ω_a	rigid-body rotational velocity
Ω_b	local rotational velocity

Operators, subscripts, superscripts and others

$\dot{\bullet}$	time derivatives, $\frac{d}{dt}$
$\bullet'$	spatial derivatives along arc length, $\frac{d}{dy}$
$\langle\bullet\rangle$	average integral over the volume of a unit cell
$\tilde{\bullet}$	cross-product or skew-symmetric operator
$\bullet_{,j}$	partial derivatives, $= \frac{\partial \bullet}{\partial x_j}$
$[\bullet]$	matrix
$\{\bullet\}$	column vector
`*.py`	Python file
$\bullet_c$	condensed degrees of freedom
$\bullet_r$	retained degrees of freedom
$\bullet_a$	body-fixed, main frame of reference
$\bullet_B$	local, deformed frame of reference
#	number of

Abbreviations

AIAA	American Institute of Aeronautics and Astronautics
ATR	Active Twist Rotor (blade)
BEM	Boundary Element Method
CPU	Central Processing Unit
CRV	Cartesian Rotation Vector
d.o.f.	degree(s) of freedom
EoM	Equations of Motion
EUCASS	European Conference for Aeronautics and Space Sciences
FEM	Finite Element Method
GECB	Geometrically-Exact Composite Beam
HALE	High-Altitude Long-Endurance
HDD	Hard Disk Drive
MIT	Massachusetts Institute of Technology
NACA	National Advisory Committee for Aeronautics (now NASA)
NASA	National Aeronautics and Space Administration (formerly NACA)
OS	Operating System
PBCs	Periodic Boundary Conditions
RAM	Random Access Memory
RPM	Revolutions Per Minute
SHARP	Simulation of High-Aspect-Ratio Planes
SSD	Solid State Drive
UAV	Unmanned Aerial Vehicle
UM/VABS	University of Michigan Variational Asymptotic Beam Section (code)
w.r.t.	with respect to

Chapter 1

Introduction

Despite significant advances in computational power in the last decade, which allow direct solid modelling of most engineering structures, there is still a practical interest in dimensionally-reduced structural models. Beam models, in particular, provide excellent approximations of the primary structures for low-frequency aeroelastic analysis of high-aspect-ratio wings, helicopter rotor blades or wind turbines. Slenderness, defined by the existence of a predominant dimension much larger than the other two, is a property that is common to all these structures. High altitude long endurance (HALE) unmanned aerial vehicles (UAV) (like those from Figure 1.2) are an aircraft example that employs slender wings. They are designed to fly during extended periods of time, sometimes weeks, performing missions such as cartography, weather sensing or telecommunication relay (replacing satellites for a fraction of the price). This means heavy payloads (relative to their weight) which require high aerodynamic and structural efficiency. Hence, high-aspect-ratio wings made out of composite materials, which have very good stiffness-to-weight ratios, are used. As a result, the efficient and accurate modelling of these lightweight structures represents a significant engineering challenge [72].

The suitability of idealising slender structures as beams lies not only on the topology of the structure but also on the desired aim of the analysis. For instance,

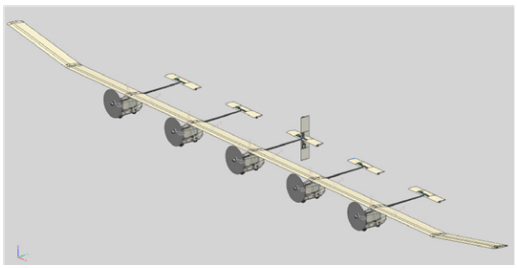

(a) X-Hale from the University of Michigan [21]

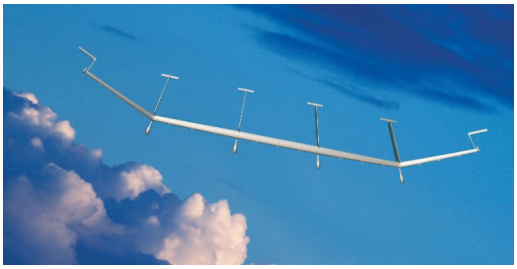

(b) Solar Eagle from Boeing

Figure 1.1.: Two concepts of HALE UAVs with very high AR wings

if one seeks to predict the flight dynamics behaviour of one of these aircraft when flying through a gust, then a geometrically nonlinear beam model, populated with the right elastic and inertial properties, and tightly coupled with an adequate aerodynamic model will most likely be appropriate. However, if the root assembly of the aforementioned aircraft wing with the fuselage is to be sized under static loads then a more detailed representation is required; full 3D finite element analysis is then unavoidable. Most of the time, when dealing with slender structures for said applications, a considerable amount of time is spent in the conceptual design stage using beam models that enable engineers to assess the relative performance of multiple configurations: different materials, layups, geometries, etc. There exists a vast range of options for the way that these models are constructed. It is paramount that the chosen option is as accurate as possible while being computationally efficient, flexible in its implementation and versatile in its applicability. This way, the best possible solutions for the engineering problems at hand will be determined early in the design stage and avoid unnecessary development expenses for inadequate ones during the detail design.

This research addresses the need for an efficient homogenisation technique to create a beam model that can be used with complex cross sections, that is able to account for the effects of transverse shear for composite structures and that allows variations of the cross section along the main dimension of the beam. Transverse reinforcements like ribs carry the loads from the control surfaces, store stations and landing gear to the spars and skins [90]. This type of reinforcement and spanwise

thickness variations are frequently encountered in such applications to strengthen the otherwise too flexible structure and/or to divide different compartments within. We aim to include such variations in a novel unit cell approach that will be implemented using an unmodified, off-the-shelf finite element solver and that therefore takes advantage of the capabilities that standard finite element packages have in the present time.

1.1. Previous Work

As noted above, there are many available analysis methods for the study of composite slender structures. This section provides an overview of the most relevant ones and the state-of-the-art alternatives to the work presented in this thesis. The first subsection covers some of the most common areas of application for beam models. In general, the modelling process can be split into two different stages: Firstly, there is a *homogenisation step*, which determines the constitutive relations of the reduced model (i.e. beam sectional properties); secondly, there is a *solution step*, in which one evaluates the response of the dimensionally-reduced model to the set of applied loads. Both stages are interrelated as assumptions on one affect the other. Subsection 1.1.1 covers the former step and it explains the different options available to obtain the properties of the reduced order models and Subsection 1.1.2 treats the latter. The amount of literature dedicated to beam theories is so large that a comprehensive revision of all the contributions is impractical and only the most important ones will be detailed here.

Applications of Beam Models

Beam models have proven to be very useful in a wide range of applications where the structure under investigation presents a morphology and a typical response conforming with the conditions introduced above. As an example, we have introduced HALE UAVs, where nonlinear beam models are used due to the presence of large deformations of the lifting surfaces which can change the natural frequencies

of the wings [84]. A review of the available analysis methods for these aircraft was presented by Palacios et al. [83] where the three main types of structural models were compared: displacement-based, strain-based and intrinsic formulations. The first option is the most commonly found in literature but it is not very computationally efficient. It also proses the problem of how the parameterisation of finite rotations is handled. The strain-based formulation offers an efficient alternative to remedy this. The third and most efficient formulation is the intrinsic model, also known as hybrid or mixed formulation, which can greatly reduce the computational cost of the conventional, displacement-based method by combining velocities and internal forces to define the independent structural states of the aircraft. Very recently, Palacios presented a further possibility based on the nonlinear normal modes of the structure expressed in terms of nodal strains and velocities alone [81]. Additionally, considerable work has been done in the area of helicopter rotor blades where the abundance of proposed methodologies and the lack of public access to experimental results and benchmark problems have made it difficult to know which theories work best in which cases. A good review of these theories and their relative performance was presented almost simultaneously by Jung et al [59] and Volovoi et al [109]. They concluded that, in the context of helicopter rotor blades, the addition of refined, higher-order theories (with more degrees of freedom and larger cross-sectional stiffness matrices) was unjustified and unnecessary and claims of increased accuracy were based on miscalculated classical stiffness terms. They also mistrust the influence of transverse shear and Vlasov's warping on sufficiently long box beams. Of course, they acknowledge the importance of these in shorter or open-section beams. The application of beam models to rotating blades was naturally extended to wind turbines [23]. In this case, beam models are not limited to the calculation of effective cross sectional properties [57] used in a static analysis. Instead, they are also used to model wind turbine vibration modes [61] or assess their fatigue resistance, as it was proven by Mandell et al [73]. They manufactured and tested an extensive set of I-beams to represent the wind turbine blade spar. Carbon nanotubes are another relevant application for beam models particularly

since the rise in computational power at the beginning of this century that allowed large enough simulations to characterise the properties of this helical nanostructures [70]. Messager and Cartraud adapted their work on wire springs and stranded ropes [17] to calculate the axial stiffness of single-walled nanotubes [75]. Response of materials at the nanoscale is different from those in their bulk counterparts, hence nonlocal elasticity assumes that stress at a reference point is a functional of the strain field at every point of the continuum [36]. Therefore, nonlocal beam models employed in the analysis of double-walled carbon nanotubes [2] must use material constitutive relations based on nonlocal parameters [35]. Furthermore, marine riser pipes [62] protein chains [62] and even long bones [8] have also been modelled using beams. The simplicity of construction of the models also makes them essential tools in many other applications for conceptual studies.

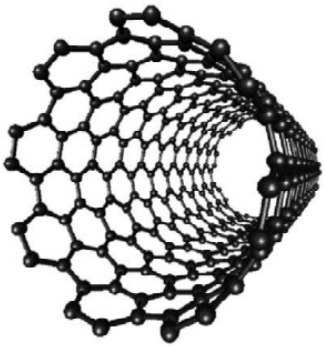

(a) Single-walled carbon nanotube [67]

(b) Offshore wind turbines in Denmark[13]

Figure 1.2.: Example of slender structures which can be idealised with a beam model

1.1.1. Homogenisation Stage

All the previous models and applications require an estimate of the cross-sectional properties; the available procedures to obtain these properties used in the dimensionally reduced models are detailed next. This step is the main focus of this work. Solution methods to the 1D problem are treated in Subsection 1.1.2.

Classical Models and Transverse Shear

The study of slender structures begins with the classical assumptions that solid homogeneous isotropic structures, under small deformations follow a specific set of kinematic relations for the displacement field. If the cross-sectional plane remains perpendicular to the beam reference axis we have the Euler-Bernoulli beam. If it does not, we have the Timoshenko beam [107]. Depending on the shape of the cross section, Timoshenko introduced a *shear correction factor* that calibrates the assumption of constant shear strain over the cross section. This shear coefficient approximates the correct integrated value of strain energy due to shear to a constant average at the reference line [1]. Over the years, much discussion has been generated around the correctness or even existence of such correction factors [32, 44]. Shear correction factors are closely linked to kinematic assumptions on sectional warping. Warping aims to capture the difference between the real behaviour of the actual cross section –when subject to certain loadings– and the assumed, larger scale one. It was first introduced in Saint-Venant's theory of torsion in 1856 [31]. Over a century and a half later, the application of warping has been extended to all six classical degrees of freedom and to solid, as well as thin, cross sections made of anisotropic materials too [89]. There are two main strategies that can be used to obtain the 1-D properties of heterogeneous anisotropic beams: one can solve the 3-D equations of elasticity asymptotically or introduce an assumption on the warping field that calibrates the displacement field. The main contributions for each group of theories are described next. In the second group we include not only those theories that pose assumptions on the warping field but also those that solve it exactly by discretising the domain.

Asymptotic Solutions

For composite beams, one of the most successful approaches in dealing with arbitrary sectional properties is the Variational Asymptotic Method (VAM) [19] based on the variational framework developed by Berdichevsky [6, 7]. The analysis asymptotically approximates the 3D warping of the displacement field

that minimises the cross-sectional deformation energy for each beam strain state and thus finds the constitutive relations for the 1D beam analysis. After the global deformation from the 1D (possibly nonlinear) beam analysis is obtained, the original 3D displacements, stresses and strains can also be recovered using those 3D warping influence coefficients. It is worth noting that solutions based on VAM only apply to the interior solutions in constant-section beams. Recently, Lee and Yu [68] have proposed, as a partial remedy to that shortcoming, to use the smallness of the heterogeneity and incorporate a spanwise dimensional reduction, in the homogenisation step of the variational asymptotic method. The resulting formulation is then similar to that obtained by the Formal Asymptotic Method [9, 10, 65], which exploits the existence of two scales in the original dynamic 3D equations governing the elastic response of the beam structure to perform an asymptotic homogenisation. However, it is not always apparent in the original formulation how to define an adequate set of boundary conditions, implementing it numerically or adapting it to conventional engineering models. This was later remedied by Cartraud and Messager [17], who restricted the solution to the four "classical" beam elastic states (axial, torsion and bending in two directions). The resulting problem was then implemented in a commercial finite-element packages (Samcef). This work resulted in an approach similar to that of Ghiringhelli and Mantegazza [41] who modified a finite element software's matrix solution procedure to apply the theory developed by Giavotto et al. [42], based on an eigenvalue problem for the basic beam motions, to obtain stiffness and stresses of a beam section made of anisotropic materials.

Non-asymptotic Methods

As an extension to the classical beam theories, one can refine the through-the-thickness representation based on assumptions made in the out of plane warping. Rand [89] did this for composite beams as Reddy had done much earlier

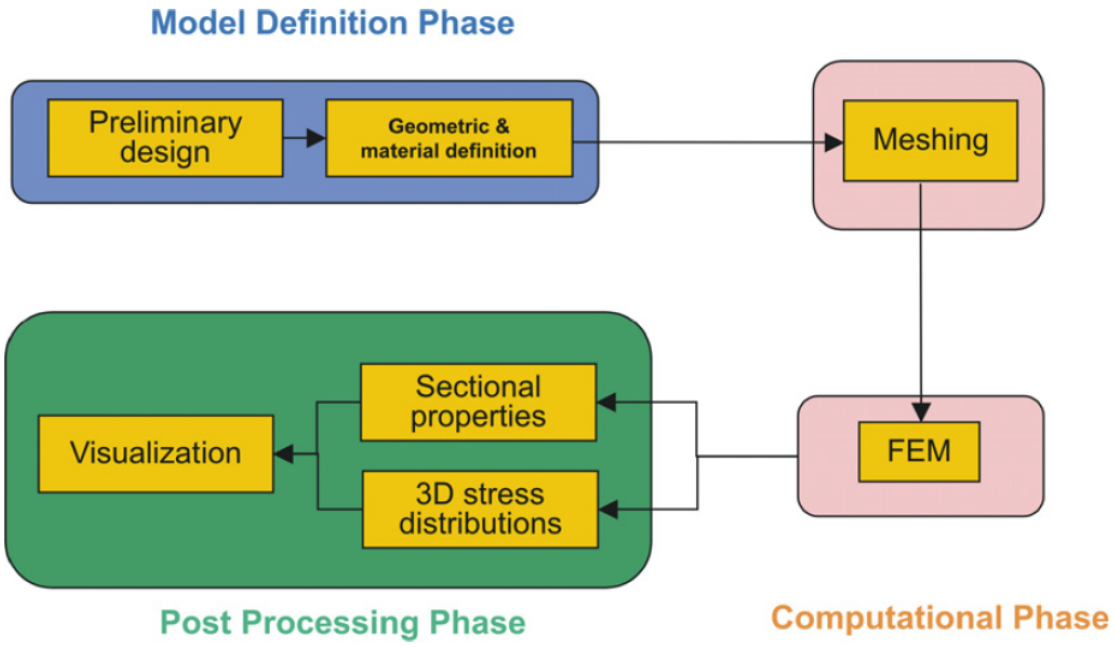

Figure 1.3.: Phases present in a typical FEM cross-sectional analysis of composite beams [22].

for laminated composite plates [91]. Thin- and thick-walled rotor blades were also given this upgrade by Jung et al. [60].

Finite element analysis has been widely used in the calculation of the effective beam sectional properties. It is not uncommon to wrap the homogenisation process around a finite element solver roughly following the stages shown in Figure 1.3. Hill and Weaver [48] used Nastran to extrude a 2D section of an anisotropic beam and retrieve the full 6×6 stiffness matrix via a 2-stage analysis: Firstly a set of unit loads is applied to the classical degrees of freedom and finally, using the reaction forces due to bending a second analysis can be run which computes the shear components by eliminating the bending moment and all remaining coupling terms. In essence, this is very similar, albeit superior due to the applicability to anisotropic materials, to the work by Jonnalagadda and Whitcomb [57] to calculate the transverse shear components of the stiffness matrix. Their approach is also based on applying to the section a bending moment equal in magnitude, but with opposite sign, than that created by the shear force, however this is only presented for isotropic structures of

constant cross sections. Carrera et al employed a finite element formulation for static [15] and vibration [16] analyses overcoming the limitations that their closed-form hierarchical solution [14] faces when dealing with arbitrary cross sections.

The boundary element method (BEM) is also used to analyse the behaviour of composite beams as an alternative to the finite element method. Instead of discretising the whole cross section into area (triangular or quadrilateral) elements limited to certain shape and distortion, only the boundary is discretised, resulting in line or parabolic elements with a comparatively small number required to achieve good accuracy. Sapountzakis and Tsiatas [94] have studied the effects of transverse shear in a nonlinear analysis of a Timoshenko beam with arbitrary variable cross sections. The same group of researchers have used this approach to model flexural-torsional linear buckling [93], post-buckling behaviour [33] and transverse shear loading [76]. Chakravarty [22] has reviewed the most relevant contributions using BEM and summarised its advantages and disadvantages over a FEM approach. The BEM only requires a mesh on the boundary and it only approximates the boundary conditions, not the differential equations. However, the solution at the domain points (stresses and strains) needs to be computed as a separate step, fully-populated, nonsymmetric matrices are generated and storage requirements and computational time grows with the square of the problem size. Furthermore, element integrals are more difficult to evaluate, some integrands become singular and pose problems even in the linear cases and it is much more difficult to implement than the FEM.

A further possibility is that proposed by Kennedy and Martins [63], which builds a kinematic description of the beam from a linear combination of fundamental state solutions. The first fundamental solutions are axially-invariant, and their corresponding deformation state is calculated at the mid plane of the beam by using a 2D finite-element method to obtain the stresses and strains due to the Saint-Venant (axial, bending, torsion and shear) [54] and Almansi-Michell (distributed surface load) loadings [55]. This method, improved from an earlier work by the authors

which only applied to orthotropic materials [64], yields solutions with accuracy comparable to that of full 3D analysis using the Finite-Element Method (FEM), for the interior solution, as long as the sections do not vary along the axis of the beam and the loads are statically determined.

It is worth noting that in the majority of the above contributions, the response of the beam is assumed static or quasi-static in order to obtain its stiffness. This is not always valid especially when interested in the vibratory response of beams where discretisation errors of the domain or of its boundary greatly affects the accuracy of the results when excitation frequency increases [108]. The dynamic stiffness of the structure needs then to be computed [69]. As large as fully populated 14×14 matrices can result from this approach which is mainly used in civil engineering applications: for concrete beams [78], circular columns [66] and sandwich beams [3]. These type of beams have substantially more material through the cross section than those present in aeronautical applications and hence the vibrational response requires this increase in modelling fidelity.

The previous solutions either were limited to constant-section geometries, required dedicated -and often quite involved- implementations, or user-created modules or subroutines in a standard finite-element solution package. Furthermore, the mentioned methodologies are linear approaches that therefore only provide strength estimates based on linear stress and strain distributions. Due to their high strength-stiffness ratio, composite thin wall structures usually exhibit local or distortional buckling before material failure [87] and this is often a design constraint.

1.1.2. Solution Stage: Geometrically Nonlinear Beam Models

Once an adequate set of cross-sectional properties has been obtained via any of the homogenisation methods described in the previous section, the dynamic equations of motion of the one-dimensional reference line that represents the slender structure must be solved. A great deal of effort has been put into developing composite beam

models and more comprehensive review of the available solution methods can be found in Chapter 1 of the treatise by Hodges [51].

The first geometrically nonlinear beam theories that were developed [24, 34, 43] were based on an inertial reference frame that included both the rigid-body motion and the structural deformations of the beam into a single expression. The kinematics for these beams were obtained as special cases of the general theory introduced by Cosserat and Cosserat [28] as described by Love [71] for extension, bending and twist and by Reissner [92] including transverse shear effects. The term "geometrically exact" is often used to describe the exact treatment of the parameterisation of the rotations of the cross-sectional frame. Euler angles were used by Reissner [92] with the consequent problems that their singularity poses. Quaternions, which are an extension of the complex numbers, from a plane to a three-dimensional space, can be used to deal with rotations and remedy the shortcomings of Euler angles. Simo and Vu-Quoc [98, 100] employed them to extend the methodology to fully three-dimensional dynamic cases. The resulting equations are based on displacement and finite rotation coordinates and solved with the finite element method. The same authors further improved the approach by including a global body-fixed reference frame to keep track of the large, unconstrained rigid-body motions of the beam in space [99, 101]. Cardona and Géradin [12, 40] used the Cartesian Rotation Vector (CRV) as an alternative to quaternions to express the sectional rotations. The CRV is a vector parallel to the rotation axis and whose amplitude is the rotation angle. Compared to quaternions, the CRV offers savings in storage and more favourable expressions for the linearisation of the rotation tensor [47].

Danielson and Hodges [30] introduced a crucial simplification to the models described above: they separated the cross-sectional rotations into their global and local components to represent the large rotations of the body-fixed frame and the small local rotations of the cross section respectively. This contribution facilitated the move from the displacement-based solutions described above to the more recent work that solves the geometrically-exact problem posing the equations in their

intrinsic, strain-based, variables [18, 95]. This approach allows the formulation of the problem in its state-space form, which, in the case of the formulation by Su and Cesnik [105], has a constant stiffness matrix. Naturally, this is numerically more efficient but it requires additional post-processing to obtain the displacements and rotations which can be a problem in a multibody configuration with arbitrary external constraints and loads [83].

The final consideration that must be made when dealing with large rotations is the objectivity of the description, that is the fact that the strain measures should remain constant regardless of how large the rigid-body motions are. Intrinsic formulations [49] assure this property but displacement-based ones violate it due to the inertial description of the beam kinematics, as demonstrated by Jelenić and Crisfield [29]. Their remedy is a co-rotational beam formulation that separates rotations into global, rigid-body ones and local, elastic ones [56] and introduces a new, local reference frame such that the local elastic deformations are always small with respect to this new frame. It is therefore possible to deal with large beam deflections while still having small strain measures locally [53] which facilitates the coupling of these beam solvers with homogenisation techniques.

1.2. Research Aims of the Thesis

The usefulness of a beam theory is determined by its applicability, the accuracy of its results and the effort required, both computationally and user wise, for the analysis [63]. The presented literature review clearly manifests the existence of a wide array of available methodologies for obtaining the homogenised properties of slender, beam-like structures. However, there is no comprehensive solution for complex-geometry composite slender structures, that can be seamlessly integrated into a standard geometrically-nonlinear beam solver.

Consequently, the objectives of the present work are the following:

1. To introduce a general methodology that evaluates the full elastic and inertial properties of composite beams with spanwise periodic characteristics (this eliminates the constant cross section simplification and it enables transverse reinforcements to be included).

2. To calculate additional strength parameters related to local buckling characteristics, such as skin wrinkling [106], and predict the nonlinear evolution of the stiffness constants as the geometry changes.

3. To define the above methodology in such a way that can be implemented into general-purpose finite-element code, thus taking advantage of all the advanced modelling features of the leading commercial packages. This has a great effect in the amount of time and effort saved if one wishes to perform parametric analysis or optimisation on the number/position/size of said reinforcements because it eliminates the need to re-mesh.

4. To demonstrate the integrability and computational suitability of the proposed technique by coupling it with a nonlinear composite beam solver [47] and comparing performance and accuracy against 3D analysis.

1.3. Present Approach

The methodology proposed in this dissertation to address the research objectives of the previous section is based on the static analysis of a unit cell, which is assumed to be much smaller than the characteristic wavelength in the beam response. Assumptions on the definition of the global variables as an average of the local ones and conservation of internal energy between scales yield a final set of equations to obtain the beam fully populated stiffness matrix, that is, including transverse shear effects. The solution will be sought using periodic boundary conditions in an off-the-shelf finite-element solver (Abaqus). The utilised models are generated automatically from a list of basic geometry parameters and assembled using tie constraints from substructures with non-coincident nodes, which considerably

simplifies model generations with a negligible impact on the homogenised properties. Inertial properties are also calculated on the discretised model by summing all the contributions from each element of the model. The solution method is also extended to certain geometrically-nonlinear (but still periodic) problems and coupled with a nonlinear composite beam solver for the calculation of tip deflections and (linear) normal modes.

1.4. Outline of the Thesis

Developing a homogenisation technique which is exclusively based on an unmodified, commercial, finite element, linear elastic analysis is an approach which requires a simple yet powerful and widely applicable formulation. The addition of the two transverse shear degrees of freedom is a strong challenge both from the theoretical as well as the implementation point of view. This dissertation is divided in three major sections: the theory description of the problem is encompassed in Chapter 2, the implementation using a standard finite element package plus a Python-based pre- and post-processor is included in Chapter 3 and the numerical examples used to demonstrate all the different capabilities of the method are separated into Chapter 4 (linear static analysis) and 5 (nonlinear and dynamic analyses). In more detail, each of the chapters contains:

Chapter 2 focuses on the development of a framework of homogenisation for slender periodic composite structures and the interaction with a geometrically-exact composite beam solver. It describes the kinematics of both the beam reference line and the representative unit cell and it postulates the equilibrium conditions between the two scales that allow the derivation of a set of periodic boundary conditions which define the static problem to be solved for the calculation of the stiffness properties. Additionally, it includes details about the determination of the inertial properties and the chosen method to apply the multipoint constraints that impose the periodic boundary conditions. Finally, Chapter 2 contains an overview of the method employed to solve the 1-D geometrically

nonlinear beam and how this is coupled to the methodology derived in this chapter.

Chapter 3 presents the implementation of the methodology developed in the previous chapter in a Python code named SHARP.cells which is part of the SHARP (Simulation of High-Aspect-Ratio Planes) aeroelastic framework. The code generated from this work uses Abaqus to solve the static problem on a representative unit cell and to obtain its elastic and inertial characteristics. An overview of the blocks involved in SHARP.cells is given in Chapter 3 with special emphasis on the geometry generation, which is a novel aspect of this approach, and the different types of analyses available thanks to the use of a commercial finite element package.

Chapter 4 contains the first set of numerical examples which validate the method for a number of cross sections of increasing complexity. It explores different material configurations ranging from isotropic aluminium to diverse composite layups with several materials in the same model. All test cases included in this chapter are subject to a linear static analysis and some of them have transverse reinforcements or variations in thickness along the beam's main direction.

Chapter 5 includes a selection of test cases that showcase some of the advanced features of this methodology in terms of analysis type. Buckling characteristics under both compressive and torsional loads are studied. The solutions obtained from a linear perturbation analysis (eigenvalue analysis) are compared to those obtained from a fully geometrically nonlinear one. Effects arising from localisation, present when the geometry of the whole structure is deformed past its (local) buckling point load, are analysed in this chapter too. Finally vibration modes and frequencies of a prismatic composite beam –obtained via the coupling established between SHARP.cells and the 1-D beam solver– are also presented in this chapter.

Chapter 6 summarises the key contributions and accomplishments of this work both in the theoretical development field or in the novel aspects of its numerical

implementation highlighted by the numerical examples. Additionally, it lists some recommendations for future work that will expand the capabilities of this approach and suggest further applications to be addressed.

Chapter 2

Theory

This chapter focuses on the development of a framework of homogenisation for slender periodic composite structures and the interaction with a geometrically-exact composite beam solver. Firstly, the kinematics of both the beam reference line and the representative unit cell are described in Section 2.1. Then, the equilibrium conditions between the two scales are postulated in Section 2.2 and this allows us to derive a set of periodic boundary conditions that define the static problem to be solved for the calculation of the stiffness properties. Acquiring the inertial properties is explained next. After that, two subsections (2.2.2 and 2.2.3) describe the method chosen to apply the multipoint constraints which impose the periodic boundary conditions and the justification behind the choice of constraints for the shear degrees of freedom. Finally, Section 2.3 contains an overview of the method employed to solve the 1-D geometrically-nonlinear beam and how this is coupled to the methodology derived in the aforementioned sections.

The one-dimensional, nonlinear beam solver calculates the response of the structure to a given set of forces and moments using Hamilton's principle, in which the kinetic energy, $\mathcal{T}$, and the internal (strain) energy, $\mathcal{U}$, per unit length are quadratic forms of the beam strains and velocities. These can only be accurately computed if the constant matrices that define them –the mass matrix, M, and the

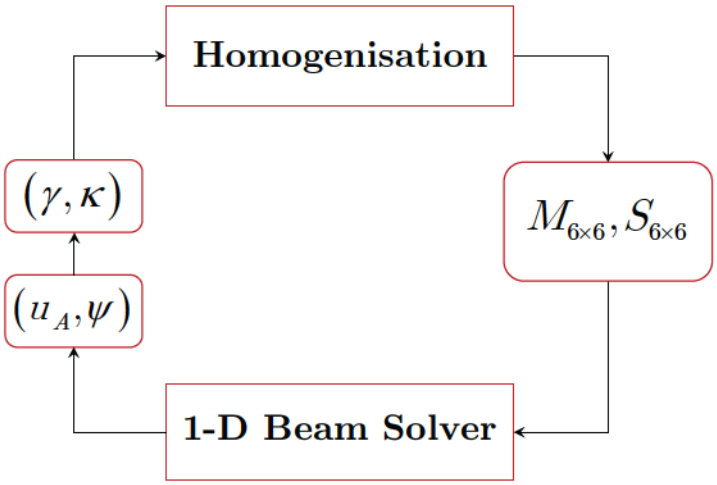

Figure 2.1.: Flow of information between the homogenisation methodology and the 1-D nonlinear beam solver.

stiffness matrix, S, respectively– are well known. The equations of motion are

$$\int_{t_1}^{t_2} \int_L [\delta\mathcal{T} - \delta\mathcal{U} + \delta W]\, dydt = 0 \tag{2.1}$$

where δW is the virtual work done by the external forces and moments. These quantities are integrated along the length of the beam, L, and the time interval of interest $[t_1, t_2]$.

The main objective of the methodology presented in this chapter is to obtain the full 6×6 stiffness matrix that characterises the elastic response of the 3D, detailed structure, when reduced to a 6 d.o.f. Timoshenko type of beam. The first section defines the kinematics of the beam and the unit cell and their relation. The second section explains the equilibrium conditions that apply on the unit cell so that a relation between the displacement on either sides of it can be derived. These displacement relations are in the form of periodic boundary conditions that are used to introduce each loading in the unit cell and, hence, linking the response with the input, the stiffness matrix is obtained. In the final section, considerations to extend this to nonlinear cases are detailed. This includes periodic buckling and the determination of real strains and curvatures calculated from the 1-D nonlinear

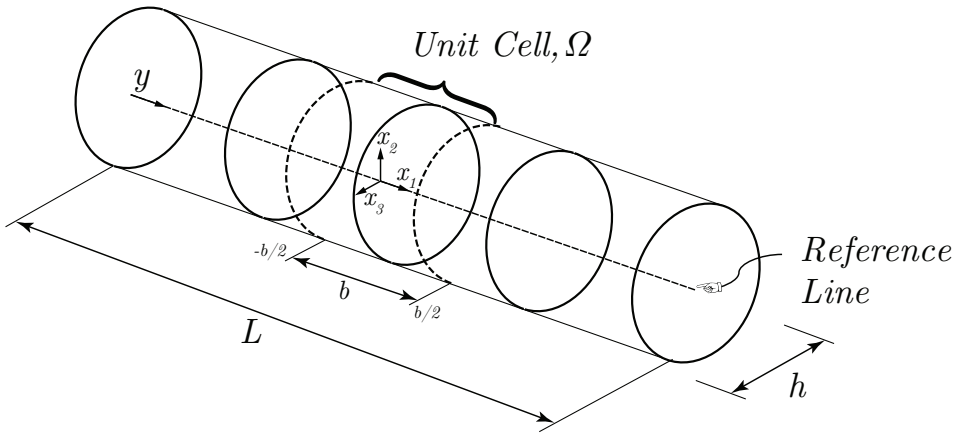

Figure 2.2.: Schematic diagram of a slender periodic structure consisting of repeated unit cells.

beam, that can then be used to either a) update the stiffness matrix or b) assess the structural integrity of the structure by comparing the local stresses and strains with the maximum allowed for a given material.

2.1. Kinematics

We define a slender prismatic solid as a longitudinal tessellation of a unit cell characterised by $-\frac{b}{2} \leq y \leq \frac{b}{2}$ (Figure 2.2). The beam-like nature of the structure is enforced by the transverse dimension, h, being much smaller than the longitudinal length of the beam, i.e. $h << L$. The coordinate y in the undeformed configuration is chosen to coincide with the neutral axis of the 1-D large scale (beam). The longitudinal dimension of the unit cell is $b << L$ and it is measured along the x_1 coordinate, which in the reference configuration lies along the large scale coordinate y. Small scale displacements associated with x_i are named v_i and large scale displacements of the reference line, y, are designated u_i. The beam stiffness

constants are obtained based on two assumptions between the scales [39]: a) the large (1-D beam) scale variables (u_i) are averages of the small (3-D unit cell) scale ones (v_i), and b) the deformation energy is conserved between scales. All throughout this section, Einstein notation is used for repeated indices, with Latin indices assuming values from 1 to 3 and Greek ones assuming values of 2 and 3. $e_{\alpha\beta}$ is the Levi-Civita or permutation symbol which takes the following values: $e_{23} = 1, e_{32} = -1$ and $e_{22} = e_{33} = 0$.

Under linear assumptions, the deformation of the reference line can be described by three local displacements $u_i(y)$ and three local rotations $\theta_i(y)$ along the axes x_i of the coordinate system in Figure 2.2. The beam strain measures are obtained from linearisation of the strain-displacement kinematic relations in [83], as

$$\begin{aligned} \gamma_1(y) &= u_1^{'}, \\ \gamma_\alpha(y) &= u_\alpha^{'} - e_{\alpha\beta}\theta_\beta, \\ \kappa_i(y) &= \theta_i^{'}. \end{aligned} \tag{2.2}$$

where $\bullet'$ denotes spatial derivatives along arc length, $\frac{d}{dy}$. The fact that this theory includes transverse shear, $\gamma_\alpha(y) \neq 0$, implies $\theta_2 \neq -u_3^{'}; \theta_3 \neq u_2^{'}$. This is equivalent to saying that the cross sections are no longer perpendicular to the reference line and the shear strain has two contributions: the angle arising from the deformation of the reference line ($u_\alpha^{'}$) and the angle created between the cross-sectional plane and the reference line (θ_β). We define the vector of beam strains containing extensional strain γ_1, transverse shear strain in two directions γ_2, γ_3, torsional curvature κ_1 and bending curvatures in two directions κ_2, κ_3, as

$$\epsilon^T = \begin{Bmatrix} \gamma_1 & \gamma_2 & \gamma_3 & \kappa_1 & \kappa_2 & \kappa_3 \end{Bmatrix}. \tag{2.3}$$

At the small scale level, we consider the 3-D deformation of a cell of volume Ω centered at y (see Figure 2.2). The undeformed position within the cell will be given by coordinates x_i, where x_1 is parallel to y, but measures lengths at cell scales (i.e. $\dfrac{dx_1}{dy} = \dfrac{b}{L}$) and it can be seen as a magnified coordinate system [11]. The

three components of the small scale displacement field are $v_i(y; x_1, x_2, x_3)$. The two longitudinal dependencies are introduced to separate between *small scale* ($\sim x_1$) and *large scale* fluctuations ($\sim y$) of the structural deformations [68]. The warping field, w_i is then defined as the difference between the small and large scale displacement fields, as

$$\begin{aligned} v_1(y; x_1, x_2, x_3) &= u_1(y) - e_{\alpha\beta} x_\alpha \theta_\beta(y) + w_1(y; x_1, x_2, x_3), \\ v_\alpha(y; x_1, x_2, x_3) &= u_\alpha(y) - e_{\alpha\beta} x_\beta \theta_1(y) + w_\alpha(y; x_1, x_2, x_3). \end{aligned} \tag{2.4}$$

Note that if the warping field is zero, Eq.(2.4) is the kinematic assumption used in Timoshenko beam theory. In general, the warping field depends on the cell and, consequently, it was explicitly written as a function of the spanwise coordinate, y.

The independent large scale variables are defined from averages in the cell, as

$$\begin{aligned} u_i(y) &= \langle v_i \rangle , \\ \theta_1(y) &= \tfrac{1}{2} \langle v_{3,2} - v_{2,3} \rangle , \\ \theta_\alpha(y) &= e_{\alpha\beta} \langle v_{1,\beta} \rangle . \end{aligned} \tag{2.5}$$

where $\langle \bullet \rangle = \frac{1}{\Omega} \int_\Omega \bullet dx_1 dx_2 dx_3$ and $\bullet_{,j} = \frac{\partial \bullet}{\partial x_j}$. Assuming that the reference axis is at the centroid of the cell, i.e. $\langle x_\alpha \rangle = 0$, these definitions impose six constraints on the warping field,

$$\begin{aligned} \langle w_i \rangle &= 0, \\ \langle w_{2,3} - w_{3,2} \rangle &= 0, \\ \langle w_{1,\alpha} \rangle &= 0. \end{aligned} \tag{2.6}$$

The choice of homogenising the stiffness properties about the centroidal axis is not a limitation of the theory but rather an advantage that simplifies the formulation when dealing with rotations.

2.2. Equilibrium Conditions

Our interest is in the interior solution of the problem, that is the response of the majority of the beam which is not subject to end effects [52] or concentrated loads, to obtain the 6×6 homogenised cross-sectional stiffness matrix, S. It will be enforced by assuming constant large scale strains, that is, $\epsilon(y) = \bar{\epsilon}$, which effectively correspond to the fundamental solutions from Kennedy and Martins [63]. We then postulate constitutive relations in the homogenised problem such that the strain energy is conserved between the small and large scale levels [39]. Due to the periodicity of the problem, the large scale strain energy per unit beam length is independent of the cell in the interior solution, and it is

$$\mathcal{U} = \frac{1}{2}\bar{\epsilon}^T S \bar{\epsilon} = \frac{1}{2b}\int_\Omega \mathcal{C}_{ijkl}\varepsilon_{ij}\varepsilon_{kl} dx_1 dx_2 dx_3, \tag{2.7}$$

with $\mathcal{C}_{ijkl}$ being the material elasticity tensor and $\varepsilon_{ij} = \frac{1}{2}(v_{i,j} + v_{j,i})$ the components of the small scale strain tensor. Define now the magnitudes $\Delta v_i = v_i(y; \frac{b}{2}, x_2, x_3) - v_i(y; -\frac{b}{2}, x_2, x_3)$ which represent the difference in the local displacement field between corresponding points on either boundary surface of the unit cell. Eq.(2.4) becomes

$$\begin{aligned} \Delta v_1(y; x_2, x_3) &= \bar{\gamma}_1 b - e_{\alpha\beta} x_\alpha \bar{\kappa}_\beta b + \Delta w_1(y; x_2, x_3), \\ \Delta v_\alpha(y; x_2, x_3) &= \bar{\gamma}_\alpha b + \tfrac{b^2}{2} e_{\alpha\beta}\bar{\kappa}_\beta - e_{\alpha\beta} x_\beta \bar{\kappa}_1 b + \Delta w_\alpha(y; x_2, x_3). \end{aligned} \tag{2.8}$$

The second term on the right hand side of the second equation in Eq. (2.8) ($\frac{b^2}{2} e_{\alpha\beta}\bar{\kappa}_\beta$) comes from double integration of shear-related terms in Eq. (2.2). Firstly, the curvatures ($\kappa_i(y) = \theta_i'$) are integrated once and substituted into ($\gamma_\alpha(y) = u_\alpha' - e_{\alpha\beta}\theta_\beta$). Then, u_α is found by integrating again. These terms denote the coupling of bending curvatures and transverse shear and would not appear in an Euler-Bernoulli theory in which cross sections remain perpendicular to the reference line: $\theta_2 = -u_3'$ and $\theta_3 = u_2'$. For this solution to be independent of the cell, it must be $\Delta w_i(y; x_2, x_3) = 0$, i.e. the warping field is periodic. This is equivalent to saying that, due to periodicity, the strain field must be compatible and the only difference in displacement allowed between both faces of the cell is a rigid body motion, which

does not create strain. We are finally left with the problem of obtaining the static equilibrium conditions on a generic cell under an applied displacement field given by

$$\begin{aligned} v_1(\tfrac{b}{2}; x_2, x_3) &= v_1(-\tfrac{b}{2}; x_2, x_3) + \bar{\gamma}_1 b - e_{\alpha\beta} x_\alpha \bar{\kappa}_\beta b, \\ v_\alpha(\tfrac{b}{2}; x_2, x_3) &= v_\alpha(-\tfrac{b}{2}; x_2, x_3) + \bar{\gamma}_\alpha b + \tfrac{b^2}{2} e_{\alpha\beta} \bar{\kappa}_\beta - e_{\alpha\beta} x_\beta \bar{\kappa}_1 b. \end{aligned} \tag{2.9}$$

where the reference to the long-scale coordinate, y, is no longer necessary. This problem can be set up in any standard FEM solver using multipoint constraints to enforce the periodic boundary conditions defined by Eq. (2.9). See Subsection 2.2.2 for more details on multipoint constraints. Loading to the structure is introduced via displacements, not forces.

Twenty-one different combinations of loading cases are then considered, corresponding to unit values in each of the six components of the beam strain $\bar{\epsilon}$, and unit values in each of the fifteen possible different pairs of strains and curvatures (e.g., coupled axial/torsion, axial/shear, etc.). For each load state, the strain energy of the whole unit cell is computed after a linear elastic analysis using the right hand side of Eq.(2.7). This strain energy corresponds *exclusively* to the degree(s) of freedom excited in a given loading case. When direct terms from the stiffness matrix are being considered, the strain energy per unit length and the single strain or curvature value chosen to load the unit cell uniquely determine that stiffness diagonal term. The off-diagonal terms can be calculated using the difference in strain energy levels that exists between a unit cell loaded *simultaneously* in two degrees of freedom and the sum of strain energy of that same unit cell loaded in the same two degrees of freedom but *separately*. Please note that the reaction forces or moments are not needed to solve the twenty-one independent coefficients of the stiffness matrix, S, in Eq.(2.7).

In order to capture transverse shear correctly, an additional constraint corresponding to the last term of Eq.(2.6) is needed. This is the case because the shear loading is not statically determinate and is linked to a bending moment, or

rotation (see Eq. (2.2)). If, for example, γ_2 is to be imposed as a periodic loading, the associated rotation, θ_2, must be zero to decouple the energy from pure shear from that of bending. This means that for every section, θ_α is nullified but in an *average* manner (see Eq. (2.5)) such that section warping is still allowed. This converts shear loadings into *periodic* loadings. The average rotation constraint is conveniently enforced via a zero average first moment (which is numerically well-posed and proven to be equivalent to a zero average rotation in Subsection 2.2.3) for each section as

$$\int_\Omega u_1 x_\alpha \, dx_2 dx_3 = 0 \quad \text{if} \quad \gamma_\alpha \neq 0. \tag{2.10}$$

2.2.1. Inertial Properties

The inertial properties of the section are given by the mass matrix, M, which is defined as

$$M = \begin{bmatrix} m & m\widetilde{x}_{cg} \\ m\widetilde{x}_{cg} & J \end{bmatrix}, \tag{2.11}$$

where m is the mass per unit length, $\widetilde{x}_{cg}$ is is the location of the centre of gravity and J are the cross-sectional moments of inertia. They are defined as

$$J_{ij} = \frac{1}{b} \int_\Omega \rho \xi_i \xi_j^T dV, \tag{2.12}$$

with ρ as the local density, b is the unit cell spanwise length, $\xi = (0 \; x_2 \; x_3)$ as the axially-invariant position vector and dV as the infinitesimal volume associated with the unit cell domain Ω. It is worth noting that all the calculations required for the mass properties are done on the discretised model.

2.2.2. Multipoint Constraints

The static problem which is the backbone of this formulation – defined by the set of periodic boundary conditions in Eq. (2.9) –, that will lead to the calculation of the 6×6 stiffness matrix, is implemented in a standard finite element solver using multipoint constraints. These can be introduced via static condensation [110],

also known as partial Gauss elimination or substructuring, Lagrange multipliers and penalty functions [25]. The first method, as implemented in Abaqus, is utilised here and hence will be explained in detail.

We begin from the standard structural equation

$$\left[\overline{K}\right]\left\{\overline{D}\right\} = \left\{\overline{R}\right\}, \tag{2.13}$$

where $\overline{K}$ is the original (before the multipoint constraints are applied) global stiffness matrix, $\overline{D}$ is the original full vector of degrees of freedom and $\overline{R}$ is the original full vector of forces. Assume that there are c independent multipoint constraints, C_c, expressed by the matrix relation:

$$\begin{bmatrix} C_r & C_c \end{bmatrix} \begin{Bmatrix} D_r \\ D_c \end{Bmatrix} = \left\{0\right\}, \tag{2.14}$$

where the full vector of degrees of freedom, D, is split between those retained, D_r, and those condensed, D_c. There must be an equal number of independent equations to the number of degrees of freedom to eliminate and therefore $[C_c]$ is square and can be inverted. The condensed degrees of freedom can be expressed in terms of the retained ones as:

$$\left\{D_c\right\} = \left[C_{rc}\right]\left\{D_r\right\} \quad \text{where} \quad [C_{rc}] = -\left[C_c\right]^{-1}\left[C_r\right]. \tag{2.15}$$

We define the transformation matrix, $[T]$, that is to be applied to the original stiffness matrix, $[K] = [T]^T \left[\overline{K}\right][T]$, and the original force vector, $\{R\} = [T]^T \left\{\overline{R}\right\}$, in Eq. (2.13) as:

$$\begin{Bmatrix} D_r \\ D_c \end{Bmatrix} = \left[T\right]\left\{D_r\right\} \text{ with } \left[T\right] = \begin{bmatrix} \mathbb{I} \\ C_{rc} \end{bmatrix}. \tag{2.16}$$

We also partition said structural equation similarly to Eq.(2.14):

$$\begin{bmatrix} K_{rr} & K_{rc} \\ K_{cr} & K_{cc} \end{bmatrix} \begin{Bmatrix} D_r \\ D_c \end{Bmatrix} = \begin{Bmatrix} R_r \\ R_c \end{Bmatrix}. \tag{2.17}$$

Finally, the condensed system is:

$$\left[K_{rr} + K_{rc}C_{rc} + C_{cr}^{T}K_{cr} + C_{rc}^{T}K_{cc}C_{rc}\right]\left\{D_r\right\} = \left\{R_r + C_{rc}^{T}R_c\right\}. \tag{2.18}$$

Overall, the static condensation technique reduces the number of equilibrium equations to be solved but it requires significant manipulation and it usually increases the bandwidth of the condensed stiffness matrix [26]. As described in Wilson [111], there are two other methods for imposing multipoint constraints: Lagrange multipliers and the Penalty method. Their advantages and disadvantages will be summarised next:

- The method of Lagrange's undetermined multipliers is used to find the maximum or minimum of a function whose variables are not independent but have some prescribed relation. It solves the constraint equations *exactly* and is especially suited if there are a *few* constraint equations that couple *many* d.o.f. The transformation can be carried out element by element when the matrices are still small and more manageable. The down side is that it increases the number of variables and the size of the matrices [25].

- The Penalty method introduces constraints by creating semi-rigid links that satisfy the structural equations in their variational formulation. It does not modify the number of variables but it solves the constraint equations approximately. Additionally, it increases the wavefront of the structural matrix and requires the penalty numbers to be chosen carefully to avoid numerical issues [88].

2.2.3. Equivalence between Zero Average First Moment of Area and Zero Average Rotation

The following mathematical proof demonstrates the equivalence between applying a zero average first moment of area constraint, α, and a zero average rotation constraint, β. Applying a zero average rotation is crucial in order to eliminate the strain energy corresponding to the bending degree of freedom but without

modifying the local warping field, hence the average approach. Consider a simplified, rectangular cross section with dimensions of unit width and $2h$ height (the area is $A = 2h$). Then we obtain the moment of area and the rotation measures, α and β, as:

$$\alpha = \frac{1}{A^2} \int v_1(x_2)\ x_2\ dx_2\ ;\ \beta = \int \frac{v_1(x_2) - \overline{v_1}}{x_2}\ dx_2. \tag{2.19}$$

Normalising the moment of area measure, α, by the square of the area so that both α and β have dimensions of length, it is possible to subtract one from the other:

$$\begin{aligned} \alpha - \beta &= \int \left[v_1(x_2)\ \left(\frac{x_2}{A^2} - \frac{1}{x_2} \right) + \frac{\overline{v_1}}{x_2} \right] dx_2 = \\ &= \int v_1(x_2)\ \left(\frac{x_2}{A^2} - \frac{1}{x_2} \right)\ dx_2 + \overline{v_1} \int_{-h}^{h} \frac{1}{x_2}\ dx_2. \end{aligned} \tag{2.20}$$

Integrating by parts and evaluating:

$$\begin{aligned} &= \int_{-h}^{h} v_1\ dx_2 \left[\frac{x_2}{A^2} - \frac{1}{x_2} \right]_{-h}^{h} - \int A\overline{v_1} \left(\frac{1}{A^2} - \frac{1}{x_2^2} \right) dx_2 + \cancelto{0}{\overline{v_1}} = \\ &= A\ \overline{v_1} \left(\frac{A}{A^2} - \frac{4}{A} \right) - \overline{v_1} - A\ \overline{v_1} \int \frac{1}{x_2}\ dx_2 = \\ &= \overline{v_1}(1 - 4) - \overline{v_1} + A\ \overline{v_1} \left[\frac{1}{x_2} \right]_{-h}^{h} = 0. \end{aligned} \tag{2.21}$$

Hence it is proven that enforcing a zero average first moment of area results in the same response as a zero average rotation (but without the numerical problems). This can be extended to any arbitrary cross section as long as the reference line coincides with the centroidal axis.

2.3. Extension to Geometrically-nonlinear Problems and Two-way Coupling with a 1-D Beam Solver

The previous formulation can be directly extended to geometrically-nonlinear problems in two situations: Firstly, when there are geometrically-nonlinear effects at the cell level but the solution is still periodic; and, secondly, when the nonlinear effects appear in the macroscopic scale but relative displacements are still small at the local (cross-sectional) scale. The first problem is representative of panel buckling or skin wrinkling in an aircraft wing. This is a local phenomenon that

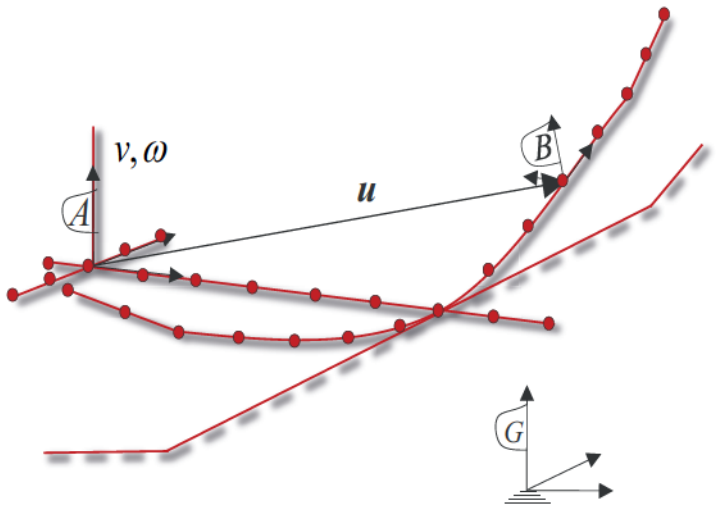

Figure 2.3.: Beam representation of a HALE aircraft with the frames of reference used in the GECB code [47]. G is the Earth's reference frame, A is the body-fixed frame and B is the local reference frame.

may not break periodicity and it is assumed that all cells undergo the same level of loading and buckling initiates simultaneously in all of them. The second problem appears when we are interested in updating the stiffness and mass properties used in geometrically-nonlinear beam modelling. In order to study the effect of fully populated 6×6 stiffness (with shear effects) and mass matrices, the current methodology is coupled to a geometrically-exact composite beam (GECB) model [83]. This beam model is used to represent all primary structures of the aircraft by curvilinear, composite (anisotropic) beams that are capable of large deformations and global rotations [102]. The body-fixed, main coordinate frame of the one-dimensional beam, A, is at the reference line denoted by the y coordinate shown in Figure 2.3. We define a local, deformed coordinate system, B, at each flexible member of the beam. Vectors in three-dimensional space are bold while their components are written in italics with a subindex indicating the reference frame in which they are projected. In order to parameterise the relative orientation between the two frames, the coordinate transformation matrix $C^{BA}(y,t) = C(\Psi)$ is used. It is defined as:

$$C = \mathbb{I} + \frac{\sin\phi}{\phi}\tilde{\Psi} + \frac{1-\cos\phi}{\phi^2}\tilde{\Psi}^2 = \sum_{k=0}^{\infty}\frac{1}{k!}\tilde{\Psi}^k, \tag{2.22}$$

where $(\widetilde{\bullet})$ is the cross-product or skew-symmetric operator and Ψ is the Cartesian Rotation Vector (CRV). This rotation vector is defined based on Euler's rotation theorem, which states that any sequence of rotations of a rigid body about a given point are equivalent to a single rotation, ϕ, about some unit vector, n, which passes through that point: $\Psi = \phi n$. Ψ tracks the local orientations of the cross-sections and, similarly, u_A tracks their positions. u_A (see Figure 2.3) is the position vector that determines the instantaneous location of a point in the deformed structure with respect to the body-fixed reference frame, A, expressed in its components in its body-fixed frame. For instance, for a rigid body with rigid body motions, this vector would be constant. Ψ and u_A are the independent set of variables in this formulation. We define the *tangential rotation operator*, T, that obtains the local curvature, K_B, from the local orientation, Ψ, as $K_B = T(\Psi)\Psi'$ –where $(\bullet')$ is the spatial derivative with respect to the y coordinate. Hence, $T(\Psi)$ can be obtained in closed form from the CRV as [101]

$$T = \mathbb{I} + \frac{\cos\phi - 1}{\phi^2}\widetilde{\Psi} + \left(1 - \frac{\sin\phi}{\phi}\right)\frac{\widetilde{\Psi}^2}{\phi^2} = \sum_{k=0}^{\infty}\frac{(-1)^k}{(k+1)!}\widetilde{\Psi}^k. \tag{2.23}$$

Having $T(\Psi)$ allows us to formulate relations between the local positions and rotations and the beam strains and curvatures. This is a very important step as it provides the necessary input data for the homogenisation tool. The relations between the local positions and rotations and the beam strains and curvatures are [49]

$$\begin{aligned}\gamma(y,t) =& C(\Psi(y,t))u'_A(y,t) - C(\Psi(y,0))u'_A(y,0),\\ \kappa(y,t) =& T(\Psi(y,t))\Psi'(y,t) - T(\Psi(y,0))\Psi'(y,0).\end{aligned} \tag{2.24}$$

Similarly, the local translational and angular velocities that constitute the inertial properties of the beam can be calculated as

$$\begin{aligned}V_B(y,t) &= C\left(\Psi(y,t)\right)\dot{u}_A(y,t) + C\left(\Psi(y,t)\right)\left[v_A(t) + \widetilde{\omega}_A(t)u_A(y,t)\right],\\ \Omega_B(y,t) &= T\left(\Psi(y,t)\right)\dot{\Psi}(y,t) + C\left(\Psi(y,t)\right)\omega_A(t),\end{aligned} \tag{2.25}$$

where $(\dot{\bullet})$ is the temporal derivative with respect to t, v_A and ω_A are the translational and angular velocities of the body-fixed frame.

Using Hamilton's principle, the dynamics of the beam in a time interval $[t_1, t_2]$ were given at the beginning of this chapter as

$$\int_{t_1}^{t_2} \int_L [\delta\mathcal{T} - \delta\mathcal{U} + \delta\mathcal{W}]\, dydt = 0, \tag{2.26}$$

where $\mathcal{T}$ and $\mathcal{U}$ are the kinetic and strain energy densities respectively. L for a full aircraft such as that from Fig. 2.3 is the sum of lengths of all the individual beams that compose the aircraft. The energies can be written as [49]

$$\begin{aligned} \delta\mathcal{U} &= \begin{bmatrix} \delta\gamma^\top & \delta\kappa^\top \end{bmatrix} S \begin{bmatrix} \gamma^\top & \kappa^\top \end{bmatrix}^\top, \\ \delta\mathcal{T} &= \begin{bmatrix} \delta V_B^\top & \delta\Omega_B^\top \end{bmatrix} M \begin{bmatrix} V_B^\top & \Omega_B^\top \end{bmatrix}^\top. \end{aligned} \tag{2.27}$$

After additional manipulation (see Appendix A for details), a finite element approximation with linear or quadratic interpolation (2 or 3 nodes per element respectively) is used. The nodal displacements and rotations are grouped into the variable η and velocities are grouped as $\beta^\top = \{v_A^\top \quad \omega_A^\top\}$. Equation (2.26), can be written in discrete form as

$$\mathcal{M}(\eta) \begin{Bmatrix} \ddot{\eta} \\ \dot{\beta} \end{Bmatrix} + \begin{Bmatrix} Q_{gyr}^S \\ Q_{gyr}^R \end{Bmatrix} (\eta, \dot{\eta}, \beta) + \begin{Bmatrix} Q_{stif}^S \\ 0 \end{Bmatrix} (\eta) = \begin{Bmatrix} Q_{ext}^S \\ Q_{ext}^R \end{Bmatrix} (\eta, \dot{\eta}, \beta, \zeta), \tag{2.28}$$

where ζ is the orientation of the A-frame measured in terms of quaternions, integrated from its angular velocity, ω_A. The top row corresponds to structural effects and the bottom one to rigid-body ones. From left to right we have inertial, gyroscopic, stiffness and external loading terms. If N_e is the number of nodes, the size of the vector of nodal variables, $\eta(y,t)$, is $6 \cdot N_e$. These equations are solved using Newmark-β in [47]. If we now linearise the equations for $\beta = 0$, the final discretised form of the equations of motion is

$$\mathcal{M}(\eta_0)\ddot{\overline{\eta}} + \mathcal{K}(\eta_0)\overline{\eta} = \overline{Q}_{ext}, \tag{2.29}$$

where $\overline{\eta}$ refers to perturbations around an equilibrium condition η. $\mathcal{M}(\eta_0)$ and $\mathcal{K}(\eta_0)$ are the assembled global mass and stiffness matrices. $\mathcal{K}(\eta_0)$ is related to Q^S_{stiff} as $\mathcal{K}(\eta_0) = \frac{\partial Q^S_{stiff}}{\partial \eta}\Big|_{\eta=\eta_0}$ calculated in the 1-D beam solver using the element-wise matrices obtained through the homogenisation step. When $\overline{\eta}$ is known at a given time step, it is used to compute strains and curvatures using Equation (2.24) and the homogenisation technique discussed in sections 2.1 and 2.2 is once more used to provide updated stiffness and mass matrices, closing the loop. More details about the flow of information from the beam solver to the homogenisation step and vice versa can be found in Section 3.2.

Chapter 3

Numerical implementation

The homogenisation methodology developed in Chapter 2 has been implemented in a Python code named SHARP.cells which is part of the SHARP (Simulation of High-Aspect-Ratio Planes) aeroelastic framework [27, 47, 77, 79]. SHARP is a multidisciplinary framework for the simulation of novel flexible aircraft configurations and large offshore wind turbines. Such highly-efficient platforms can exhibit very large deformations which are captured accurately with this high-fidelity simulation tool developed in Python, Matlab and Fortran. SHARP includes a range of powerful capabilities for the simulation of very flexible aircraft with large wing deformations: trim computations, open- and closed-loop dynamic response, gust and manoeuvre loads, linear stability analyses, robust flutter suppression, gust load alleviation and real-time simulations. SHARP.cells uses Abaqus to solve the problem defined in Eq.(2.8) by applying Eq.(2.9) and Eq.(2.10). The code outlined in this chapter is effectively a wrapper around a standard, unmodified finite element package. Firstly, it creates or imports the geometry of the unit cell. Secondly, it sets the right periodic boundary conditions for the finite element analysis and, finally, it post-processes that information to calculate, primarily, the elastic and inertial properties of the equivalent 1-D beam. Furthermore, it can also compute additional characteristics such as buckling loads, post-buckling stiffness or vibration modes, to name a few. It is important to note that, unlike the methodology proposed by

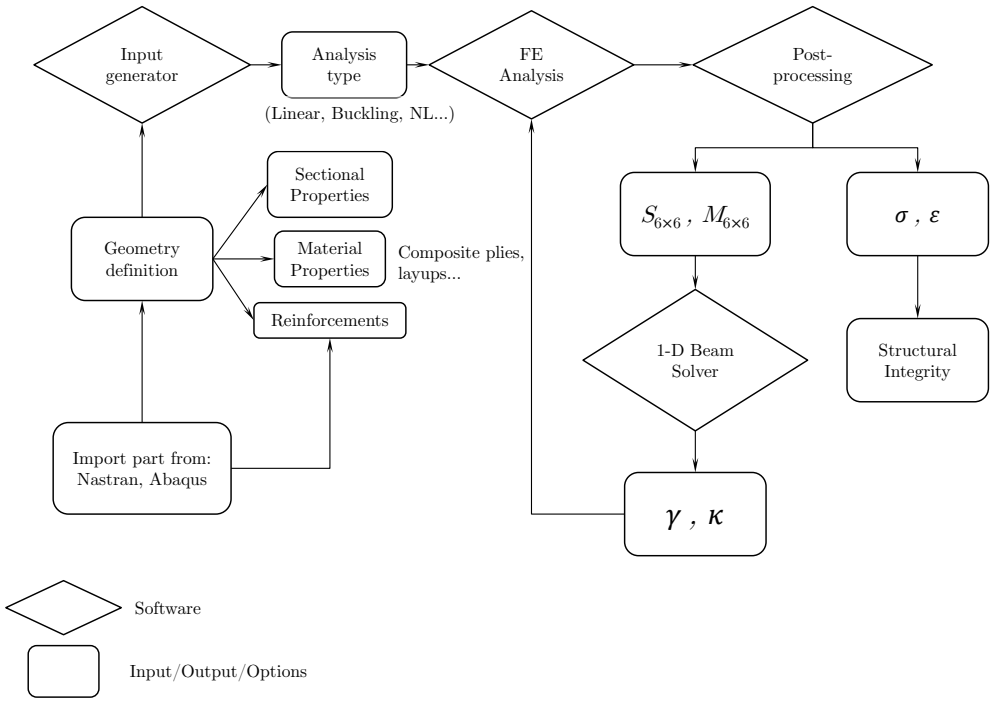

Figure 3.1.: Flow of information between the different modules of SHARP.cells

Giavotto et al [42], the solution procedure of the finite element packaged remains unmodified in this approach and internal reinforcements can be analysed.

This chapter describes details of the implementation and software architecture, including the interaction with the finite element package and the nonlinear beam solver SHARP.beams. It also contains information about the modules and functions that it uses, the format and content of its input and output files, the modelling conventions and some performance considerations.

3.1. Description of the Python Code

Python was chosen as the scripting language for the implementation of the dimensional reduction of slender periodic composite structures for several reasons. Firstly, it is the language employed in Abaqus to store and organise all the information in the output database and therefore it is very convenient to use it to

request the analysis data natively without invoking the graphical interface. Secondly, it is a highly-readable, clean and compact language which is widespread in the scientific community and has many scientific packages ready available. Thirdly, it is free, open source and OS-independent. Thanks to its compactness, the necessary code written for this application has a combined line count of just over 3000 lines, with three main files and 22 modules, 16 of which are originally developed and 6 are external modules (mainly from NumPy [80] and one piece of C code used for Delaunay triangulation and meshing called Triangle [96]).

The main structure of the program is shown in Figure 3.1. The higher level script, which governs everything else, calls the preprocessor to generate the input file (more details in section 3.1.1). After that, it creates an Abaqus job using the generated input file and sends it to the Abaqus's solver (this process is carried out automatically in both Windows and Linux). The number of cores (or threads) and maximum RAM to be used are determined in this step. More details on the computational performance of the code can be found in section 3.1.5. Finally, it uses the post-processor to access the output database (an Abaqus `.odb` file) and calculates the required properties. It is also this module that controls the interactions with the 1-D beam solver and can run loops for parametric analysis using the aforementioned sub-files.

The bulk of the effort from this work comprises the pre- and post-processor files and these will be described in further detail below.

3.1.1. Program Input/Output

In this section we distinguish between the input required for the Python code to work and the input file created to be used by the finite element package. Similarly the output from the code is not the same as the output from the FE solver, although it is naturally based on this.

The first part, or pre-processor, performs the following tasks: it creates the geometry of the unit cell, assigns the material properties and sections and creates

all 21 load cases that will be run in the static analysis and any additional ones that may be requested such as a linear perturbation step or nonlinear steps.

3.1.2. Geometry Generation

The geometry generation is based on a 2D planar surface which is then automatically extruded to create the unit cell. Thickness variations and transverse reinforcements can be added during and after the extrusion stage respectively. The two-dimensional cross section can be defined as:

a) A set of coordinates corresponding to the outer contour of the surface (represented with squares in Fig. 3.2). Linear interpolation is assumed between these «master corners» and a variable number of intermediate nodes can be automatically created for additional refinement (represented with circles in Fig. 3.2). If the section is composed of thin walls, the skin is meshed and its thickness (measured from the outer wall) is required as an input: for composite layups, this is the thickness of a single ply and the number of plies is automatically understood from the layup configuration (see Subsection 3.1.3). The skin is meshed first and further reinforcements can be added later. On the other hand, if the section is solid, a Delanauy triangulation [96] is performed and no further parts can be added (see Fig. 3.2 for an example of a solid NACA-4412 section meshed defined with 21 main coordinates and 221 elements per section, 663 in total). There are a variety of modules that have been included to facilitate the generation of the most common shapes, including aerofoils. For example, `circ2cart.py` includes a simple function of the same name that creates a thin walled cylinder centered at the origin. It takes as arguments the outer radius and the thickness of the cylinder. `naca.py` is a more sophisticated suite of functions which allows creating any 4- or 5-digit NACA profile by simply specifying these digits and the number of points as arguments of the function.

b) Geometry imported directly from UM/VABS [82] or Nastran style input files. These are accepted directly as long as valid geometry, in text format, is

contained within. At the time of writing SHARP.cells exclusively recognises the keywords `GRID`, `CQUAD8`, `MAT3D` and `PSHELL` as accepted inputs for nodes, element connectivities, material properties and section assignments respectively. [74]

c) Any combination of pre-meshed parts –including those generated in a)– that are then bonded together using tie constraints. This includes parts generated in any CAD preprocessor that follows the Abaqus format for the description of the mesh. description or any reinforcement from the included libraries to add spars, stringers and ribs (`spar.py, stringer.py and rib.py` respectively). For the homogenisation step, details such as stress concentrations at joints have a very small effect in the beam stiffness constants (as they are averaged over the whole unit cell volume). Therefore, the meshing can be done independently for the various subcomponents of the cells without affecting the accuracy of the solution. Matching nodes are not required and both master (inner surface of the skin) and slave surfaces (reinforcement) are bonded via tie constraints in the Abaqus model [103].

In general, the models are meshed using 'C3D8R' (3D-cuboid-8node) elements, with reduced integration for the calculation of the linear stiffness properties. Reduced integration uses only one integration point (Gauss point) and is computationally cheaper than full integration at the expense of less accuracy. Full integration is used for buckling analysis or complicated geometries such as the ATR blade in Figure 4.12 in Section 4.3. This is to remedy hourglassing, which usually occurs in the complex buckling deformed shapes. The only exception to this is a solid section generated with a) and discretised using Delaunay triangulation; in this case 'C3D6' (3D-wedge-6node) elements are used.

3.1.3. Material Properties

In terms of material properties, SHARP.cells handles isotropic, orthotropic or fully anisotropic materials using Abaqus convention for their definition. For the anisotropic cases, each element has its own local coordinate system that defines the

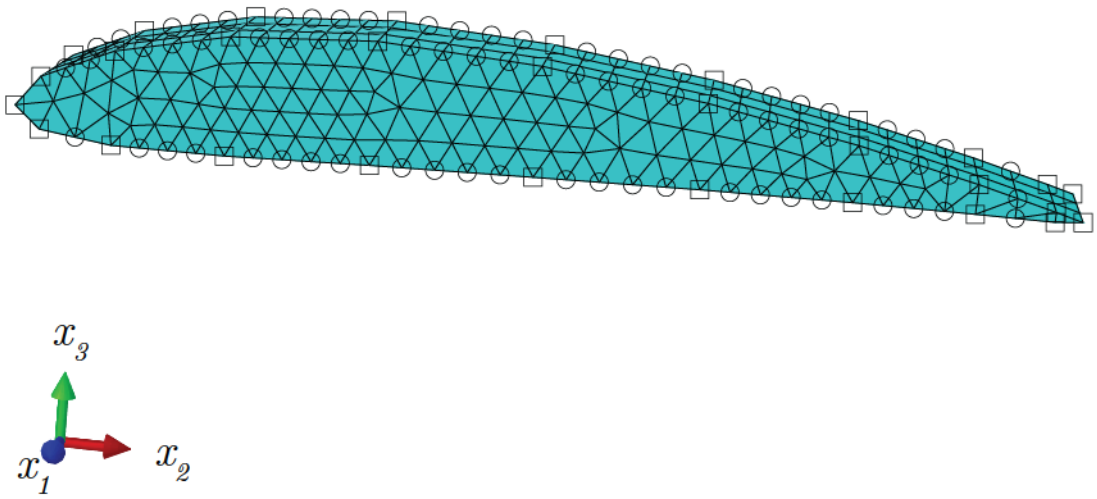

Figure 3.2.: Unit cell finite-element discretisation of a solid NACA-4412 profile meshed using Delaunay triangulation. Squares represent the master nodes of the geometry and circles depict those nodes created between squares in a linear interpolated fashion[1].

ply orientation. The 0-degree axis runs parallel to the x_1 axis and positive angles are measured clockwise around x_3. Each composite ply is modelled with a layer of elements and SHARP.cells understands standard composite layup notation (i.e. $[0,90]_3$).

The inertial properties of the section are calculated on the discretised model in the pre-processing stage and, as it stands, SHARP.beams cannot update the mass matrix with deformed geometries.

3.1.4. Analysis Types

The only remaining parameter to be defined before the input file is generated is the type of analysis to be performed. The following list contains an enumeration of all the possible analysis and the codes involved in each of them:

[1]Please note that the profile is in 3D and master nodes are shown on both the front and the back face of the unit cell. There are three elements through the depth of it.

Linear This is the standard linear elastic analysis used to calculate the 6×6 mass and stiffness matrices and it is performed by default. Adding the keyword '`static`' to the `run_abaqus()` function is therefore not required. It involves using SHARP.cells and Abaqus static with the `NLGEOM` flag OFF. It is also used as part of the vibration analysis, the linear coupled and the linear tapered analyses.

Linear coupled This involves coupling the above results to the beam code SHARP.beams for an actual beam simulation. The beam description might be nonlinear but the stiffness is linear and is not updated with deformed geometries.

Nonlinear coupled This is potentially the most useful type of analysis in an aeroelastic simulation. It involves using SHARP.beams and Abaqus (with the `NLGEOM` flag ON) repeatedly to update the cross sectional stiffness and mass properties of the beam being studied in SHARP.beams. Information travels both ways and SHARP.cells provides updated matrices when required by the beam solver and takes nodal positions and rotations to convert them into strains and curvatures and use those exact values as the reference loading for the nonlinear unit cell analysis.

Linear tapered When a tapered structure is under consideration, the stiffness varies along the span of the idealised beam. SHARP.cells is first run for a few representative unit cells at discrete positions on the beam representation which provide the required stiffness parameters for SHARP.beams. The beam is initialised using this if the number of beam elements is the same as the number of unit cells for which properties have been acquired or, alternatively, a linear interpolation between known stiffness values. The same would apply to inertial properties. After that SHARP.beams performs the beam study of interest as it would in the linear coupled case, that is, without further update on the cross sectional characteristics.

Vibration In order to obtain the normal mode frequencies and shapes of a slender structure, a vibration analysis is performed which involves SHARP.cells obtaining representative cross sectional properties through a linear Abaqus analysis and using SHARP.beams to assemble the global mass and stiffness matrices. As a final step, SHARP.cells performs an eigenvalue analysis with the aforementioned matrices using the linear algebra tools available in the `Numpy` package.

Buckling (linear perturbation) An estimate of the strength of a structure may be obtained via a local buckling analysis. In this particular one, SHARP.cells uses Abaqus' linear perturbation analysis to assess the response of the unit cell to a given loading. Only deformed shapes and buckling strains/curvatures are calculated here.

Post-buckling/fully nonlinear This is a full geometrically nonlinear analysis in which SHARP.cells uses Abaqus recursively and with the `NLGEOM` flag ON, to characterise the evolution of the stiffness matrix as the geometry changes. This change in geometry is introduced by varying *one* of the components of the strain, γ, or curvature, κ, vector in a discretised domain of interest; the tangent stiffness is calculated for small increments of all degrees of freedom around those values. As described in Section 2.3, this is especially useful to determine local post-buckling characteristics, hence the name chosen.

The second part, or post-processor, is in charge of accessing the Abaqus output database (`.odb` file), calculating the elastic strain energy for the whole model. Using Eq.(2.7), the stiffness matrix is then calculated for the unit cell. It prints this 6×6 matrix to an output text file together with the mass matrix (calculated during the geometry generation), centroidal location and moments of inertia. Optionally, it can also output the buckling characteristics of the unit cell under the chosen loading state.

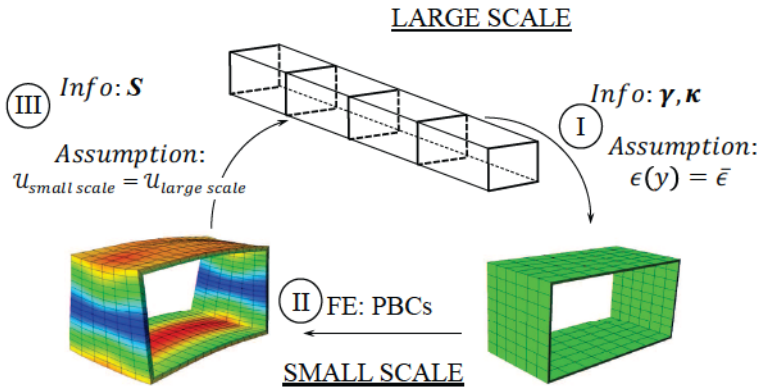

Figure 3.3.: Flow of information between the large and small scales.

3.1.5. Performance Analysis

The Python code written for this application is devised to be included in a conceptual-design-stage aeroelastic tool and, as such, it was designed to be fast and efficient. In order to benchmark SHARP.cells a representative unit cell has been created. Depicted in Fig. 3.4, this unit cell is a unit radius circular cylinder which includes eight composite plies $[0, +45, -45, 90]_2$. The wall thickness is 5% of the length of the radius. It is meshed using 2164 nodes and 1280 C3D8R elements. The computational time required for the SHARP.cells Python code plus the finite element package when calculating the fully populated 6×6 mass and stiffness matrices for this representative unit cell has been explored in Table 3.1. We recall that 21 loading cases are required to determine all the terms in the stiffness matrix. The total running time is around five seconds with an Intel Core i7 2600k@4.5GHz as opposed to a couple of minutes if the whole 3D structure (extruded to 50 times the length of the unit cell) is run in Abaqus. Most of the time is consumed by the finite element solver stage. The influence that different computer hardware has on the analysis time is also reflected on Table 3.1. Evidently, the number of available logical cores plays an important role in the finite element stage. The benefits of using a larger number of cores are more pronounced in fairly large finite element models and it is not evident here; we can observe diminishing returns after four cores are employed and communication becomes more relevant than available cores. In general, we can state

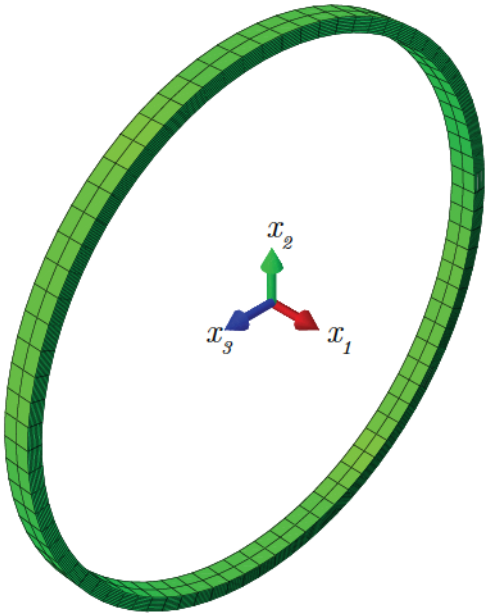

Figure 3.4.: 3D view of the 8-ply cylinder used to benchmark SHARP.beams. Two rows of elements are not necessary but the second one is kept to check spanwise invariance.

Table 3.1.: Representative running times of SHARP.cells with different hardware configurations. The Python column includes the pre- and post-processor CPU time and the Abaqus column indicates the FE analysis CPU time.

Storage type	# of cores	Python [s]	Abaqus [s]	Total wall clock time [s]
HDD	1	0.913	3.82	4.73
HDD	2	0.916	2.86	3.78
HDD	4	0.912	2.47	3.38
HDD	8	0.912	2.52	3.43
SDD	8	0.644	1.88	2.52

that two fast x86 processing cores are enough to run SHARP.beams adequately. The Python code is single-threaded and does not benefit from multiple cores. I/O speed from the storage drive was explored by testing SHARP.cells in a high-performing solid state drive as opposed to a mechanical 7200RPM hard disk. Improvements are present but may not justify the cost of the former and its reduced storage size.

3.2. Integration with 1-D Beam Solver

The geometrically nonlinear beam solver, SHARP.beams, developed by Hesse and Palacios [47] (based on a *geometrically-exact* displacement-based formulation

[40, 99]) and wrapped with Python by Simpson and Palacios [102] is coupled to this homogenisation code for certain analysis types as described in Subsection 3.1.4. Thanks to both programs being written in the same language, the transfer of information is straight forward. Also, certain functions and classes from SHARP.cells can be imported and used in SHARP.beams and vice versa.

In a general geometrically nonlinear case, SHARP.cells calculates the mass and stiffness matrices for each beam element, following the procedure described in the previous section, and then transfers them as an input for the initialisation of the nonlinear beam solver. Aside from a tapered structure, each beam element is given the same properties at the start of the simulation. At each time step, the nonlinear beam solver in the aeroelastic framework (see Figure 3.5) uses the forces computed from the unsteady aerodynamics solver on the previous step's deformed shape to update the geometry. The number of time steps required for requesting an updated stiffness matrix from SHARP.cells depends on the tolerances set for changes in the strain state. Once that condition is met, the instantaneous beam strains and curvatures of the current deformed shape are computed. These are determined at a discrete and small number, N_s, of span-wise locations using Eq.(2.24). The instantaneous beam strains and curvatures are then used as an exact input for a N_s number of unit cells. For each of these unit cells, a 21-loading-case, geometrically-nonlinear, static analysis is performed to obtain the updated stiffness that corresponds to that specific deformed geometry. Alternatively, these geometrically-nonlinear, static analyses can be employed to assess the integrity of the structure. One possibility is to compare the resulting stresses and strains with predetermined maximum allowed stresses and/or strains for a given material. Please note that, in the current approach, materials are always treated following a linear-elastic law, with no plasticity. A second possibility is to limit the amount, if any, of local buckling, at the unit cell level, and use that as a design constraint, on its own or in addition to the maximum stress approach. Other options could be considered as well.

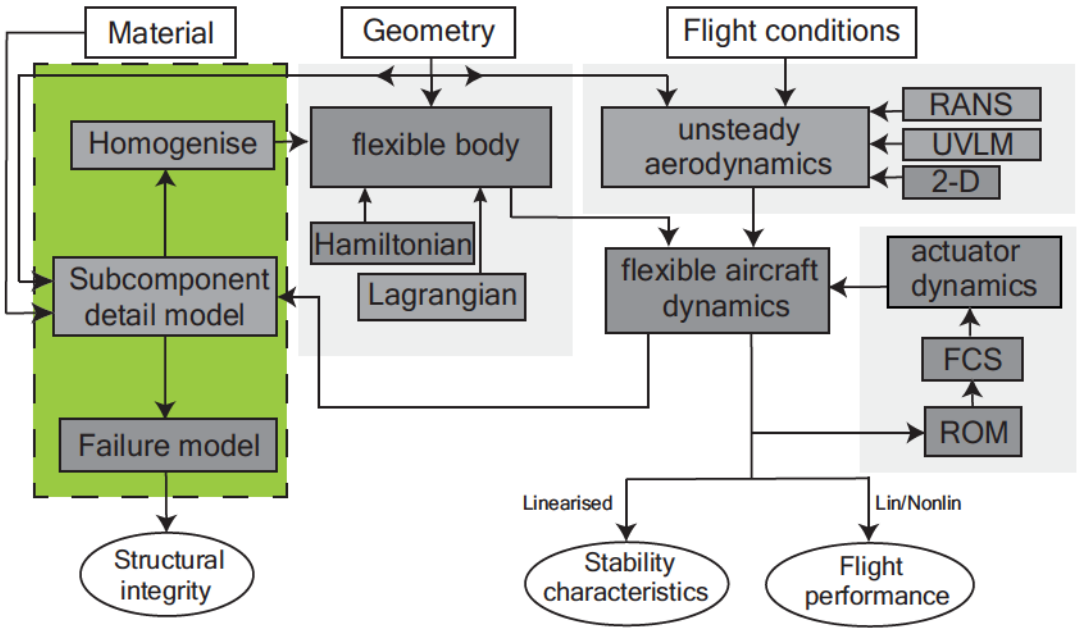

Figure 3.5.: Main analysis blocks in the multidisciplinary aeroelastic framework of SHARP. The modules in green are SHARP.cells.

Free vibration normal modes and frequencies can also be obtained by using the beam solver to assemble the global mass and stiffness matrices (using the cross sectional ones obtained from the homogenisation tool) and then using Numpy's linear algebra module (`numpy.linalg`) to compute the eigenvalue problem defined in Eq.(2.29).

It is worth noting that SHARP.cells is OS-independent and has been tested in both Windows and Linux. Thanks to the dynamic variables used for directories and the fact that all commands used to run Abaqus analyses are implemented using the OS module, porting the Python code from Windows to Linux requires no modifications at all.

Chapter 4

Homogenisation of Slender Composite Structures with Reinforcements

This chapter gives examples of the linear static part of the homogenisation methodology described in Chapter 2. Most of the implementation details explained in Chapter 3 will also be illustrated via the test cases included here. These will cover a wide variety of cross sections –ranging from a simple circular cylinder to a complex, active twist rotorblade[20]–, material configurations –isotropic, orthotropic and fully anisotropic– and geometry variations in the spanwise direction. Special implementation advantages of SHARP.cells, such as the ability to use tie constraints between differently meshed parts (see Subsection 4.1.1 or Section 4.3) or the ability to recover accurate 3D stresses (see Section 4.2), are highlighted. The test cases are: two varieties of prismatic box beams and a tapered box beam in Section 4.1, a circular cylinder with spanwise thickness variation in Section 4.2 and a real-life helicopter rotorblade in Section 4.3.

Whenever possible, the results obtained here will be compared with UM/VABS[82] and/or full 3D finite element results obtained from Abaqus.

4.1. Prismatic Box Beam

This section presents three different models of a prismatic box beam. The first one is an initial validation of the method, for isotropic materials and classical stiffness components (i.e. no shear components). It includes transverse reinforcements. The second one investigates the suitability of this approach for tapered slender structures by coupling SHARP.cells to SHARP.beams and using different levels of fidelity to populate the stiffness matrix of the 1-D beam solver. Finally, the third one explores the behaviour of different composite layups and it includes transverse shear terms.

4.1.1. Isotropic Prismatic Box Beam with Reinforcements

This first model is a ribbed prismatic box beam made out of homogeneous isotropic material (aluminium: $E = 70\text{GPa}$, $\nu = 0.3$) with width and height equal to 2m and 1m, respectively, and with 0.025m-thick walls. The distance between ribs is $b = 1\text{m}$, which defines the unit cells. In order to define a reference for comparison, a full box-beam of length $L = 20\text{m}$ is built-in on one end and all the loads or moments are applied via a reference point at the other end. This reference point is linked to the structure using a rigid body constraint which ties all the nodes on the end of the beam to said reference point. The full model is meshed using 10400 C3D8R elements with 17421 nodes and is partially shown in Figure 4.1 (a cut-out has been included for better visualization). The unit cell mesh has a twentieth of the number of elements. There are ten elements along the height, width and span of one cell, and three through the thickness. The transverse reinforcements in both models (full and unit cell) are added to the model via tie constraints, which avoids local mesh refinement in the joints between rib and outer skin. The geometry and the von Mises stress contour of the full structure subject to a tip bending curvature ($\kappa_2 = 0.1\text{m}^{-1}$) are shown in 4.1.

Stiffness results for the extensional (S_{11}), torsional(S_{44}) and both bending directions(S_{55}, S_{66}) are summarised in Table 4.1. The results from SHARP.cells

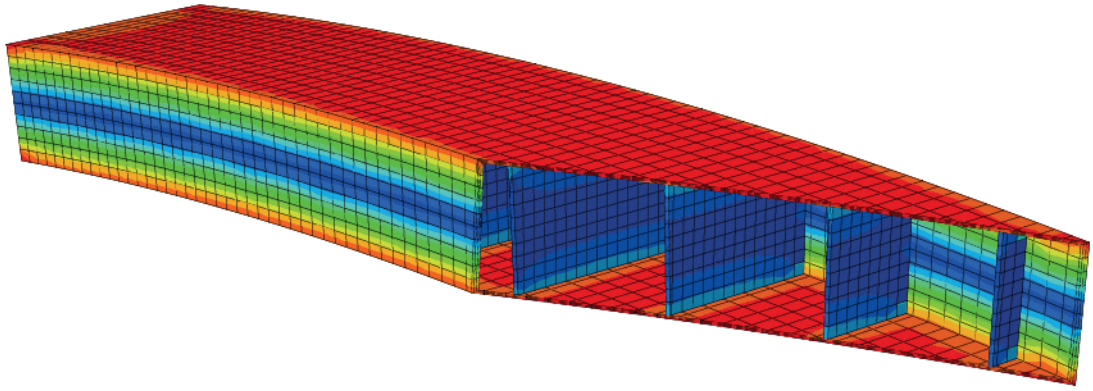

Figure 4.1.: Vertical cut-out of the deformed reinforced box-beam model under a bending curvature of $\kappa_2 = 0.1\text{m}^{-1}$). Contour plot shows von Mises stress.

for the unreinforced beam are compared to those from: a) analytical results from thin-walled beam theory; b) full 3D FEM analysis using static loading; c) UM/VABS. However, the results in italics show the effect of adding a transverse rib to all unit cells at their mid-span location. The thickness of the reinforcement is the same as that of the outer walls of the beam. The agreement of the results produced by this homogenisation method is excellent both with the theory and the current available tools. The small discrepancy that thin-wall theory has, in the case of torsion, with both UM/VABS [82] and the proposed method, is due to the thin-wall assumption of the former. Thin-walled closed sections have uninterrupted circuits for the shear flow and if the wall thickness is much smaller than the other cross-sectional dimensions, then this shear flow can be assumed to be uniform across the wall thickness [5]. The suppression of warping at the built-in ends, on the other hand, has negligible effects at the scale that the torsional rigidity is calculated. Finally, the addition of the transverse wall results in a small change of stiffness, which can nevertheless be estimated with the present approach.

Table 4.1.: Homogenised stiffness constants for the prismatic box beam. Numbers in italics correspond to the stiffness of the beam with transverse reinforcements present in the structure.

Stiffness constant ***(with ribs)***	FE (full beam)	Analytical (thin wall)	UM/VABS [82]	SHARP.cells
$S_{11}(EA)$ [GN]	10.3 *(10.5)*	10.3	10.3	10.3 *(10.5)*
$S_{44}(GJ)$ [GNm^2]	1.71 *(1.72)*	1.79	1.71	1.71 *(1.72)*
$S_{55}(EI_{22})$ [GNm^2]	1.91 *(1.94)*	1.91	1.91	1.91 *(1.94)*
$S_{66}(EI_{33})$ [GNm^2]	5.58 *(5.62)*	5.58	5.58	5.58 *(5.62)*

4.1.2. Tapered Isotropic Square Box Beam

Most aircraft use tapered wings to get as close as possible to the elliptical lift distribution along the length of the wing without actually having to build a complex shape like an ellipse. Additionally, tapered wings are lighter than the aerodynamically comparable straight ones and experience a less severe root bending moment because they can be shorter for equivalent performance in terms of lift [90] The current methodology does not include taper but we are interested in the accuracy of three different approximations. For this purpose, a modified problem is defined to investigate the effect of a draft or taper angle in a box beam whose response is approximated by:

Approximation 1. A piecewise discretisation of the beam.

Approximation 2. A linear interpolation based on stiffness values calculated at the tip and at the root of the beam.

Approximation 3. An average approach using only the middle span geometry for the calculation of the beam properties.

The metric used to assess this accuracy is the tip deflection under a vertical tip load.

The model considered is a 10m long, 1m wide at the root, square box beam with 0.025m-thick walls. It is a cantilever beam anchored at the root and with no internal ribs. The full beam is discretised with 12000 solid (C3D8R) elements which result in 10 along the cross sectional dimensions, 100 along the span and 3 through the

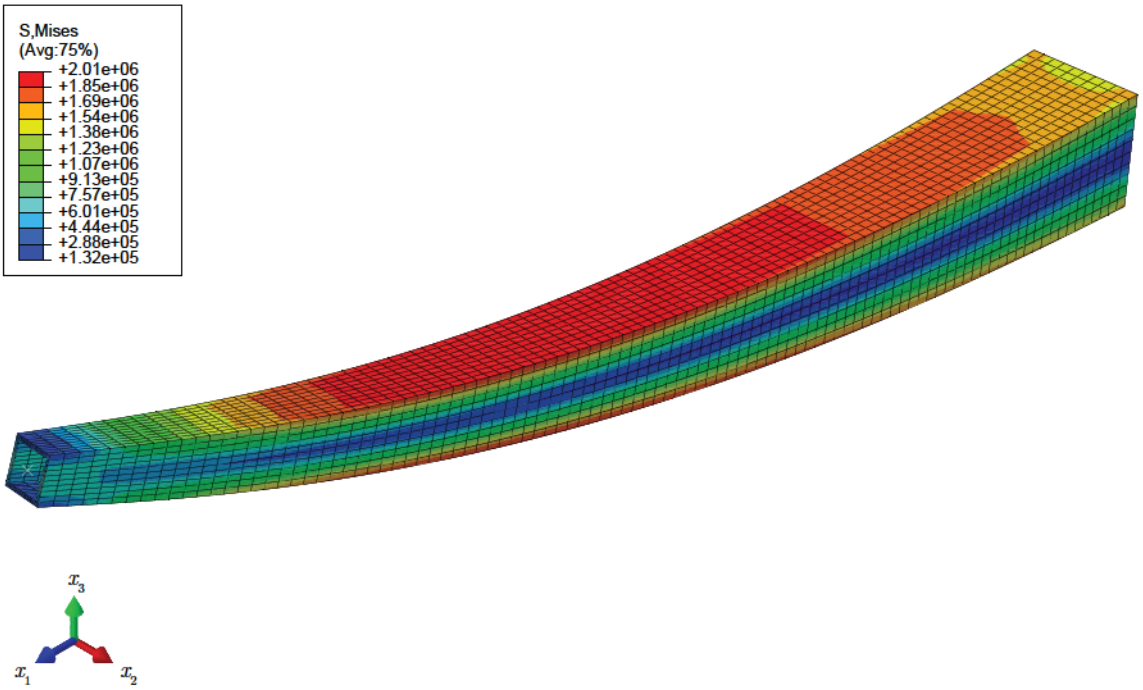

Figure 4.2.: von Mises stress distribution in a cantilever tapered box beam with a 5kN vertical tip load and a taper angle of 2 degrees.

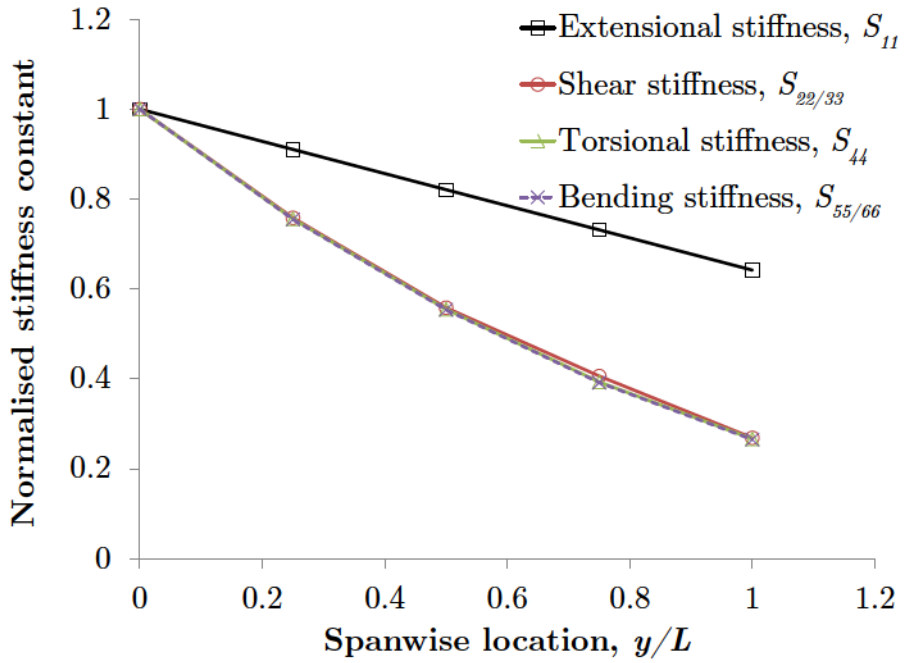

Figure 4.3.: Evolution of the stiffness parameters along the normalised span of a L=10m long, 52% taper ratio beam. The stiffness constants are normalised with the values at the root of the beam: $S_{11,root}$ = 683 GN; $S_{22/33,root}$ =31.6 MN; $S_{44,root}$ =63.1 GNm^2; $S_{55/66,root}$ =108 GNm^2.

thickness. Material properties remain unchanged from the previous example and the tip force, which is applied to the end section nodes via a reference point located at the centre of the section and rigidly link to them, is 5kN. For the first approach, the beam is represented using 10 representative unit cells. These are located at the 0.5m, 1.5m,...,9.5m positions along the main dimension of the beam and are only one element deep given that there is no variation in geometry in the spanwise direction for this case. For the second and third approaches, the beam cross sectional properties are obtained from a linear interpolation of actual values at the extremes (several FE solvers do that for beam elements [37]) and a constant distribution of the central properties respectively. Five taper angles are studied ranging from zero to 2 degrees which corresponds to 0% (no taper) to 70% taper ratio. The semi-width at any span position is given by the trigonometric relation $s(y) = 0.5 - y\tan(\alpha)$ where y is the spanwise position (measured from the root) and α is the taper angle. The taper ratio can then be calculated using the width at the tip. Fig. 4.2 shows the extreme case where the taper angle is 2 degrees and the tip section is only 302mm wide (70% taper ratio).

Table 4.2.: Tip vertical displacement under a 5kN tip load for an encastred tapered beam. The percentage difference with respect to the full 3D Abaqus solution is shown in italics.

Taper ratio [%] ***(% diff w.r.t. Abaqus Full 3-D)***	**Abaqus Full 3-D** [mm]	**1D beam Approx. 1** [mm]	**1D beam Approx. 2** [mm]	**1D beam Approx. 3** [mm]
0	1.582	1.593 *(0.65)*	1.593 *(0.65)*	1.593 *(0.65)*
17	1.821	1.852 *(1.68)*	1.742 *(-4.34)*	2.112 *(15.98)*
35	2.161	2.231 *(3.24)*	1.955 *(-9.53)*	2.869 *(32.72)*
52	2.690	2.824 *(4.99)*	2.255 *(-16.17)*	3.856 *(43.36)*
70	3.649	3.950 *(8.22)*	2.732 *(-25.19)*	5.947 *(62.95)*

Table 4.2 shows the tip deflections in mm for the three different approaches described above and the percentage discrepancy with the full 3D solution from Abaqus. As expected the best solution is achieved with the most accurate representation of the stiffness variation throughout the span. Having 10 unit cells yields just under 5% error for a taper ratio of 52% which is not very desirable.

The accuracy increases with a finer discretisation but then the advantages of this combination of tools versus a full 3D finite element analysis are hard to justify. The linear discretisation performs better than the average approach and it suggests that having a good estimate in the evolution of the stiffness is crucial for obtaining the tip displacement correctly. For that reason, the stiffness constants are plotted in Fig. 4.3 for the 52% taper ratio beam. It demonstrates that a linear interpolation is only valid for the extensional stiffness. For a tip load, shear and bending stiffness play the most important role and higher order polynomials, at least quadratic, should be employed in order to greatly improve the results, as suggested by Friedman and Kosmatka for Timoshenko beams [38].

4.1.3. Full 6×6 Stiffness Properties of Composite Prismatic Box Beams

The third model in this section is a thin-walled box-beam made of six composite plies of thickness t=0.127mm. Two different composite layups are considered: a)($[0,\text{-}30]_3$) for all walls and b)$[-15]_6$, $[15]_6$, $[15/-15]_3$, $[-15/15]_3$ for the top, bottom, right and left walls respectively. The width and height of the model are respectively: w=24.21mm and h=13.46mm. The material used is AS4/3501-6 graphite-epoxy unidirectional pre-preg, and it has the following properties: $E_{11} = 142$ GPa; $E_{22} = E_{33} = 9$ GPa; $\nu_{12} = \nu_{13} = 0.42$; $\nu_{23} = 0.34$; $G_{12} = G_{13} = 5.998$ GPa; $G_{23} = 4.799$ GPa; $\rho = 1265$ kg m^{-3}.

The unit cell model consists of 20 C3D8R elements per side and one per ply through the thickness. The full beam model is constructed with 20 unit cells. The geometry of the unit cell, along with the von Mises stress contour plot corresponding to a transverse shear loading of $\gamma_2 = 0.1$ for the $[0,\text{-}30]_3$ layup, is shown in Figure 4.4. Results from the present method are shown in tables 4.3 and 4.4. They agree very well with published results (UM/VABS, from Ref. [82]) and with the full 3-D solution. The coupling terms present in the unbalanced $[0,\text{-}30]_3$ layup are due to extensional-twist coupling and shear-bending coupling. If we normalise

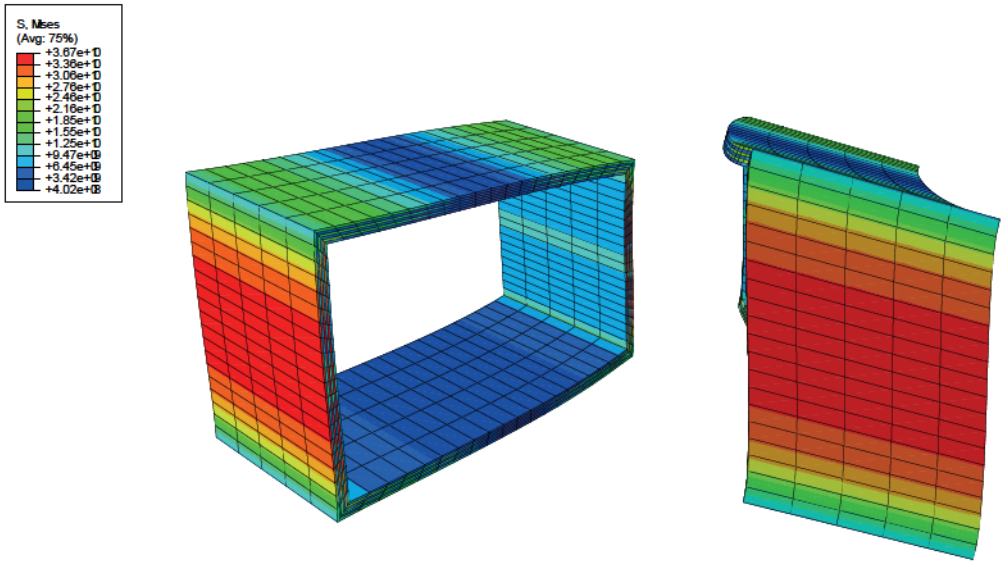

Figure 4.4.: von Mises stress contour plot for a loading strain of $\gamma_{22} = 0.1$.

Table 4.3.: Full stiffness matrix results for a rectangular prismatic composite beam. Layup is $[0,30]_3$

Stiffness constant ***(% diff w.r.t. Abaqus Full 3-D)***	**Abaqus Full 3-D**	**UM/VABS**	**Present method**
S_{11} [MN]	5.497	5.496 *(0.0)*	5.497 *(0.0)*
S_{22} [MN]	0.442	0.4375 *(-1.0)*	0.4377 *(-1.0)*
S_{33} [MN]	0.1843	0.1855 *(0.6)*	0.1858 *(0.8)*
S_{44} [Nm^2]	50.06	49.73 *(-0.6)*	49.89 *(0.4)*
S_{55} [Nm^2]	169.16	170.5 *(0.8)*	171.2 *(1.2)*
S_{66} [Nm^2]	434.1	430.4 *(-0.9)*	432.2 *(-0.4)*
S_{14} [kNm]	5.280	5.830 *(10.0)*	5.48 *(3.78)*
S_{25} [kNm]	-2.583	-2.947 *(14.0)*	-2.874 *(11.2)*
S_{36} [kNm]	-3.26	-3.121 *(-4.2)*	-3.185 *(-2.3)*

Table 4.4.: Full stiffness matrix results for a rectangular prismatic composite beam. Layup is (from top wall and clockwise): $[-15]_6, [15]_6, [15/-15]_3, [-15/15]_3$

Stiffness constant ***(% diff w.r.t. Abaqus Full 3-D)***	**Abaqus Full 3-D**	**UM/VABS**	**Present method**
S_{11} [MN]	6.162	6.161 *(0.0)*	6.162 *(0.0)*
S_{22} [MN]	0.412	0.410 *(-0.4)*	0.418 *(1.4)*
S_{33} [MN]	0.182	0.1806 *(-1.2)*	0.186 *(1.7)*
S_{44} [Nm^2]	49.2	48.58 *(-1.3)*	49.35 *(0.3)*
S_{55} [Nm^2]	168.9	169.5 *(0.3)*	169.4 *(0.3)*
S_{66} [Nm^2]	408.1	405.3 *(-0.7)*	406.5 *(-0.3)*
S_{12} [MN]	-0.796	-0.855 *(7.4)*	-0.788 *(-1.0)*
S_{45} [Nm^2]	53.12	50.51 *(4.9)*	52.15 *(-1.8)*

these coupling terms S_{14} and S_{25} by the corresponding direct terms as $\frac{S_{14}}{\sqrt{S_{11}S_{44}}}$ and $\frac{S_{25}}{\sqrt{S_{22}S_{55}}}$ respectively, we can explain why the up-to-10% discrepancy occurs: the coupling terms are exactly two orders of magnitude smaller than the corresponding direct terms. With the symmetric layup, we only encounter extensional-shear and extensional-bending couplings in the axis about which the wing profile is not symmetrical. It is worth noting that in order to calculate the shear stiffness using a full beam model, this has to be made remarkably long in order to avoid end effects (see the following sub-section) which results in very computationally expensive models that take hours rather than seconds in a desktop PC.

4.1.4. End Effects

Transverse shear is characterised by having end effects that propagate further than other types of loadings such as bending. This becomes a problem when obtaining shear stiffness properties from a full 3D model: knowing how far these propagate dictates the accuracy obtained via the current method which assumes very slender structures. This is given as an example in Figure 4.5 where the error in the compliance terms associated with bending and shear has been plotted. (Compliance is calculated in the full beam model because the loading is introduced in terms of forces and not strains). It can clearly be seen that in the bending case, most length of the beam produces results with a very low percentage error, whereas in

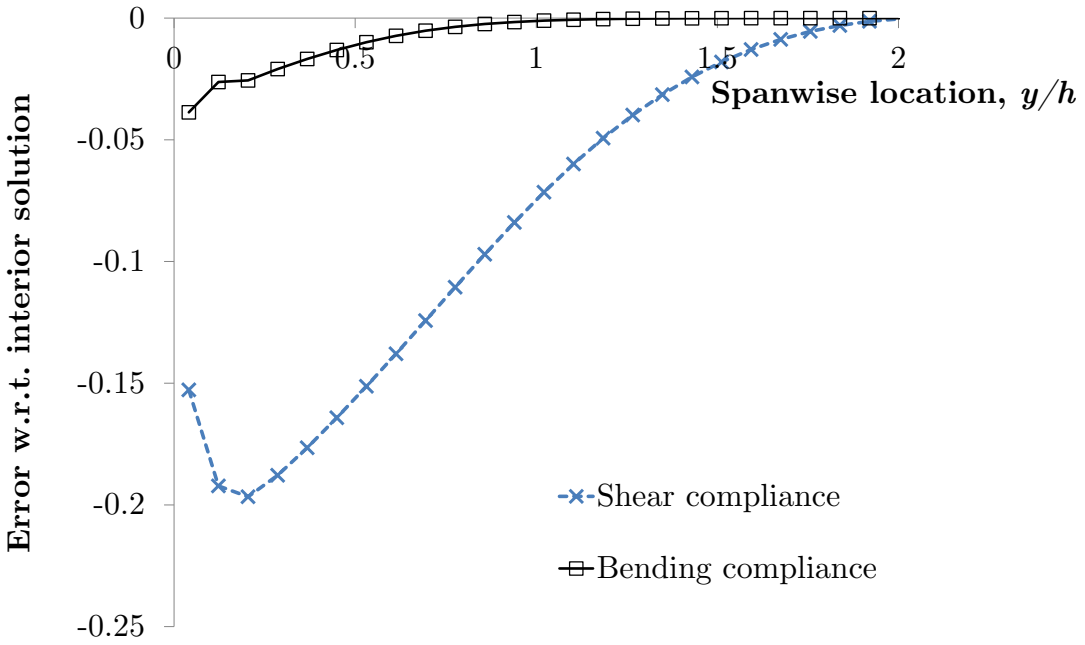

Figure 4.5.: Characteristic length of the propagation of end effects for the shear and bending compliance terms. The spanwise coordinate, y, is normalised with the cross sectional dimension, h.

the shear case, if the beam aspect ratio is smaller than 5, the majority of the length of the beam is affected by these end effects. The thickness of the wall also has an influence on how far these end effects propagate. Figure 4.6 shows that results calculated at a comparable distance from the root of the beam disagree more with the internal solution the thicker the walls are. Both bending stiffness and shear stiffness coefficients seem to be affected in a similar manner by the thickness of the wall as shown by the slope of the sensitivity plots in Figure 4.6.

4.2. Laminated Cylinder with Constant Ply Angle and Span-wise Variable Thickness

Next, we will consider two subcases: a 2-ply, constant-fibre-orientation-angle circular cylinder, which will be used to demonstrate the stiffness variation as the ply angle changes; and a modified section of this, that will be used to give an example

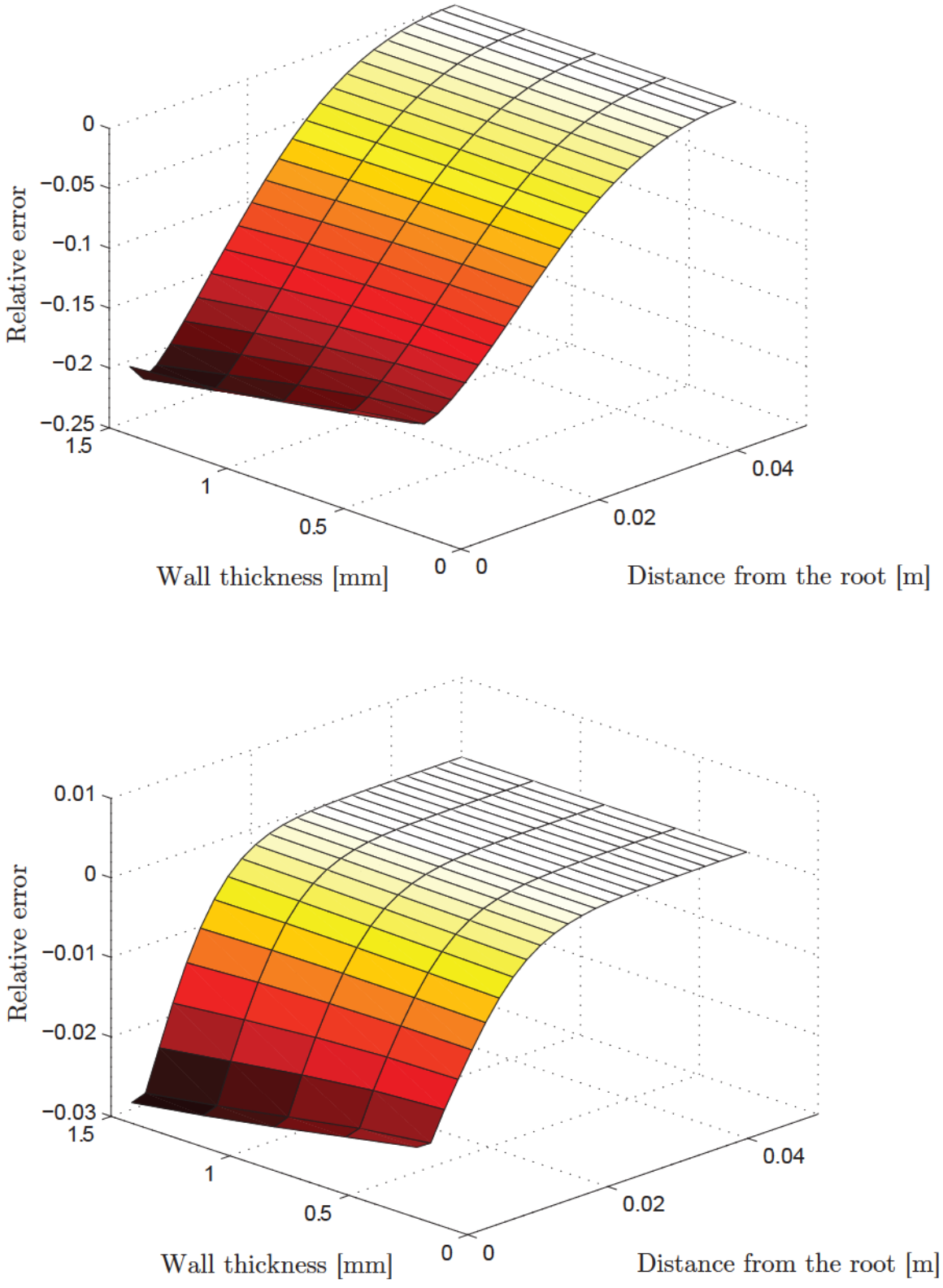

Figure 4.6.: Wall thickness effects on the propagation of end-effects for the shear (top) and bending (bottom) stiffness coefficients.

of the approach for cross sections of varying thickness along the span. The ply angle is measured clockwise around the radial direction of the tube, with the x_1 direction take as the reference for a zero-degree ply angle.

Table 4.5.: Ply properties of the laminated cylinder.

$E_{11} = 1.42 \times 10^{11}$ Pa	$E_{22} = E_{33} = 9.8 \times 10^{9}$ Pa
$G_{12} = G_{13} = 6.0 \times 10^{9}$ Pa	$G_{23} = 4.8 \times 10^{9}$ Pa
$\nu_{12} = \nu_{13} = 0.3$	$\nu_{23} = 0.3$

For the reference (constant-section) case, the cylinder has unit radius, $R = 1m$, measured to the outer wall, and 5% thickness ($t = 0.05m$), as depicted in Figure 4.7. The length of the unit-cell model, which does not affect the homogenised results, is $b = 0.1m$. This has been meshed with 320 C3D8R elements (724 nodes). There are two elements per 9 degrees in the circumferential direction, one per ply and two in the spanwise direction (only one is needed). The material properties of the composite used are given in Table 4.5. The non-zero terms of the 4×4 stiffness matrix have been plotted in 4.8 together with the results obtained using UM/VABS [82]. There are no transverse shear terms included because, in its current state, the methodology presented here cannot produce results for the transverse shear terms when the geometry is not constant along the length of the beam. The classical stiffness terms included are then: extensional (S_{11}), torsional (S_{44}) and bending ($S_{55/66}$) stiffnesses plus the coupling between the first two (S_{14}). Only one bending stiffness is shown in the figure, as the section is symmetric. As one should expect, S_{44} has a maximum around 30°, while S_{11} and $S_{55/66}$ decrease with θ. The evolution of these constants with the ply angle agrees very well between both methods and the error is always less than 0.1%.

A modified version of the previous example will be used next to explore the capabilities of the method to model 3D cells that include heterogeneity along the x_1 direction. For that purpose, the outer radius will remain the same, but the thickness of the section will vary as a function of the span-wise position, as shown in Figure

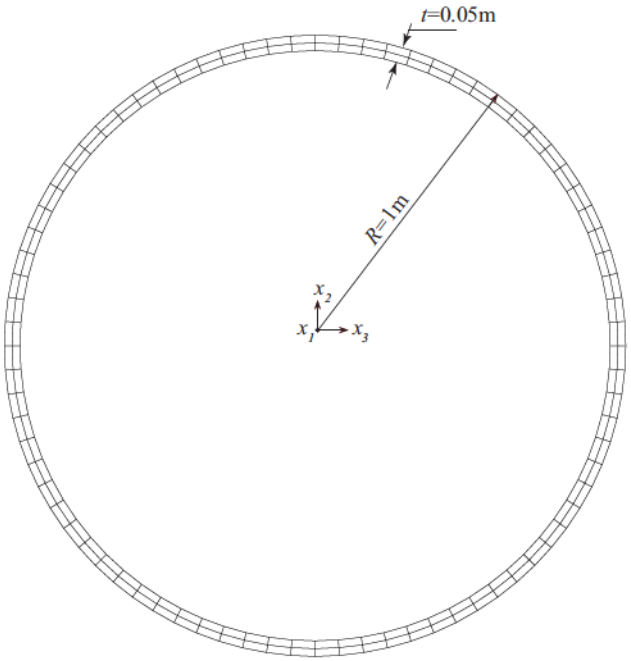

Figure 4.7.: Cross-sectional discretisation and dimensions of the reference laminated cylinder. (Cell model is 3-D.)

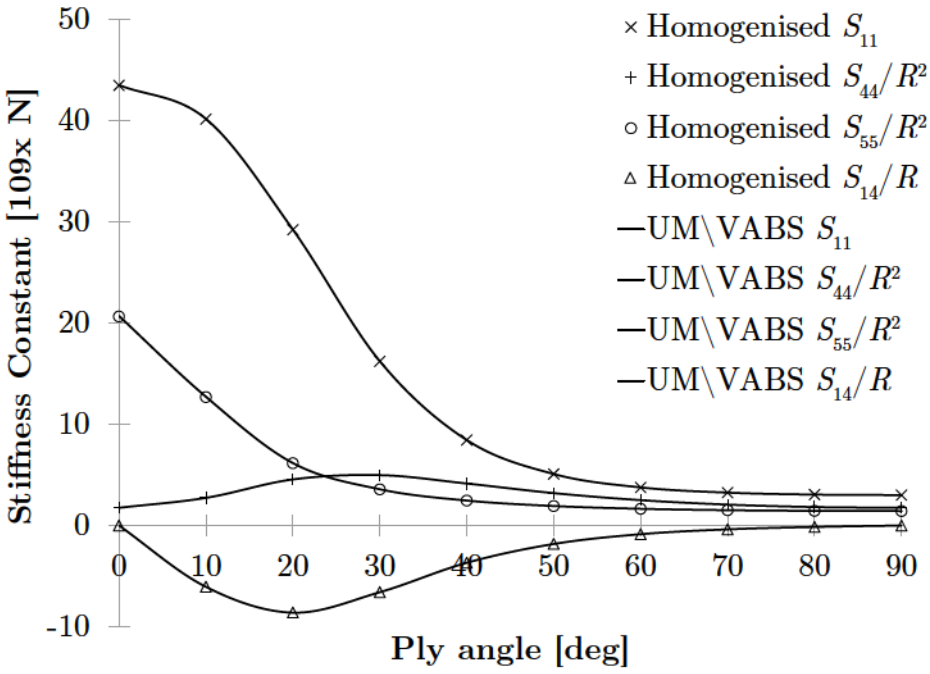

Figure 4.8.: Stiffness constants as a function of the ply angle for the laminated cylinder with constant wall thickness.

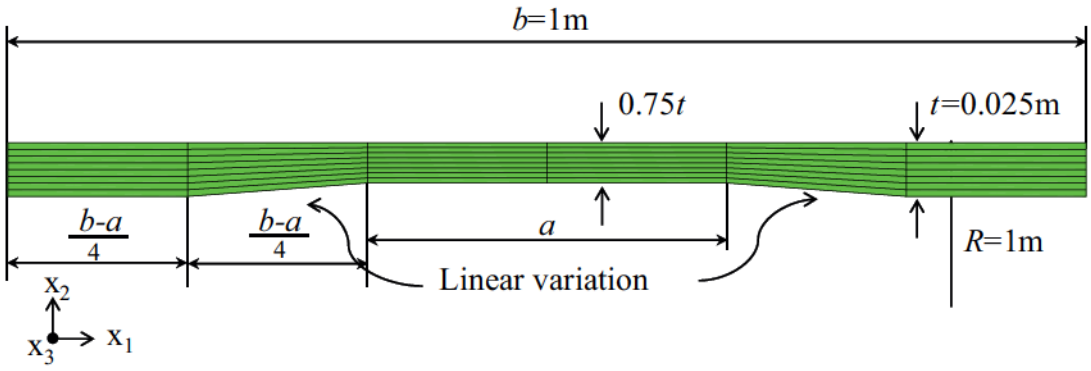

Figure 4.9.: Longitudinal cut of the cell of the laminated cylinder showing the thickness variation.

4.9. This change consists of a 25% reduction in thickness of the inner sections (length a) with a linear variation region joining the outermost sections which remain the same thickness. Please note that this is only an academic example as composite plies cannot be made thinner. The material properties are those from Table 4.5. The composite layup is now a $[45,\text{-}45,0,90]_s$. The new mesh has 6 elements in the spanwise direction, one per ply (8 plies) and 50 in the azimuth coordinate. The unit-cell results will be compared to a full size linear FE analysis of a 10-cell beam created with a tessellation of the cell just described, which results in a rather large mesh with 24000 C3D8R elements. It is clamped on one end and loaded with a $\kappa_3 = 0.1m^{-1}$ bending curvature. This is achieved by applying a rotation to a reference node placed at the other end and linked via a rigid body to the nodes at that extremity of the structure. It is worth noting that the unit cell model runs in seconds but the full-size model requires *over 16GB of RAM* and takes two orders of magnitude longer to run. Table 4.10 shows the deflection of the top nodes ($x_2 = R, x_3 = 0$) as a function of x_1 in the full model as compared to the deflection of a beam of the homogenised stiffness under the same load. Both solutions are very close with minor discrepancies at the boundaries of the beam, since end effects are not accounted for in the homogenised model. Table 4.6 contains the von Mises stress values through the thickness of all

Table 4.6.: Interpolated von Mises stress values accross plies at mid-span nodes on vaying thickness cylinder $\left[\frac{a}{b} = \frac{1}{3} \text{ and } \kappa_3 = 0.1\text{m}^{-1}\right]$.

Ply angle (deg)	von Mises stress (MPa)	
	Homogenised	FE (full beam, centre cell)
45	400.0	400.5
-45	386.0	386.5
0	910.1	910.3
90	211.2	210.9
90	209.1	208.8
0	780.2	780.9
-45	283.7	278.9
45	233.4	239.0

plies at an azimuth location of $45°(x_2 = x_3 = \sqrt{2}/2m)$ and at the mid-span location $(x_1 = b/2)$. It confirms that the technique not only predicts homogenised stiffness and displacements correctly, but it also provides small scale stress levels across the plies of the periodic structure.

Given the level of automation of the mesh generation it is easy to perform a parametric analysis to check the sensitivity of the structure to variations of one (or more) of its variables. In this case, the effect of the thickness of the wall has been studied. This is done by increasing the relative length of the thin region (25%-reduced thickness part) with respect to the total length, b. The results are plotted in Figure 4.11. Note that in the limit when $a/b = 1$ this corresponds to a cylinder of constant thickness $0.75t$. The evolution of the stiffness constants follows an expected mild decrease as the thickness is reduced.

4.3. Application to a Real Structure: ATR Blade

The Active Twist Rotor blade (ATR) was jointly developed at NASA and MIT, and has served as a benchmark for several homogenisation techniques because of its high geometrical complexity of the cross section and the fact that it combines different anisotropic materials [97]. Its dimensions and material distribution can be seen in Figure 4.12 and the elastic properties of the conforming materials are

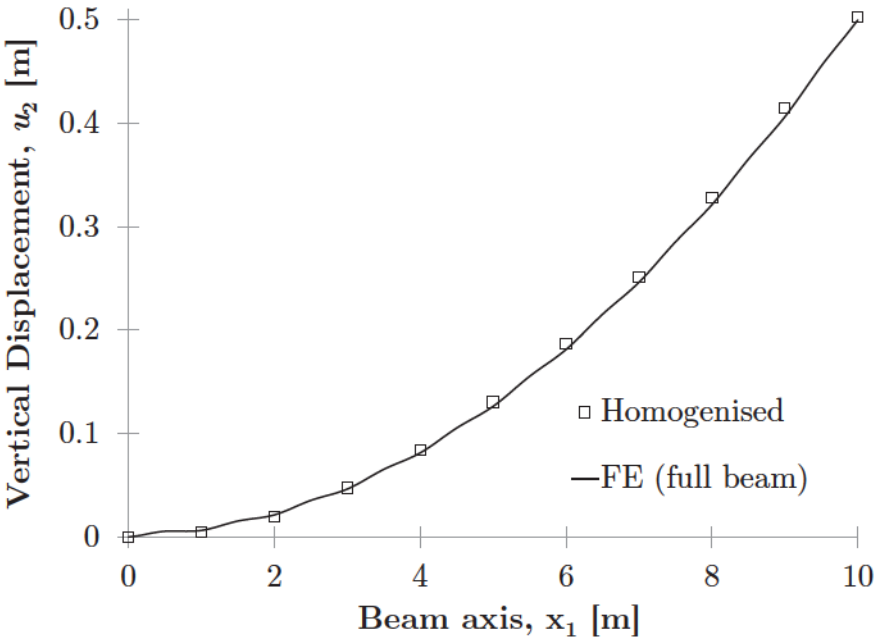

Figure 4.10.: Vertical deflection of the top nodes of the varying-thickness cylinder $\left[\frac{a}{b} = \frac{1}{3} \text{ and } \kappa_3 = 0.1\text{m}^{-1}\right]$.

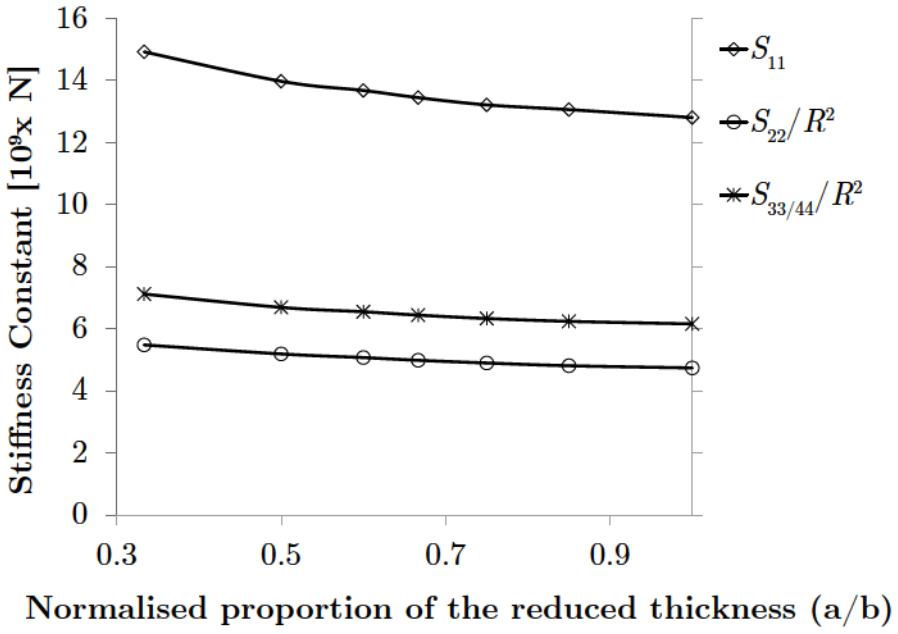

Figure 4.11.: Effect of local thickness reduction on the stiffness of the laminated cylinder.

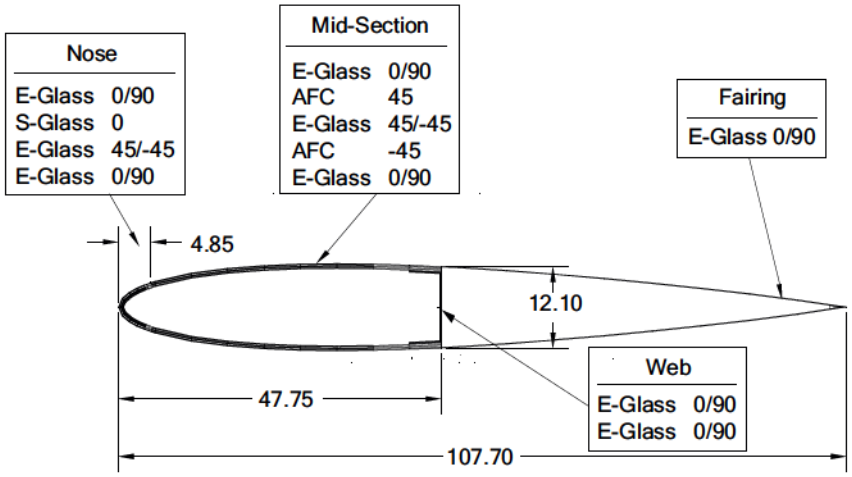

Figure 4.12.: Dimensions (in mm) and materials used in the different parts of the ATR wing.

included in Table 4.7. The cross section has been modelled without the foam core, and extruded to create a unit cell with a total depth of 20% the chord of the profile. Note, however, that the results are independent of the choice of depth for the unit cell. Given the fact that the current methodology allows for advanced modelling features of the FEM package to be used in the solution, the various parts of the section (skin, spars, joints, etc.) were meshed independently, without the need for coincident meshes on the interface, and were assembled using Abaqus tie constraints [103] (penalty method) for a mesh transitioning between pairs of surfaces. As already mentioned, this enhances the scalability and possibilities of the current solution method, as the details in the connection between spar and skin have a small effect in the homogenised stiffness. The mesh used consists of 3912 C3D8 elements and 6171 nodes which is a very similar discretisation to that in [82]. Full integration was used here to mitigate a problem of artificial strain energy creation.

Table 4.7.: Material properties of the plies in the ATR wing [20].

Material Property	**Units**	**E-Glass (Style 120 Fabric)**	**S-Glass (Unitape)**	**Active-Fibre Composite**
E_1	[GPa]	20.7	46.9	22.18
E_2/E_3	[GPa]	20.7	12.1	14.91
G	[GPa]	4.1	3.6	5.13
ν	-	0.13	0.28	0.454
t_{ply}	[mm]	0.114	0.229	0.203

Table 4.8.: Stiffness matrix including transverse shear of the ATR blade

Stiffness constant ***(% diff w.r.t. Abaqus Full 3-D)***	**Abaqus Full 3-D**	**UM/VABS**	**Present method**
S_{11} [kN]	1681	1677 *(-0.3)*	1678 *(0.2)*
S_{22} [kN]	209.2	208.4 *(-0.4)*	205.1 *(1.9)*
S_{33} [kN]	24.6	24.50 *(-0.8)*	24.2 *(1.6)*
S_{44} [Nm^2]	39.1	38.11 *(-2.5)*	38.59 *(1.3)*
S_{55} [Nm^2]	41.17	41.18 *(0.0)*	41.08 *(0.2)*
S_{66} [Nm^2]	1092	1086 *(-0.5)*	1077 *(1.3)*
S_{16} [Nm]	395	369.4 *(6.4)*	384 *(2.7)*
S_{34} [Nm]	-243.2	-285.2 *(17)*	-253.1 *(4.1)*

The stiffness constants obtained through this method have been summarised in Table 4.8 and compared to those in UM/VABS [82] and the full 3D finite element solution. The direct terms are in full agreement with the UM/VABS model, and the coupling terms are very accurate. The observed discrepancy in the torsional stiffness, S_{44}, is due to a ply angle orientation error already identified in Palacios and Cesnik [82] that wrongly modelled the nose of the profile. There is also an element missing in the same area. There are two significant coupling terms in this model: S_{16} and S_{34}. Following the same procedure of Subsection 4.1.3, we can determine that the coupling terms are, once more, two order of magnitude smaller than the direct terms. Consequently, bigger discrepancies were observed. These coupling terms link extensional to bending and shear (about the non symmetrical axis) to torsional degrees of freedom, respectively. The former is due to material anisotropy and the latter arises from the non-symmetric geometry of the model (i.e. it is still present in an isotropic model). Aside from the coupling terms, the biggest discrepancy is found in the S_{22} term which corresponds to the vertical shear direction along which the blade is really stiff anyway. Increasing the number of elements by two reduces the error to under 1% hence this is believed to be a convergence issue. As it can be seen, the tie constraints introduced to link the various parts in the model have a negligible effect on the solution.

Chapter 5

Non-linear, Buckling and Vibration Analyses

This chapter encompasses all the advanced capabilities, in terms of analysis type, of the methodology proposed in this dissertation. After exploring the linear static solutions in Chapter 4, local buckling, nonlinear and vibration analyses are presented next. We begin the chapter with two different cases of local buckling for a prismatic ribbed structure: skin wrinkling under a torsional load and panel (skin) buckling between reinforcements for a compressive load. For the same situations, nonlinear analyses are performed to assess the evolution of the stiffness with said loading conditions and to explore the interesting phenomenon of localisation. All this is included in Section 5.1. The last part of the chapter is dedicated to the coupling of SHARP.cells with SHARP.beams for the calculation of the normal modes of a composite structure with and without shear effects (Section 5.2).

5.1. Buckling and Geometrically-nonlinear Analyses

5.1.1. Skin Wrinkling under a Torsional Load for a Ribbed Beam

Skin wrinkling between ribs under a torsional load is a sizing factor for aircraft wings [106]. In this numerical example, a 2×1m box beam made out of isotropic

material (E=70GPa, $\nu = 0.3$) is considered. The skin thickness is t_{skin}=2cm and ribs of t_{rib}=10cm are placed every metre. The unit cell is discretised using 20 C3D8R elements along the cross sectional dimensions, x_2 and x_3, two through the thickness and 20 again for the depth, $b = 1m$, of the unit cell. The full 3D structure is created using 8 of these unit cells. A linear perturbation buckling analysis is run on both models and the buckling load computed. Results for the unit cell and the full 3-D structure are in very good agreement: $\kappa_{1,unitcell} = 0.1207$ and $\kappa_{1,fullbeam} = 0.1203$. The buckling modes can be observed in Figure 5.1.

The analysis of local buckling using a unit cell requires that the wavelength of the response be the same length as the unit cell depth. In this skin wrinkling case, it is interesting then to investigate the effect of rib thickness to determine whether the period of the deformation is ever longer than the distance between two ribs. In Figure 5.2 it can be appreciated that even with a rib thickness of t=0.5mm the period is still the length between ribs. Further decrease in the thickness of the rib results in these ribs actually buckling, before it can be observed full-beam wrinkling period independent of the reinforcements.

The skin thickness also affects the stiffness as a function of loading. A geometrically-nonlinear analysis can be performed and the evolution of the stiffness compared between the present method and the full 3-D model. Figure 5.3 shows the secant stiffness S_{44} for a varying range of skin thicknesses from the full Abaqus beam and the unit cell approach. As one should expect, the thicker the skin the higher stiffness constant. This is captured with excellent agreement by both the unit cell and the full 3D structure. The initial plateau corresponds to the pre-buckling stiffness (mostly linear in this case). For all skin thicknesses tested, the stiffness decays gradually after the buckling curvature $\kappa_1 \approx 0.12$, as expected.

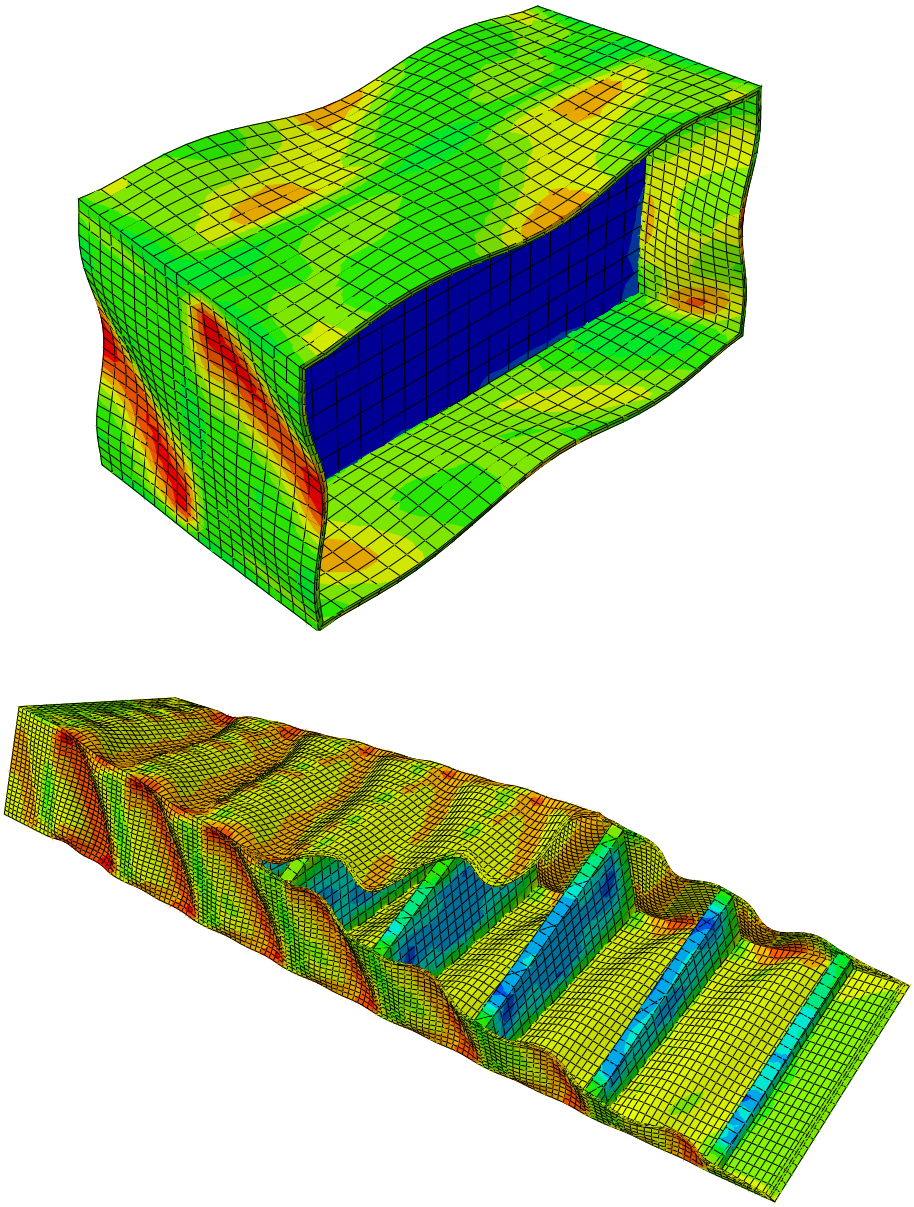

Figure 5.1.: Deformed shape of the unit cell (top) and full 3-D structure (bottom, with oblique side-cut) for a torsional load of $\kappa_1 = 0.1203$ and a rib thickness of 5mm. Unity deformation scale factor.

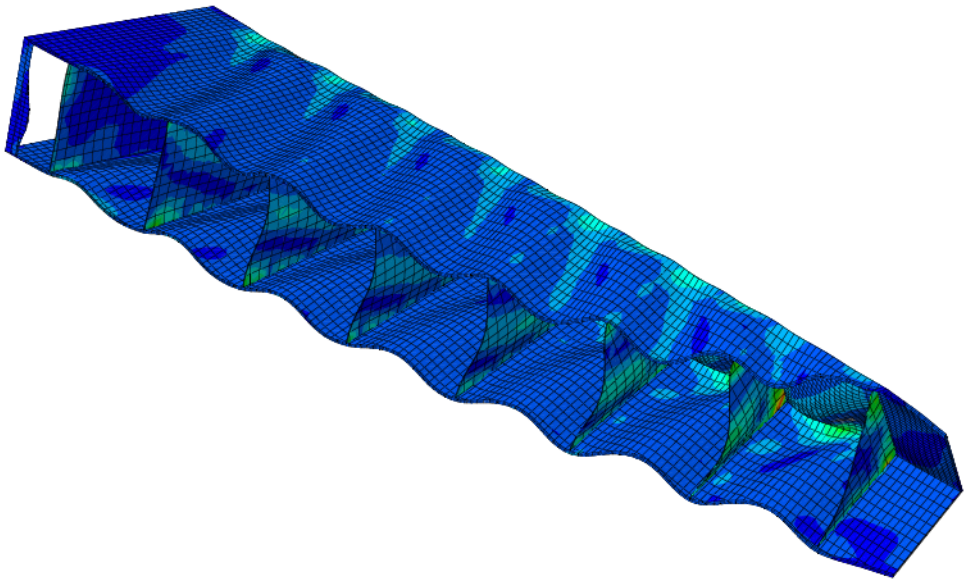

Figure 5.2.: Longitudinal cut on the deformed shape of the ribbed prismatic beam under a high torsional load of $\kappa_1 = 0.1203$ for a rib thickness of 0.5 mm. Unity deformation scale factor.

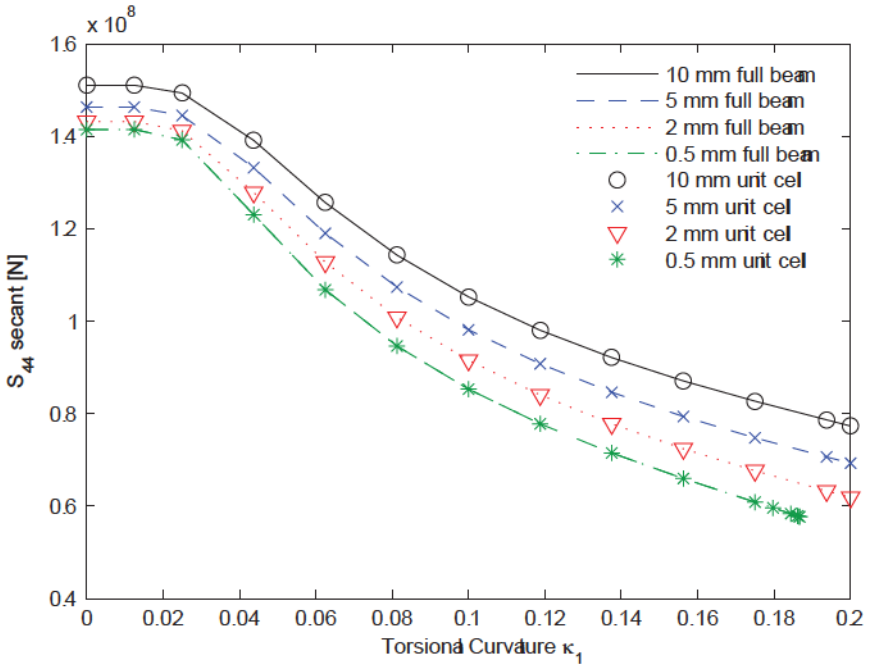

Figure 5.3.: Evolution of the torsional stiffness as a function of the torsional strain for different skin thicknesses.

5.1.2. Local Compressive Buckling of a Reinforced Prismatic Box Beam

This case explores the suitability of a unit cell analysis to obtain local buckling loads under compressive forces when the solution is still periodic. Global buckling is not accounted for here but could instead be computed by the homogenised beam model. The model used is similar, in shape, to those from Section 4.1, a prismatic box beam with perpendicular wall reinforcements, but the thicknesses of the skin and the reinforcement have been modified to ensure skin-buckling response. The new thicknesses are hence: 1mm for the skin and 10cm for the transverse reinforcement. The material used is the same aluminium as in the aforementioned case and the boundary conditions for the full beam are also the same. From a convergence test, the full beam mesh is created with 24000 C3D8R elements, while the model of the unit cell one is a sixth of that, that is, 4000 elements. The transverse reinforcements are linked to the skin of the structure via tie constraints. All elements have a planar characteristic length of 10cm; there are three elements through the thickness in the skin and two elements through the thickness of the reinforcement walls. As it can be seen from Figure 5.4, the buckling mode of the structure is coincident in both models -the unit cell one and the full 3D one. The maximum displacement is in both cases normalised to one, and the magnitude of the axial strain at which local buckling occurs (eigenvalue) is found to be very close: $\gamma_{1,buckling} = 3.042 \cdot 10^{-3}$ for the full 3D model and $\gamma_{1,buckling} = 3.058 \cdot 10^{-3}$ for the unit cell one. It is clear that both approaches find the same solution for the first buckling mode.

A geometrically-nonlinear analysis is then performed on the same model (with C3D8, full-integration elements now) to compute its post-buckling stiffness. Please note that this approach is only valid on the assumption that all cells deform the same and hence the periodicity of the structure is not broken. Figure 5.5 shows the vertical displacement at the centre top node of the horizontal top wall, as a function of the axial strain. Note that the vertical displacement shown in Figure 5.5 is measured relative to a baseline deformed geometry considered right after the initial

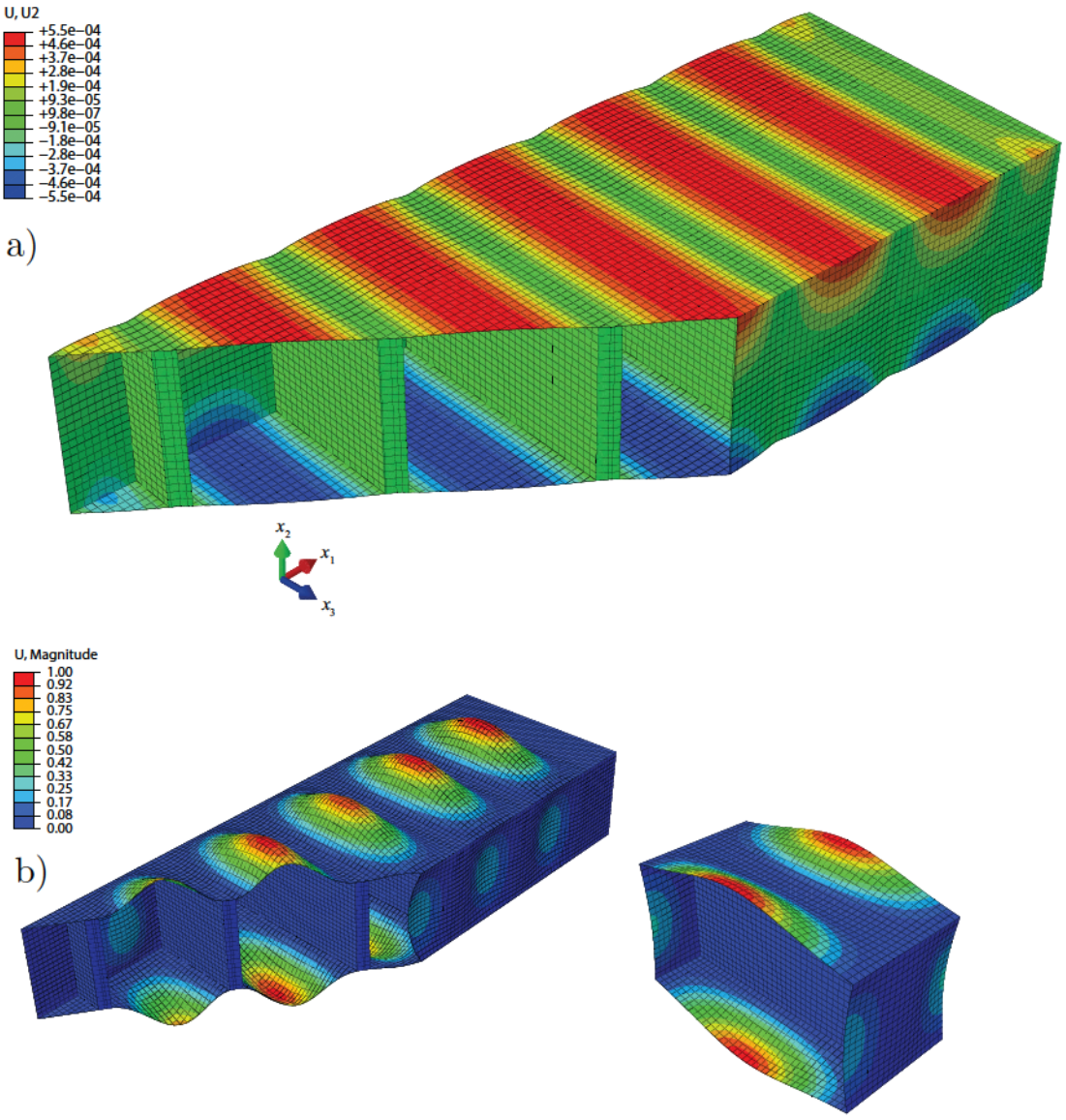

Figure 5.4.: (a)Vertical displacement in a *linear* ribbed prismatic beam subject to a compressive load of $\gamma_1 = 0.5\gamma_{1,buckling}$;(b) Contour plot of the first eigenshape of a ribbed prismatic beam under compressive loads. Full 3-D model (with a cut-out) shown on the left and unit cell on the right.

perturbation load (if there is any) is applied. Results are normalised with $\gamma_{1,buckling}$ of the unit cell. The deflection at that node starts to grow shortly after the normalised strain is unity, in agreement with the linear buckling analysis. The plot depicts three different load paths: one for the original structure and two corresponding to configurations with point normal loads of 500N and 1000N (positive inwards). The point forces are applied at the node where the displacement is measured, and in an antisymmetric manner; that is, the reciprocal node in the lower wall has the same load magnitude but opposite sign. The buckling of the original structure occurs with the horizontal walls buckling outwards and the side walls inwards (see Figure 5.4(b))naturally, that is, without the need of a perturbation load. The deformation before buckling, shown in Figure 5.4(a) for a linear analysis with $\gamma_1 = 0.5 \cdot \gamma_{1,buckling}$, leads to a non-uniform displacement field which triggers the bifurcation shown in Figure 5.5. For large enough perturbation loads (1000N in the example) vertical displacements in the opposite direction are obtained but the bifurcation load remains unchanged.

Geometrically-nonlinear Analysis of Periodic Compressive Buckling

The same energy-based procedure used in the linear cases in Chapter 4 can be applied to each increment in the nonlinear step in order to calculate the stiffness constants as a function of a given loading or strain. In Figure 5.6, the axial (secant) stiffness, $S_{11,secant}$, has been computed for axial deformations of up to 10% strain and three different wall thicknesses. This stiffness is calculated applying the same procedure described at the end of Section 2.2 to each of the increments in the nonlinear analysis in absolute terms. As the thick transverse reinforcements act as essentially rigid supports, the buckling strain is almost independent of the wall thickness. The nominal-thickness unit cell has also been compared with a full 3-D model, created with seven cells. As in previous cases, the boundary conditions on the full 3D model are: encastre on one side and rigid body plus reference point (to apply the loading displacement and measure the reaction force) on the other. The

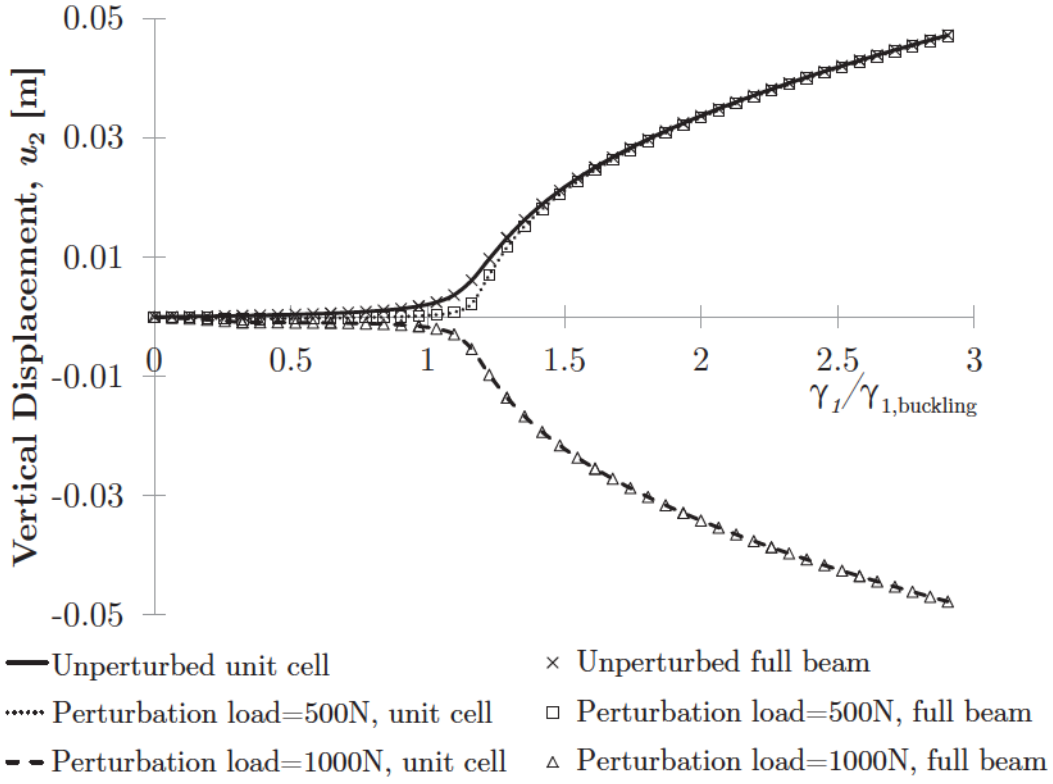

Figure 5.5.: Nonlinear load path as a function of the axial strain, γ_1, for the unit cell model and the full beam one.

results agree well but, as expected, the full model is slightly stiffer than the unit cell. This can be attributed to the way that the loading is introduced in the full 3D structure via rigid bodies with reference points and the fact that the stiffness is calculated using an average strain determined by the axial displacement of the loading reference point.

In addition, it can be observed that a negative tangent stiffness (slope of the load strain curves in Figure 5.7 is obtained at high strains, which implies that *localisation* has occurred [85]. Consequently, past this point (γ_1 greater than $\sim$ 0.1), the assumption of periodicity is broken and the cell-based solution diverges from the actual response. In this particular example, with very thick transverse reinforcements, the unit cell model still gives a reasonable approximation, but this will not be the case if warping information is propagated across several unit cells.

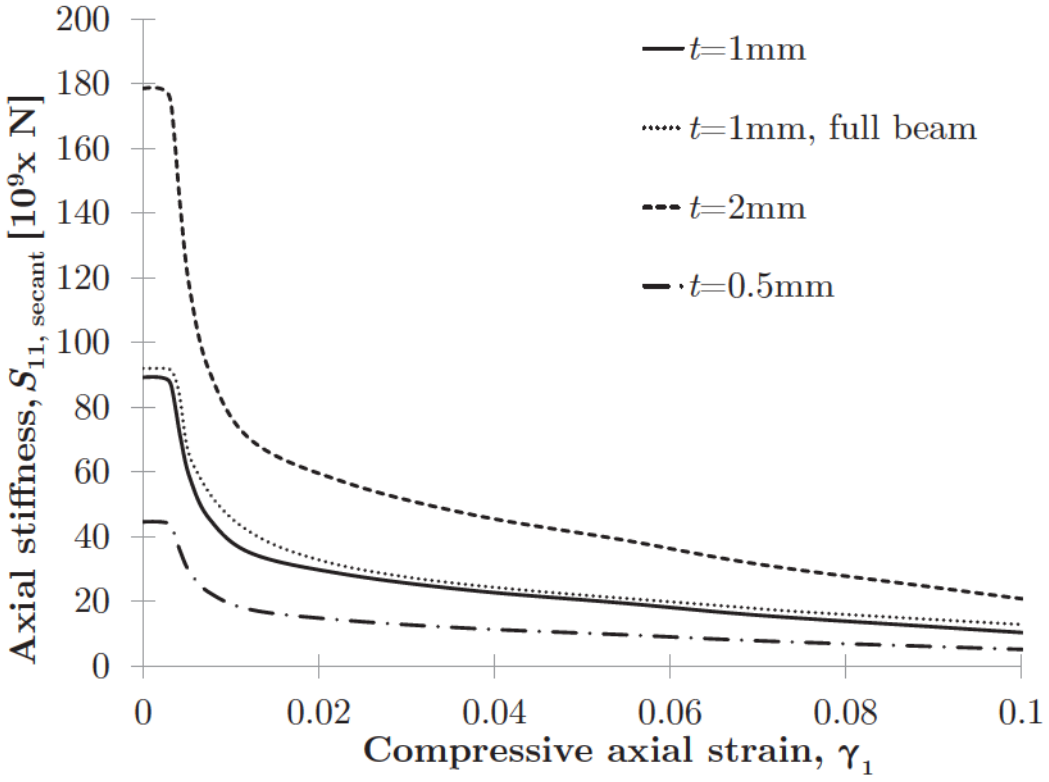

Figure 5.6.: Post-buckling axial softening of the reinforced prismatic beam for various wall thicknesses.

Continuing with the analysis of this example, when the tangent stiffness becomes zero, the beam response is no longer periodic and one of its cells will greatly deform, without increasing the load, while the others relax and go back to a lesser strain. In Figure 5.7, the reaction force and the axial component of the tangent stiffness have been plotted versus the axial strain in order to better understand the sequence of events in this localisation process. The strain for the adjacent beam cells has been computed using the displacement of the reference point at one end of the beam, subtracting the displacement due to the centre cell, and averaging it over all adjacent beam cells. Before localisation, the strain in all unit cells (depicted in Figure 5.8a for the unit cell and 5.8b for the full beam at $\gamma_1 = 0.05$) is the same. The load is always constant through the cells. When the tangent stiffness becomes negative ($\gamma_1 \cong 0.1$), one of the cells will continue to deform (growing γ_1, see Figure 5.8c) for a representation of $\gamma_1 = 0.35$) and the others will relax (decreasing γ_1, see

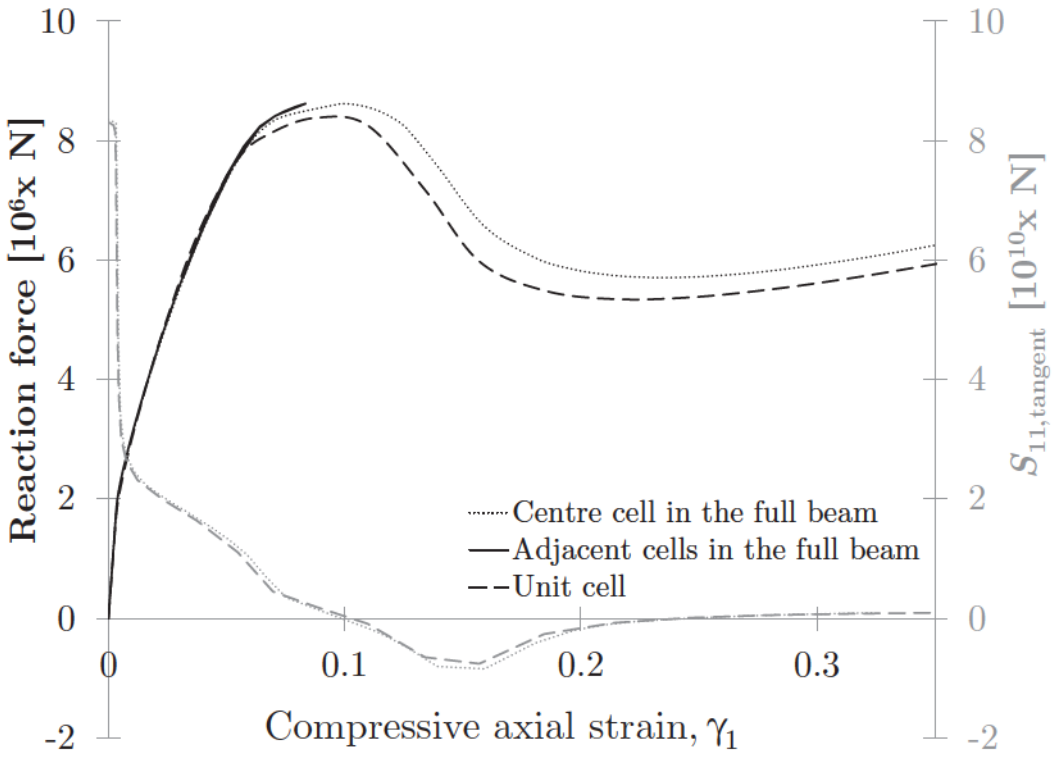

Figure 5.7.: Load (left axis, black lines) and tangent stiffness (right axis, 50% gray lines) as a function of axial compressive strain, γ_1. Please note that all adjacent cells in the full beam model follow the load strain path backwards once there is localisation.

Figure 5.8d). Note that after localisation has occurred, for a given load, various strain states are possible.

Note that a single unit cell with periodic boundary conditions predicts the conditions of the centre cell rather accurately thanks to the thickness of the transverse reinforcements, which means that there is no warping in the boundaries. It is stressed that this is a special case given the wall thickness and would not be observed with thinner walls. As described above, the choice of wall thickness was made for the local buckling to occur prior to the column buckling.

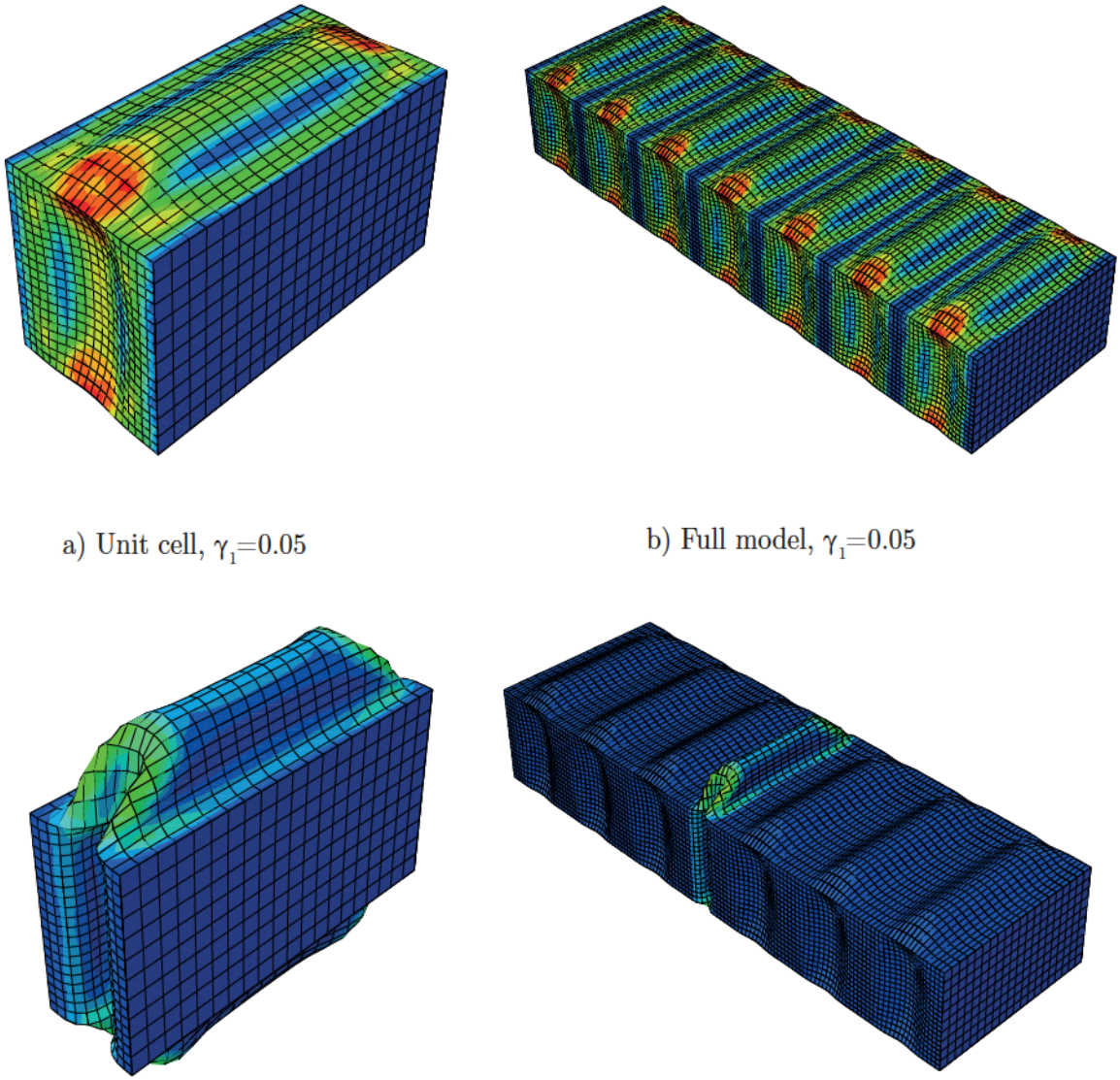

a) Unit cell, γ_1=0.05

b) Full model, γ_1=0.05

c) Unit cell, γ_1=0.35

d) Full model, γ_1=0.35

Figure 5.8.: Deformed shapes, with scale factor of one, for the unit cell and the full model of the reinforced box beam at different stages of the localisation process (contour plot shows corresponding von Mises stress).

5.2. Shear Effects on the determination of Normal Modes for an Anisotropic Prismatic Beam

In this final example, the natural frequencies of a composite beam are investigated using the current method. The geometry of the cross section, material and mesh refinement are those from section 4.1. The total length of the beam is ten times its width dimension: 0.1346m. The composite layup is b) from section 4.1. The 6×6 stiffness and mass matrices have been computed using the unit cell approach. This information is then used in the 1D-beam solver (see Eq. (2.29)) to assemble the global stiffness and mass matrices and an eigenvalue analysis is performed. The results of such analysis are included in Table 5.1. The first two modal frequencies show good agreement for the full 6×6 but this accuracy is decreased without shear components. The mode shapes for these two frequencies are bending in the vertical (shown in Figure 5.9) and horizontal directions with a quarter-wave type of deformation. The 3^{rd} and 4^{th} bending modes (three-quarter-wave type) indicate the need of a complete formulation, that is, which includes shear stiffness, in the calculation of composite beam natural frequencies. The discrepancy between the full 3-D model and the classical 4×4 approach for the highest frequency bending mode studied, reaches up to 7.9% while the full 6×6 achieves one order of magnitude better agreement ($\approx 0.5\%$). In the last frequency shown, which would correspond to a coupled torsional/bending mode, the present method deviates slightly (2.5%) from the full beam solution due to the lack of restrained warping effects [82]. Without properly capturing shear effects, the prediction is even worse for short beams because we know from Subsection 4.1.4 that shear-related end effects are present in a generous portion of the beam. In Figure 5.9 the deformed shape of the first bending/torsional mode has been plotted to show the large elastic couplings existing in this particular composite structure.

Table 5.1.: First five natural frequencies (in kHz) of a composite prismatic beam

	1^{st} **Mode**	2^{nd} **Mode**	3^{rd} **Mode**	4^{th} **Mode**	5^{th} **Mode**
Full Abaqus 3D	1.132	2.023	3.308	4.353	5.075
Unit cell+ 1D beam solver	1.135	2.028	3.324	4.377	5.203
Unit cell (4×4)**+ 1D beam solver**	1.215	2.140	3.578	4.649	5.881

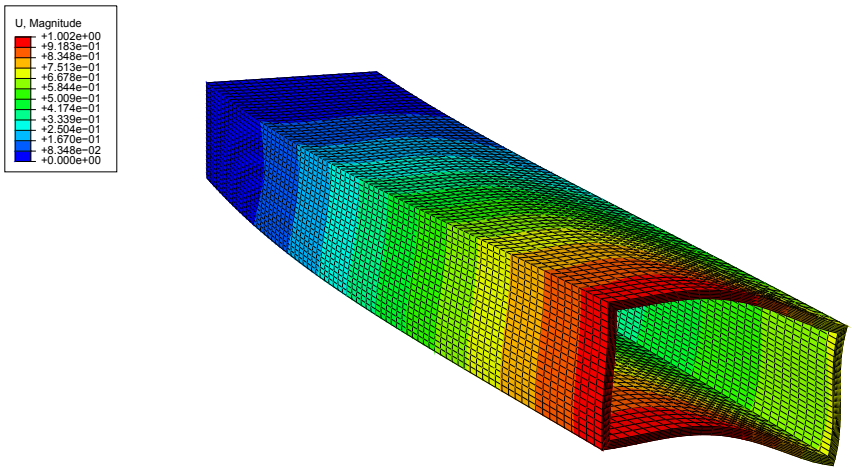

Figure 5.9.: 1^{st} mode of the composite beam. Note the coupling between bending and torsion.

Chapter 6

Conclusions and Recommendations

This chapter presents a summary of the main contributions and achievements of this multiscale analysis on slender periodic composite structures. The first section covers the main outcomes of the theoretical and practical characteristics of the approach presented in this work. Section 6.2 highlights the key accomplishments of this thesis which in turn provide the basis for the recommendations for future work and alternative applications of the presented technique.

6.1. Overall Conclusions

The design of novel aircraft configurations and ever more powerful wind turbines requires a set of tools that integrate the effects of the dynamics of the structure with the aerodynamic forces and the control mechanisms. For each configuration and set of test cases, it would be prohibitively costly and computationally unviable to simulate the full 3D structure. Hence beam models are used where the slenderness of the structure permits such idealisation. There are generally two steps present in the evaluation of the response from such beams. The solution step calculates the deformation and overall response of the beam subject to the external forces and all other inputs. This step is well developed and composite beam models [51] that include geometrically-nonlinear effects are readily available thanks to the contributions of, among others, Simo and Vu-Quoc [99]; Cardona and Géradin [12]

and Hodges [49][50]. The homogenisation step is related with the determination of the cross-sectional inertial and stiffness properties that better represent the actual behaviour of the real structure. This latter stage, on the other hand, was dealt with excessive assumptions or solved via mathematical implementations for which boundary conditions were hard to find. In this work, we showed a method of obtaining such properties by analysing a representative unit cell. This is, inherently, a more flexible description of the geometry of the beam than those based on constant cross sections [63][57]. The level of fidelity was also increased by including shear effects as opposed to the classical degrees of freedom [41], and the versatility and ease of implementation were greatly improved by the use of a standard finite element package.

The methodology that was presented here is based on the static analysis of a unit cell, which was assumed to be much smaller than the characteristic wavelength in the beam response. Assumptions on the definition of the global variables as an average of the local ones and the conservation of internal energy between scales yielded a final set of equations to obtain the beam cross sectional full stiffness matrix, that includes transverse shear effects. These equations were solved using periodic boundary conditions and additional zero-average rotation constraints for all sections in the transverse shear case. As a consequence of the use of this zero-average rotation constraint, it was impossible to calculate the shear stiffness coefficients for beams where the cross sections varied in the spanwise direction or that it had transverse reinforcements. In these situations, an alternative methodology that is able to isolate the shear loading from the bending moments remains to be found. The calculation of inertial properties was also included in the discretised model by summing all the contributions from each element.

Numerical examples were used to validate the proposed approach and the accuracy of the results for prismatic, cylindrical and aerofoil-like beams was verified. Taper was an interesting case –given that most modern aircraft wings and wind turbine blades have some taper in them– to which reasonable solutions were obtained

if several representative unit cells were used to populate the 1D beam solver, i.e. using a piecewise approximation. Consistently, the local buckling behaviour of the structure was correctly captured when the wavelength of the response was known a priori, both in terms of the load required to achieve buckling and the deformed shape when that occurred. In the compressive local buckling the phenomenon of localisation was explored to investigate the limits of applicability of the current method when the periodicity is broken. Fully geometrically-nonlinear and vibration analyses were also presented where the code developed for this application, SHARP.cells, was successfully coupled with the 1D beam solver, SHARP.beams. Overall the methodology performed as expected, with a level of accuracy in accordance with the discretisation level and demonstrated the advantages and flexibility of using a standard finite element package by making use of tie constraints to join the different parts that constituted the model. This was done without an impact on the homogenised stiffness calculation. While the local stress field would be affected by the presence of tie constraints, the method did achieve good ply-by-ply agreement recovering local stresses.

6.2. Key Contributions of this Thesis

The main contribution of this Thesis is the development of a complete homogenisation tool that is based on the analysis of representative unit cells to obtain the elastic and inertial properties of periodic composite beams, without the need for constant cross sections and using an unmodified, standard finite element package. The following specific key developments make this a novel and unique approach:

Unit cells with transverse reinforcements and periodic thickness variation.

Unlike many of the currently available methodologies, this approach is not restricted to axially-invariant cross sections. This fact makes the number of applications of the methodology much larger than if only constant cross sections were considered. Taking the example of HALE wings, the presence of

transverse reinforcements or ribs can adequately be dealt with now. Periodic thickness variation can also be accounted for if desired.

A one-step solution for transverse shear. The full 6×6 stiffness matrix is obtained without ad hoc assumptions on the warping field. This is valid for composite materials with arbitrary layups and the transverse shear response is calculated in a single analysis step.

Meshing flexibility and tie constraints. The cross sectional and unit-cell geometries are fully parametrised, ready to be linked to an optimisation algorithm or simply to assess the sensitivity of the structure to a given variable. Using tie constraints allows for arbitrary positioning and meshing of reinforcement subcomponents such as ribs, spars and webs which is a clear advantage in the conceptual design when the final geometry is not yet defined.

Efficient coupling with a 1D beam solver. This homogenisation method has been successfully and seamlessly linked to a 1D beam solver to provide the latter with accurate cross-sectional properties and also to use information on the current values of strain to update the stiffness of the structure.

6.3. Impact and Significance of this Research

The work presented in this dissertation has led to the publication of the following journal and conference papers:

- Julian Dizy, Rafael Palacios and Silvestre T. Pinho. Homogenization of slender periodic composite structures. In *Proceedings of the 53rd AIAA/ASME/ASCE/AHS/ASC Structures, Structural Dynamics and Materials Conferences. Honolulu, Hawaii, AIAA-2012-1949*, 2012. doi: 10.2514/6.2012-1949

- Julian Dizy, Rafael Palacios and Silvestre T. Pinho. Homogenisation of slender periodic composite structures. *International Journal of Solids and Structures*, 50(9):1473 - 1481, 2013. ISSN 0020-7683. doi: 10.1016/j.ijsolstr.2013.01.017

- Julian Dizy, Rafael Palacios and Silvestre Pinho. Shear effects in the homogenisation of slender composite wings. In *Proceedings of the 5th European Conference for Aeronautics and Space Sciences (EUCASS). Munich, Germany, EUCASS-2013*, 2013.

The research contained in this thesis was awarded the following international awards:

- **Lockheed Martin award** for best student paper in structures. (53^{rd} AIAA SDM Conference).
- **Astrium award** for best student paper. (5^{th} EUCASS Conference).

6.4. Recommendations for Future Work

The homogenisation tool developed in this dissertation has proven to be an efficient and flexible approach for modelling anisotropic slender structures. The numerical cases that have been presented herein demonstrated the capabilities of SHARP.cells code to deal with complex cross sections and material configurations, the accuracy of the properties obtained –including the transverse shear– and the diverse range of analysis types that can be applied to the unit cell representation of the beam. To conclude, we present an overview of the main aspects of this approach that could be further improved in order to broaden its applicability and a number of features that could be added to it:

Including transverse shear for non-constant cross sections is a natural improvement to the current formulation. Recalling the requirements for the isolation of transverse shear from the corresponding bending moments, zero average rotations (or moments of area) were necessarily imposed to each of the sections of the unit cell. This ensured that no bending energy was present when the solution for the shear stiffness was sought. Having spanwise variations in the unit cell would mean that the bending moment component of the shear loading would no longer be constant throughout the unit cell and

could not be cancelled out as explained. This enhancement would certainly benefit the completeness of the current approach.

Open-section beams have a torsional stiffness much smaller than either bending stiffness and they experience heavy nonlinear coupling between these degrees of freedom. They also exhibit the so-called "trapeze effect", which is a nonlinear effect due to extension-torsion coupling in beams undergoing large axial forces. It is so named because a trapeze, when twisted slightly under an axial force, tends to restore itself to zero with a restoring moment that it is a function of both the angle and the axial force [51]. This effect is very relevant when dealing with helicopter rotor blades, propellers and turbomachinery blades as they all have to cope with large centrifugal forces [86]. It leads to an effective torsional rigidity that varies with axial force. Additionally, thin-walled open-section beams show Vlasov effects (restrained warping at the boundaries) that make it complicated to determine their buckling behaviour [58]. Extending the current theory to treat thin-walled open-section beams requires dealing with the aforementioned problems and assuring that the solutions are consistent for a variety of open-section shapes.

Distributed loads create beam responses that require polynomial approximations one order higher than those obtained from tip-applied moments and forces. Furthermore, for distributed loads that are not constant (e.g. linear, quadratic, etc.) the order of the polynomial required to describe the periodic boundary conditions would further increase [63]. While it is desirable to deal with this type of loading directly in the homogenisation step, (for example to account for a uniform distribution of lift along the span of the wing), it is a formidable challenge to adapt the present method, that deals with a unit cell with reinforcements and spanwise variations, to account for this directly. Instead, distributed loads can still be applied to the 1D beam solver and approximate solutions obtained that way.

Non-classical beam deformations are degrees of freedom that can be added to the classical six in beam models to increase the accuracy of the response, in particular to vibration analysis. Also known as finite section modes [82], these are more evident in shorter beams and could be added to SHARP.cells to increase the accuracy in the calculation of the normal modes. Figure 5.9 shows one of these modes.

Debonding between components could be studied with the present approach. Multiple parts are used in the current model and these are bonded together using tie constraints. This could easily be replaced with a row of cohesive elements and hence the debonding behaviour under real strain conditions (obtained directly from the coupled 1D beam solver) could be predicted. This would assume that all unit cells behave in a similar fashion, i.e. debonding is periodic. Moreover, delamination and other material failure modes could be added to further improve predictions on the structural integrity of the beam.

Optimisation and aeroelastic tailoring can be explored thanks to the parametrisation of the code and its meshing flexibility. This would allow for the directionality and the inherent couplings present in composite materials to be used as an advantage to obtain desired aeroelastic properties and achieve significant weight reductions [45]. In terms of optimisation, any of the model parameters (thickness, number of plies, position of stringers, etc.) could be optimised for a given stiffness components by interfacing SHARP.cells with the MATLAB® Optimisation Toolbox.

Appendices

Appendix A

Equations of motion of the GECB

This appendix contains the detailed steps to solve the dynamic equations of motion for the composite beam solver used in this work, which was outlined in Section 2.3.

Infinitesimal Beam Kinematics

Expressions for the infinitesimal changes on the beam force and moment strains are obtained by taking variations on the beam strains and curvatures given in Eq. (2.24). This results in the virtual strain-displacement relations, which are written as

$$\begin{aligned} \delta\gamma &= C\delta u'_A(s,t) + \widetilde{u}'_A\delta\Phi_B, \\ \delta\kappa &= \delta\Phi'_B + \widetilde{K}_B\delta\Phi_B, \end{aligned} \tag{A.1}$$

where the local virtual rotation vector, $\delta\Phi_B$, and the local curvature, K_B, are parametrised using the relation as $\delta\widetilde{\Phi}_B = C\delta C^\top = T\widetilde{\delta\Psi}$ and $\widetilde{K}_B = C\left(C^\top\right)' = T\widetilde{(\Psi)\,\Psi'}$, respectively [40]. In a similar fashion, variation of the inertial velocities leads to the expressions of infinitesimal beam velocities as

$$\begin{aligned} \delta V_B &= C\left(\delta\dot{u}_A + \widetilde{\omega}_A\delta u_A - \widetilde{u}_A\delta\omega_A + \delta v_A\right) + \widetilde{V}_B\delta\Phi, \\ \delta\Omega_B &= \delta\dot{\Phi}_B + \widetilde{\Omega}_B\delta\Phi_B + C\delta\omega_A. \end{aligned} \tag{A.2}$$

For a derivation of the variation of the inertial rigid-body velocities please see [46]. This derivation of the beam kinematics highlights the benefits of using the CRV for

the parametrisation of the cross-sectional orientations leading to compact definitions of the local strain and velocity measures, which will be applied next to develop expressions for the virtual work and energy densities of the flexible aircraft. The solution process of the resulting transient equations requires linearisation of the beam equations, which will repeatedly involve variations of the rotation operator C, and the tangential rotation operator, T. The latter is given for an arbitrary 3×1 column matrix, h, as [40]

$$\begin{aligned}\delta T(\Psi) h = A_1(\Psi, h) =& \phi^{-2}(1-\cos\phi)\widetilde{h} + \phi^{-1}\left[\sin\phi - 2\phi^{-1}(1-\cos\phi)\right]\widetilde{h}nn^{\top} + \\ & \phi^{-1}\left(2+\cos\phi-3\phi^{-1}\sin\phi\right)\widetilde{n}\widetilde{h}nn^{\top} + \\ & \phi^{-1}\left(1-\phi^{-1}\sin\phi\right)\left(\widetilde{h}\widetilde{n}-2\widetilde{n}\widetilde{h}\right),\end{aligned} \tag{A.3}$$

with the Cartesian rotation vector written as before with $\Psi = \phi n$.

Internal and Kinetic Energy Densities

We can now write the virtual strain and kinetic energies as [49]

$$\begin{aligned}\delta\mathcal{U} &= \begin{bmatrix}\delta\gamma^{\top} & \delta\kappa^{\top}\end{bmatrix} S \begin{bmatrix}\gamma^{\top} & \kappa^{\top}\end{bmatrix}^{\top} = \begin{bmatrix}\delta\gamma^{\top} & \delta\kappa^{\top}\end{bmatrix}\begin{bmatrix}\mathbb{F}_B^{\top} & \mathbb{M}_B^{\top}\end{bmatrix}^{\top}, \\ \delta\mathcal{T} &= \begin{bmatrix}\delta V_B^{\top} & \delta\Omega_B^{\top}\end{bmatrix} M \begin{bmatrix}V_B^{\top} & \Omega_B^{\top}\end{bmatrix}^{\top} = \begin{bmatrix}\delta V_B^{\top} & \delta\Omega_B^{\top}\end{bmatrix}\begin{bmatrix}P_B^{\top} & H_B^{\top}\end{bmatrix}^{\top},\end{aligned} \tag{A.4}$$

where we have introduced the internal forces and moments, $\mathbb{F}_B$ and $\mathbb{M}_B$, and the local translational and angular momenta, P_B and H_B, respectively. In the above expression the internal energy in the deformation of the flexible vehicle was defined by the linearised strain energy, which is valid if the deformations of the flexible body remain in the linear elastic regime of the material properties. Note however that this does not prevent displacements and rotations from being large.

The 6×6 cross-sectional mass and stiffness matrices, M and S, in Eq. (A.4) are obtained through the homogenisation technique presented in the body of this thesis.

Virtual Work of External Forces

Consider next the applied volume (or surface) forces μ_G acting on the beam sections. The corresponding virtual work per unit length is $\delta\mathcal{W} = \left\langle \delta X_G^\top \mu_B \right\rangle$, where δX_G is the virtual position vector in the current configuration at the material points where forces μ_G are applied, and $\langle \bullet \rangle$ is the integral over the area (or area contour) of the local cross section. The position vector of an arbitrary point on the local cross section for a static body-fixed reference frame[1], A is simply

$$X_G = u_A + C^\top \xi_B, \tag{A.5}$$

where ξ_B are the local cross-sectional coordinates in the local material frame B. From the definition of the position vector X_G, the virtual work per unit length is

$$\delta\mathcal{W} = \delta u_A^\top C^\top F_B + \delta\Phi_B^\top M_B, \tag{A.6}$$

where the concept of the local virtual rotation $\delta\widetilde{\Phi}_B = C\delta C^\top$ was introduced above [40]. The set of resultant forces and moments per unit beam length is then given as

$$\begin{aligned} F_B &= \langle \mu_B \rangle, \\ M_B &= \langle \widetilde{\xi}_B \mu_B \rangle. \end{aligned} \tag{A.7}$$

Equations of Motion at an Arbitrary Reference Line

Finally, all virtual magnitudes are expressed in terms of the independent set of variables, through the kinematic relations introduced in Eqs. (A.1) and (A.2). Substitution of the contributions of the virtual work and the energy densities in Eqs. (A.6) and (A.4), respectively, into the expressions of Hamilton's principle, Eq. (2.26), and integration by parts in time leads to the weak form of the beam dynamics

[1] For a complete formulation, with a moving body-fixed frame, A, with respect to the inertial frame, G, please refer to [46] for more details.

EoM as [83]

$$\begin{aligned}
&\int_{t_1}^{t_2} \Big\{ \int_L \Big\{ \delta u_A^\top C^\top \left(\dot{P}_B + \widetilde{\Omega}_B P_B - F_B \right) + \delta u'^\top_A C^\top \mathbb{F}_B \\
&\qquad + \delta \Phi_B^\top \left[\dot{H}_B + \widetilde{\Omega}_B H_B + \widetilde{V}_B P_B - \widetilde{K}_B \mathbb{M}_B - \widetilde{u'}_A F_B - M_B \right] + \delta \Phi'^\top_B \mathbb{M}_B \Big\} dy \\
&\quad + \delta r_G^\top C^{GA} \left[\dot{P}_A^u + \widetilde{\omega}_A P_A^u - F_A^u \right] + \delta \varphi_A^\top \left[\dot{H}_A^u + \widetilde{\omega}_A H_A^u - M_A^u \right] \Big\} dt = \\
&= \int_L \left[\delta u_A^\top C^\top P_B + \delta \Phi_B^\top H_B \right]_{t_1}^{t_2} dy + \left[\delta r_G^\top C^{GA} P_A^u + \delta \varphi_A^\top H_A^u \right]_{t_1}^{t_2}
\end{aligned} \tag{A.8}$$

The local momenta, P_B and H_B, and the internal forces, $\mathbb{F}_B$ and $\mathbb{M}_B$, respectively, are expressed in the local material frame B and have been defined in Eq. (A.4). The total momenta and external forces can be obtained in the global body-fixed reference frame A through integration over all reference lines of the multi-beam configuration as

$$\begin{aligned}
P_A^u &= \int_L C^\top P_B dy, \quad H_A^u = \int_L \left(\widetilde{u}_A C^\top P_B + C^\top H_B \right) dy, \\
F_A^u &= \int_L C^\top f_B dy, \quad M_A^u = \int_L \left(\widetilde{u}_A C^\top F_B + C^\top M_B \right) dy.
\end{aligned} \tag{A.9}$$

Discrete Form of the Equations of Motions

To solve the governing beam EoM, Eq. (A.8), the position vector, u_A, and the Cartesian rotation vector, Ψ, are approximated using a finite-element discretisation in terms of the the shape functions $N_i(s)$ as [40]

$$\begin{aligned}
u_A(s) &\cong \sum_{i=1}^{3} N_i(s) u_{Ai}, \\
\Psi(s) &\cong \sum_{i=1}^{3} N_i(s) \Psi_i,
\end{aligned} \tag{A.10}$$

where u_{Ai} and Ψ_i are the nodal values of the position and rotation parameters. The beam model has been implemented using 2- and 3-noded elements which corresponds to linear and quadratic interpolations, respectively [46]. There are known issues with *objectivity* of the interpolation operation of finite rotations [4, 29], however, good

performance of the implementation is observed for quadratic elements or fine enough discretisation with linear elements.

If η is the column vector with all the nodal displacements and rotations and $\beta^\top = \{v_A^\top \;\; \omega_A^\top\}$, the discrete form of the dynamic equation, Eq. (A.8), is written in compact form as

$$\mathcal{M}(\eta)\begin{Bmatrix}\ddot{\eta}\\ \dot{\beta}\end{Bmatrix} + \begin{Bmatrix}Q^S_{gyr}\\ Q^R_{gyr}\end{Bmatrix} + \begin{Bmatrix}Q^S_{stif}\\ 0\end{Bmatrix} = \begin{Bmatrix}Q^S_{ext}\\ Q^R_{ext}\end{Bmatrix}, \tag{A.11}$$

where structural and rigid-body components (denoted by superscripts S and R) have been identified in the gyroscopic, stiffness and external forces. The discrete generalised forces in the above equation are written as

$$\begin{aligned} Q^S_{stif}(\eta) &= \int_\Gamma \left(N^\top \Upsilon^\top A_K + N^\top \Upsilon'^\top + N'^\top \Lambda^\top\right)\hat{\mathbb{F}}dy,\\ Q_{gyr}(\eta,\dot{\eta},\beta) &= \int_\Gamma \begin{bmatrix}\Lambda N & A_{RC}\end{bmatrix}^\top \left(\mathcal{M}_{cs}\hat{V}_{gyr} + A_{V\Omega}\mathcal{M}_{cs}\hat{V}\right)dy,\\ Q_{ext}(\eta,\dot{\eta},\beta,\zeta) &= \int_\Gamma \begin{bmatrix}\Lambda N & A_{RC}\end{bmatrix}^\top \hat{F}dy, \end{aligned} \tag{A.12}$$

where ζ is the orientation of the body-fixed reference system, and, assuming a flat Earth, is defined as [104]

$$\begin{Bmatrix}\dot{\zeta}_0\\ \dot{\zeta}_v\end{Bmatrix} = -\frac{1}{2}\begin{bmatrix}0 & \omega_A^\top\\ \omega_A & \widetilde{\omega}_A\end{bmatrix}\begin{Bmatrix}\zeta_0\\ \zeta_v\end{Bmatrix}. \tag{A.13}$$

Also, the following variables for resultant loads, local inertial velocities, and internal forces have been defined to simplify notation,

$$\hat{F} = \begin{Bmatrix}F_B\\ M_B\end{Bmatrix},\;\; \hat{V} = \begin{Bmatrix}V_B\\ \Omega_B\end{Bmatrix},\;\; \hat{\mathbb{F}} = \begin{Bmatrix}\mathbb{F}_B\\ \mathbb{M}_B\end{Bmatrix}. \tag{A.14}$$

The gyroscopic velocities $\hat{V}_{gyr}$ in the definition of the gyroscopic forces, Q_{gyr} in Eq. (A.12), are given as

$$\hat{V}_{gyr}(\eta,\dot{\eta},\beta) = \begin{Bmatrix}V_{gyr}\\ \Omega_{gyr}\end{Bmatrix} = \begin{Bmatrix}C\widetilde{\omega}_A\dot{u}_A + \widetilde{V}_B T\dot{\Psi}\\ \dot{T}\dot{\Psi} + \widetilde{\Omega}_B T\dot{\Psi}\end{Bmatrix}, \tag{A.15}$$

and the following 6×6 matrix operators were used in the definition of the discrete generalised forces,

$$\Upsilon = \begin{bmatrix} I & 0 \\ 0 & T \end{bmatrix}, \quad A_K = \begin{bmatrix} 0 & 0 \\ -\widetilde{u}'_A & -\widetilde{K}_B \end{bmatrix}, \quad A_{V\Omega} = \begin{bmatrix} \widetilde{\Omega}_B & 0 \\ \widetilde{V}_B & \widetilde{\Omega}_B \end{bmatrix}. \tag{A.16}$$

The tangent mass matrices have been defined as a function of the deformed state, η, as

$$\mathcal{M}(\eta) = \begin{bmatrix} \mathcal{M}^{SS} & \mathcal{M}^{SR} \\ \mathcal{M}^{RS} & \mathcal{M}^{RR} \end{bmatrix} = \int_\Gamma \begin{bmatrix} \Lambda N & A_{RC} \end{bmatrix}^\top \mathcal{M}_{cs} \begin{bmatrix} \Lambda N & A_{RC} \end{bmatrix}, \tag{A.17}$$

where the operators Λ and A_{RC} are defined as

$$\begin{Bmatrix} V_B \\ \Omega_B \end{Bmatrix} = \Lambda \begin{Bmatrix} \dot{u}_A \\ \dot{\Psi} \end{Bmatrix} + A_{RC} \begin{Bmatrix} v_A \\ \omega_A \end{Bmatrix}, \tag{A.18}$$

to obtain the compact form of the inertial velocities. The resulting set of nonlinear second-order differential EoM, Eq. (A.11), couples the geometrically-nonlinear beam dynamics with the nonlinear rigid-body motion of the flexible body through the inertial and gyroscopic forcing terms. This completes the full derivation of the beam equations presented in Section 2.3.

Bibliography

[1] R.J. Astley. *Finite elements in solids and structures. An introduction.* Chapman & Hall (Springer), 1992.

[2] M. Aydogdu. A general nonlocal beam theory: its application to nanobeam bending, buckling and vibration. *Physica E: Low-dimensional Systems and Nanostructures*, 41(9):1651–1655, 2009.

[3] J.R. Banerjee and A.J. Sobey. Dynamic stiffness formulation and free vibration analysis of a three-layered sandwich beam. *International Journal of Solids and Structures*, 42(8):2181 – 2197, 2005. doi: http://dx.doi.org/10.1016/j.ijsolstr.2004.09.013.

[4] O.A. Bauchau, A. Epple, and S. Heo. Interpolation of finite rotations in flexible multi-body dynamics simulations. *Proceedings of the Institution of Mechanical Engineers, Part K: Journal of Multi-body Dynamics*, 222(4):353–366, 2008.

[5] F.P. Beer and E.R. Johnston Jr. Mechanics of materials, 1981, 1974.

[6] V.L. Berdichevskii. Variational-asymptotic method of constructing a theory of shells: Pmm vol. 43, no. 4, 1979, pp. 664–687. *Journal of Applied Mathematics and Mechanics*, 43(4):711–736, 1979.

[7] V.L. Berdichevskii. On the energy of an elastic rod. *Journal of Applied Mathematics and Mechanics*, 45(4):518–529, 1981.

[8] C.A. Brassey, L. Margetts, A.C. Kitchener, P.J. Withers, P.L. Manning, and W.I. Sellers. Finite element modelling versus classic beam theory: comparing methods for stress estimation in a morphologically diverse sample of vertebrate long bones. *Journal of The Royal Society Interface*, 10(79), 2013.

[9] N. Buannic and P. Cartraud. Higher-order effective modeling of periodic heterogeneous beams. i. asymptotic expansion method. *International Journal of Solids and Structures*, 38(40):7139–7161, 2001.

[10] N. Buannic and P. Cartraud. Higher-order effective modeling of periodic heterogeneous beams. ii. derivation of the proper boundary conditions for the

interior asymptotic solution. *International Journal of Solids and Structures*, 38(40):7163–7180, 2001.

[11] N. Buannic, P. Cartraud, and T. Quesnel. Homogenization of corrugated core sandwich panels. *Composite Structures*, 59(3):299–312, 2003.

[12] A. Cardona and M. Géradin. A beam finite element non-linear theory with finite rotations. *International journal for numerical methods in engineering*, 26(11):2403–2438, 1988.

[13] T.G. Carne and G.H. James III. The inception of OMA in the development of modal testing technology for wind turbines. *Mechanical Systems and Signal Processing*, 24(5):1213 – 1226, 2010. doi: http://dx.doi.org/10.1016/j.ymssp.2010.03.006.

[14] E. Carrera and G. Giunta. Refined beam theories based on a unified formulation. *International Journal of Applied Mechanics*, 2(01):117–143, 2010.

[15] E. Carrera, G. Giunta, P. Nali, and M. Petrolo. Refined beam elements with arbitrary cross-section geometries. *Computers & Structures*, 88(56):283 – 293, 2010. doi: http://dx.doi.org/10.1016/j.compstruc.2009.11.002.

[16] E. Carrera, M. Petrolo, and P. Nali. Unified formulation applied to free vibrations finite element analysis of beams with arbitrary section. *Shock and Vibration*, 18(3):485–502, 2011.

[17] P. Cartraud and T. Messager. Computational homogenization of periodic beam-like structures. *International Journal of Solids and Structures*, 43(3): 686–696, 2006.

[18] C.E.S. Cesnik and E.L. Brown. Modeling of high aspect ratio active flexible wings for roll control. In *Proceedings of the 43rd AIAA/ASME/ASCE/AHS Structures, Structural Dynamics, and Materials Conferences, Denver, CO*, 2002.

[19] C.E.S. Cesnik and D.H. Hodges. Vabs: a new concept for composite rotor blade cross-sectional modeling. *Journal of the American Helicopter Society*, 42(1):27–38, 1997.

[20] C.E.S. Cesnik and M. Ortega-Morales. Active composite beam cross-sectional modeling-stiffness and active force constants. In *Proceedings of the 40th AIAA Structures, Structural Dynamics and Materials Conferences. St. Louis, Missouri, AIAA-99-1548*, 1999.

[21] C.E.S. Cesnik and W. Su. Nonlinear aeroelastic simulation of x-hale: a very flexible uav. In *49th AIAA Aerospace Sciences Meeting including the New Horizons Forum and Aerospace Exposition, Orlando, Florida*, 2011.

[22] U.K. Chakravarty. On the modeling of composite beam cross-sections. *Composites Part B: Engineering*, 42(4):982 – 991, 2011. doi: http://dx.doi.org/10.1016/j.compositesb.2010.10.012.

[23] H. Chen, W. Yu, and M. Capellaro. A critical assessment of computer tools for calculating composite wind turbine blade properties. *Wind Energy*, 13(6): 497–516, 2010. doi: 10.1002/we.372.

[24] H. Cohen. A non-linear theory of elastic directed curves. *International Journal of Engineering Science*, 4(5):511–524, 1966.

[25] R.D. Cook. *Concepts and applications of finite element analysis: a treatment of the finite element method as used for the analysis of displacement, strain, and stress*. Wiley, 1974.

[26] R.D. Cook. *Finite element modeling for stress analysis*. John Wiley & Sons, Inc., 1994.

[27] R.G. Cook, R. Palacios, and P. Goulart. Robust gust alleviation and stabilization of very flexible aircraft. *AIAA Journal*, 51(2):330–340, 2013.

[28] E. Cosserat, F. Cosserat, M. Brocato, and K. Chatzis. *Théorie des corps déformables*. A. Hermann Paris, 1909.

[29] M.A. Crisfield and G. Jelenić. Objectivity of strain measures in the geometrically exact three-dimensional beam theory and its finite-element implementation. *Proceedings of the Royal Society of London. Series A: Mathematical, Physical and Engineering Sciences*, 455(1983):1125–1147, 1999.

[30] D.A. Danielson and D.H. Hodges. Nonlinear beam kinematics by decomposition of the rotation tensor. *Journal of Applied Mechanics*, 54:258, 1987.

[31] M. de Saint-Venant. *Mémoire sur la torsion des prismes: avec des considérations sur leur flexion ainsi que sur l'équilibre intérieur des solides élastiques en général: et des formules pratiques pour le calcul de leur résistance à divers efforts s' exerçant simultanément*. Imprimerie nationale, 1856.

[32] S.B. Dong, C. Alpdogan, and E. Taciroglu. Much ado about shear correction factors in timoshenko beam theory. *International Journal of Solids and Structures*, 47(13):1651 – 1665, 2010. doi: http://dx.doi.org/10.1016/j.ijsolstr.2010.02.018.

[33] J.A. Dourakopoulos and E.J. Sapountzakis. Postbuckling analysis of beams of arbitrary cross section using BEM. *Engineering Structures*, 32(11):3713–3724, 2010. doi: http://dx.doi.org/10.1016/j.engstruct.2010.08.016.

[34] J.L. Ericksen and C. Truesdell. Exact theory of stress and strain in rods and shells. *Archive for Rational Mechanics and Analysis*, 1(1):295–323, 1957.

[35] A.C. Eringen. On differential equations of nonlocal elasticity and solutions of screw dislocation and surface waves. *Journal of Applied Physics*, 54(9): 4703–4710, 1983.

[36] A.C. Eringen. *Nonlocal continuum field theories*. Springer, 2002.

[37] Z. Friedman and J.B. Kosmatka. Exact stiffness matrix of a nonuniform beam I. extension, torsion, and bending of a bernoulli-euler beam. *Computers & Structures*, 42(5):671 – 682, 1992. doi: http://dx.doi.org/10.1016/0045-7949(92)90179-4.

[38] Z. Friedman and J.B. Kosmatka. Exact stiffness matrix of a nonuniform beam II. bending of a timoshenko beam. *Computers & Structures*, 49(3):545 – 555, 1993. doi: http://dx.doi.org/10.1016/0045-7949(93)90056-J.

[39] M.G.D. Geers, V.G. Kouznetsova, and W.A.M. Brekelmans. Multi-scale computational homogenization: Trends and challenges. *Journal of computational and applied mathematics*, 234(7):2175–2182, 2010.

[40] M. Géradin and A. Cardona. *Flexible multibody dynamics: a finite element approach*. John Wiley, 2001.

[41] G.L. Ghiringhelli and P. Mantegazza. Linear, straight and untwisted anisotropic beam section properties from solid finite elements. *Composites Engineering*, 4(12):1225–1239, 1994.

[42] V. Giavotto, M. Borri, P. Mantegazza, G. Ghiringhelli, V. Carmaschi, G.C. Maffioli, and F. Mussi. Anisotropic beam theory and applications. *Computers & Structures*, 16(14):403 – 413, 1983. doi: http://dx.doi.org/10.1016/0045-7949(83)90179-7.

[43] A.E. Green and N. Laws. A general theory of rods. *Proceedings of the Royal Society of London. Series A. Mathematical and Physical Sciences*, 293(1433): 145–155, 1966.

[44] F. Gruttmann and W. Wagner. Shear correction factors in timoshenko's beam theory for arbitrary shaped cross-sections. *Computational Mechanics*, 27(3): 199–207, 2001. doi: 10.1007/s004660100239.

[45] S. Guo. Aeroelastic optimization of an aerobatic aircraft wing structure. *Aerospace Science and Technology*, 11(5):396 – 404, 2007. doi: http://dx.doi.org/10.1016/j.ast.2007.01.003.

[46] H. Hesse. *Consistent aeroelastic linearisation and reduced-order modelling in the dynamics of manoeuvring flexible aircraft*. PhD thesis, Imperial College London, 2013.

[47] H. Hesse and R. Palacios. Consistent structural linearisation in flexible-body dynamics with large rigid-body motion. *Computers and Structures*, 110:1–14, 2012.

[48] G.F.J. Hill and P.M. Weaver. Analysis of arbitrary beam sections with non-homogeneous anisotropic material properties. In *Proceedings of the 13th International Conference on Composite Materials, Beijing*, volume 501, page 1285, 2001.

[49] D.H. Hodges. A mixed variational formulation based on exact intrinsic equations for dynamics of moving beams. *International journal of solids and structures*, 26(11):1253–1273, 1990.

[50] D.H. Hodges. Geometrically exact, intrinsic theory for dynamics of curved and twisted anisotropic beams. *AIAA journal*, 41(6):1131–1137, 2003.

[51] D.H. Hodges. Nonlinear composite beam theory. *Progress in astronautics and aeronautics*, 213:304, 2006.

[52] C.O. Horgan and J.G. Simmonds. Saint-venant end effects in composite structures. *Composites Engineering*, 4(3):279–286, 1994.

[53] K.M. Hsiao, J.Y. Lin, and W.Y. Lin. A consistent co-rotational finite element formulation for geometrically nonlinear dynamic analysis of 3-d beams. *Computer Methods in Applied Mechanics and Engineering*, 169(1): 1–18, 1999.

[54] D. Ieşan. On saint-venant's problem. *Archive for Rational Mechanics and Analysis*, 91(4):363–373, 1986.

[55] D. Ieşan. On the theory of uniformly loaded cylinders. *Journal of Elasticity*, 16(4):375–382, 1986.

[56] G. Jelenić and M.A. Crisfield. Geometrically exact 3d beam theory: implementation of a strain-invariant finite element for statics and dynamics. *Computer Methods in Applied Mechanics and Engineering*, 171(1):141–171, 1999.

[57] Y. Jonnalagadda and J.D. Whitcomb. Calculation of effective section stiffness properties for wind turbine blades using homogenization. *Wind Energy*, 2012.

[58] N.R. Bauld Jr. and T. Lih-Shyng. A vlasov theory for fiber-reinforced beams with thin-walled open cross sections. *International Journal of Solids and Structures*, 20(3):277 – 297, 1984. doi: http://dx.doi.org/10.1016/0020-7683(84)90039-8.

[59] S.N. Jung, V.T. Nagaraj, and I. Chopra. Assessment of composite rotor blade modeling techniques. *Journal of the American Helicopter Society*, 44 (3):188–205, 1999. doi: http://dx.doi.org/10.4050/JAHS.44.188.

[60] S.N. Jung, V.T. Nagaraj, and I. Chopra. Refined structural model for thin-and thick-walled composite rotor blades. *AIAA journal*, 40(1):105–116, 2002.

[61] M. Jureczko, M. Pawlak, and A. Mezyk. Optimisation of wind turbine blades. *Journal of Materials Processing Technology*, 167(23):463 – 471, 2005. doi: http://dx.doi.org/10.1016/j.jmatprotec.2005.06.055.

[62] S. Kaewunruen, J. Chiravatchradej, and So. Chucheepsakul. Nonlinear free vibrations of marine risers/pipes transporting fluid. *Ocean Engineering*, 32(3): 417–440, 2005.

[63] G.J. Kennedy and J.R.R.A. Martins. A homogenization-based theory for anisotropic beams with accurate through-section stress and strain prediction. *International Journal of Solids and Structures*, 2011.

[64] G.J. Kennedy, J.S. Hansen, and J.R.R.A. Martins. A timoshenko beam theory with pressure corrections for layered orthotropic beams. *International Journal of Solids and Structures*, 48(1617):2373 – 2382, 2011. doi: http://dx.doi.org/10.1016/j.ijsolstr.2011.04.009.

[65] J.S. Kim and K.W. Wang. Vibration analysis of composite beams with end effects via the formal asymptotic method. *Journal of Vibration and Acoustics*, 132(4), 2010.

[66] M.Y. Kim, H.-T. Yun, and N.I. Kim. Exact dynamic and static element stiffness matrices of nonsymmetric thin-walled beam-columns. *Computers & Structures*, 81(14):1425 – 1448, 2003. ISSN 0045-7949. doi: http://dx.doi.org/10.1016/S0045-7949(03)00082-8.

[67] F. Kreupl, A.P Graham, G.S. Duesberg, W. Steinhagl, M. Liebau, E. Unger, and W. Hanlein. Carbon nanotubes in interconnect applications. *Microelectronic Engineering*, 64(14):399 – 408, 2002. ISSN 0167-9317. doi: http://dx.doi.org/10.1016/S0167-9317(02)00814-6.

[68] C.Y. Lee and W. Yu. Variational asymptotic modeling of composite beams with spanwise heterogeneity. *Computers & Structures*, 89(15):1503–1511, 2011.

[69] A.Y.T. Leung. *Dynamic stiffness and substructures*. Springer-Verlag Berlin, 1993.

[70] C. Li and T.W. Chou. A structural mechanics approach for the analysis of carbon nanotubes. *International Journal of Solids and Structures*, 40(10): 2487–2499, 2003.

[71] A.E.H. Love. A mathematical treatise on the theory of elasticity. *Dover, New York*, 1944.

[72] D.J. Lucia. The sensorcraft configurations: A non-linear aeroservoelastic challenge for aviation. In *46th AIAA/ASME/ASCE/AHS/ASC Structures, Structural Dynamics & Materials Conference, AIAA 2005-1943*, 2005.

[73] J.F. Mandell, D.D. Samborsky, D.W. Combs, M. E. Scott, and D.S. Cairns. *Fatigue of Composite Material Beam Elements Representative of Wind Turbine Blade Substructure*. Jan 1998. doi: 10.2172/14386.

[74] C.W. McCormick. *The NASTRAN User's Manual:(Level 15)*. National Aeronautics and Space Administration, Scientific and Technical Information Office, 1973.

[75] T. Messager and P. Cartraud. Homogenization of helical beam-like structures: application to single-walled carbon nanotubes. *Computational Mechanics*, 41 (2):335–346, 2008. doi: 10.1007/s00466-007-0189-3.

[76] V.G. Mokos and E.J. Sapountzakis. A {BEM} solution to transverse shear loading of composite beams. *International Journal of Solids and Structures*, 42(11â€“12):3261 – 3287, 2005. ISSN 0020-7683. doi: http://dx.doi.org/10.1016/j.ijsolstr.2004.11.005.

[77] J. Murua, R. Palacios, and J.M.R. Graham. Assessment of wake-tail interference effects on the dynamics of flexible aircraft. *AIAA journal*, 50 (7):1575–1585, 2012.

[78] M. MusiaÅ,. Static and dynamic stiffness of reinforced concrete beams. *Archives of Civil and Mechanical Engineering*, 12(2):186 – 191, 2012. ISSN 1644-9665. doi: http://dx.doi.org/10.1016/j.acme.2012.04.005.

[79] B.F. Ng, R. Palacios, J.M.R. Graham, and E.C. Kerrigan. Robust control synthesis for gust load alleviation from large aeroelastic models with relaxation of spatial discretisation. *Proceedings of the EWEA*, 2012.

[80] T.E. Oliphant. *A Guide to NumPy*, volume 1. Trelgol Publishing USA, 2006.

[81] R. Palacios. Nonlinear normal modes in an intrinsic theory of anisotropic beams. *Journal of Sound and Vibration*, 330(8):1772–1792, 2011.

[82] R. Palacios and C.E.S. Cesnik. Cross-sectional analysis of nonhomogeneous anisotropic active slender structures. *AIAA Journal*, 43(12):2624–2638, 2005.

[83] R. Palacios, J. Murua, and R. Cook. Structural and aerodynamic models in nonlinear flight dynamics of very flexible aircraft. *AIAA Journal*, 48(11): 2648–2659, 2010.

[84] M.J. Patil, D.H. Hodges, and C.E.S. Cesnik. Nonlinear aeroelasticity and flight dynamics of high-altitude long-endurance aircraft. *Journal of Aircraft*, 38(1):88–94, 2001.

[85] S.T. Pinho, L. Iannucci, and P. Robinson. Physically based failure models and criteria for laminated fibre-reinforced composites with emphasis on fibre kinking. part ii: Fe implementation. *Composites Part A: Applied Science and Manufacturing*, 37(5):766–777, 2006.

[86] B. Popescu and D.H. Hodges. Asymptotic treatment of the trapeze effect in finite element cross-sectional analysis of composite beams. *International Journal of Non-Linear Mechanics*, 34(4):709–721, 1999.

[87] P. Qiao and L. Shan. Explicit local buckling analysis and design of fiber–reinforced plastic composite structural shapes. *Composite Structures*, 70(4):468–483, 2005.

[88] S.S. Quek and G.R. Liu. *Finite Element Method: A Practical Course: A Practical Course*. Butterworth-Heinemann, 2003.

[89] O. Rand. On the importance of cross-sectional warping in solid composite beams. *Composite Structures*, 49(4):393 – 397, 2000. doi: http://dx.doi.org/10.1016/S0263-8223(00)00073-8.

[90] D.P. Raymer et al. *Aircraft design: a conceptual approach*, volume 3. American Institute of Aeronautics and Astronautics, 1999.

[91] J.N. Reddy. A simple higher-order theory for laminated composite plates. *Journal of applied mechanics*, 51(4):745–752, 1984.

[92] E. Reissner. On one-dimensional large-displacement finite-strain beam theory. *Studies in applied mathematics*, 52(2):87–95, 1973.

[93] E.J. Sapountzakis and J.A. Dourakopoulos. Flexural-torsional buckling analysis of composite beams by {BEM} including shear deformation effect. *Mechanics Research Communications*, 35(8):497 – 516, 2008. doi: http://dx.doi.org/10.1016/j.mechrescom.2008.06.007.

[94] E.J. Sapountzakis and D.G. Panagos. Shear deformation effect in non-linear analysis of composite beams of variable cross section. *International Journal of Non-Linear Mechanics*, 43(7):660 – 682, 2008. doi: http://dx.doi.org/10.1016/j.ijnonlinmec.2008.03.005.

[95] C.M. Shearer and C.E.S. Cesnik. Nonlinear flight dynamics of very flexible aircraft. *Journal of Aircraft*, 44(5):1528–1545, 2007.

[96] J.R. Shewchuk. Triangle: Engineering a 2D quality mesh generator and Delaunay triangulator. In *Applied computational geometry towards geometric engineering*, pages 203–222. Springer, 1996.

[97] S.J. Shin. *Design, manufacturing, and testing of an active twist rotor*. PhD thesis, Massachusetts Institute of Technology, 1999.

[98] J.C. Simo. A finite strain beam formulation. the three-dimensional dynamic problem. part i. *Computer Methods in Applied Mechanics and Engineering*, 49(1):55–70, 1985.

[99] J.C. Simo and L. Vu-Quoc. On the dynamics of flexible beams under large overall motions—the plane case: Part II. *Journal of Applied Mechanics*, 53: 855, 1986.

[100] J.C. Simo and L. Vu-Quoc. A three-dimensional finite-strain rod model. Part II: Computational aspects. *Computer Methods in Applied Mechanics and Engineering*, 58(1):79–116, 1986.

[101] J.C. Simo and L. Vu-Quoc. On the dynamics in space of rods undergoing large motions: a geometrically exact approach. *Computer Methods in Applied Mechanics and Engineering*, 66(2):125–161, 1988.

[102] R. Simpson and R. Palacios. Numerical aspects of nonlinear flexible aircraft flight dynamics modeling. In *Proceedings of the 54th AIAA Structures, Structural Dynamics and Materials Conferences. Boston, Massachussets, AIAA-2013-1634*, 2013.

[103] DCS Simulia. Abaqus 6.11 analysis user's manual. *Abaqus 6.11 Documentation*, 2011.

[104] B.L. Stevens and F.L. Lewis. *Aircraft control and simulation*, volume 2. Wiley New York, 2003.

[105] W. Su and C. E. S. Cesnik. Strain-based analysis for geometrically nonlinear beams: A modal approach. In *53rd AIAA/ASME/ASCE/AHS/ASC Structures, Structural Dynamics, and Materials Conference*, Honolulu, HI, USA, 2012.

[106] W. Su and C.E.S. Cesnik. Dynamic response of highly flexible flying wings. *AIAA journal*, 49(2):324–339, 2011.

[107] S.P. Timoshenko. On the transverse vibrations of bars of uniform cross-section. *The London, Edinburgh, and Dublin Philosophical Magazine and Journal of Science*, 43(253):125–131, 1922.

[108] D. Tounsi, J.B. Casimir, and M. Haddar. Dynamic stiffness formulation for circular rings. *Computers & Structures*, 112–113(0):258 – 265, 2012. doi: http://dx.doi.org/10.1016/j.compstruc.2012.08.005.

[109] V.V. Volovoi, D.H. Hodges, C.E.S. Cesnik, and B. Popescu. Assessment of beam modeling methods for rotor blade applications. *Mathematical and computer modelling*, 33(10):1099–1112, 2001.

[110] E.L. Wilson. The static condensation algorithm. *International Journal for Numerical Methods in Engineering*, 8(1):198–203, 1974.

[111] E.L. Wilson. *Three-dimensional static and dynamic analysis of structures*. CSi Computers and Structures, Berkeley, 2002.